The Devonian-Carboniferous Boundary In Vietnam: Sustained Ocean Anoxia With A Volcanic Trigger For The Hangenberg Crisis?

By: Olivia Paschall, **Sarah K. Carmichael**, Peter Königshof, Johnny A. Waters, Phuong H. Ta, Toshifumi Komatsu, & Allison Dombrowski

Abstract

The Devonian-Carboniferous transition (359 Ma) was a time of extreme climate and faunal change and is associated with the end-Devonian biodiversity crisis. The transition is characterized by transgressive/regressive cycles, which culminated in the onset of widespread ocean anoxia (the Hangenberg Black Shale event) and a remarkable sea-level fall close to the Devonian-Carboniferous boundary (the Hangenberg Sandstone event); together these are known as the Hangenberg Crisis. The Hangenberg Crisis has been documented around the globe, but the trigger mechanisms for its onset remain unknown. The Pho Han Formation on Cat Ba Island in northeastern Vietnam preserves the Devonian-Carboniferous transition and Hangenberg Crisis in a sediment-starved basinal facies on the South China carbonate platform. Although the Hangenberg Black Shale event is generally preserved as a discrete anoxic interval in Devonian-Carboniferous boundary sections of North America and Europe, the Pho Han Formation records sustained dysoxic/anoxic conditions from the Famennian (Upper Devonian) through the Tournasian (early Carboniferous), with severe anoxia (approaching euxinia) throughout the Hangenberg Black Shale event interval (as determined by trace element proxies, increased total organic carbon, and framboidal pyrite distributions). There is also significant mercury enrichment corresponding to the Hangenberg Crisis in the Pho Han Formation. The isolated paleogeography of the region suggests that the mercury is most likely sourced from distal volcanic emissions. It is therefore possible that large-scale volcanic activity acted as a trigger mechanism for the Hangenberg Crisis and biodiversity drop at the Devonian- Carboniferous transition, similar to other major mass extinction events.

Paschall, O.C., **Carmichael, S.K.**, Königshof, P., Waters, J.A., Ta Hoa, P., Komatsu, T., Dombrowski, A.D., 2019. The Hangenberg Event in Vietnam: sustained ocean anoxia with a volcanic trigger? Global and Planetary Change (Special issue on Devonian global changes - recent advances and challenges in different domains, eds. G. Racki and P. Wignall), v. 175, p. 64-81. DOI: 10.1016/j.gloplacha.2019.01.021. Publisher version of record available at: https://www.sciencedirect.com/science/article/pii/S0921818118304405?via%3Dihub

Paschall, O.C., Carmichael, S.K., Königshof, P., Waters, J.A., Ta Hoa, P., Komatsu, T., Dombrowski, A.D., 2019. The Hangenberg Event in Vietnam: sustained ocean anoxia with a volcanic trigger? Global and Planetary Change (Special issue on *Devonian global changes - recent advances and challenges in different domains*, eds. G. Racki and P. Wignall), v. 175, p. 64-81. DOI: 10.1016/j.gloplacha.2019.01.021

The copy of record is available from Elsevier
https://www.sciencedirect.com/science/article/pii/S0921818118304405?via%3Dihub.

The Devonian-Carboniferous boundary in Vietnam: sustained ocean anoxia with a volcanic trigger for the Hangenberg Crisis?

Olivia Paschall[1], Sarah K. Carmichael[1,*], Peter Königshof[2], Johnny A. Waters[1], Phuong H. Ta[3], Toshifumi Komatsu[4], Allison Dombrowski[1]

1. Department of Geological and Environmental Sciences, ASU Box 32067 Appalachian State University, Boone, NC 28608, USA
2. Senckenberg Research Institute and Natural History Museum, Senckenberganlage 25, 60325 Frankfurt, Germany
3. Hanoi National University, 334 Nguyen Trai Str. Than Xuan Dist. Hanoi, Vietnam
4. Graduate School of Science and Technology, Kumamoto University, Kumamoto 806-8555, Japan

* Corresponding author at: ASU Box 32067, Appalachian State University, Boone, NC 28608, USA.
Tel.: +1 828 262 8471. E-mail address: carmichaelsk@appstate.edu (S.K. Carmichael).

Graphical Abstract:

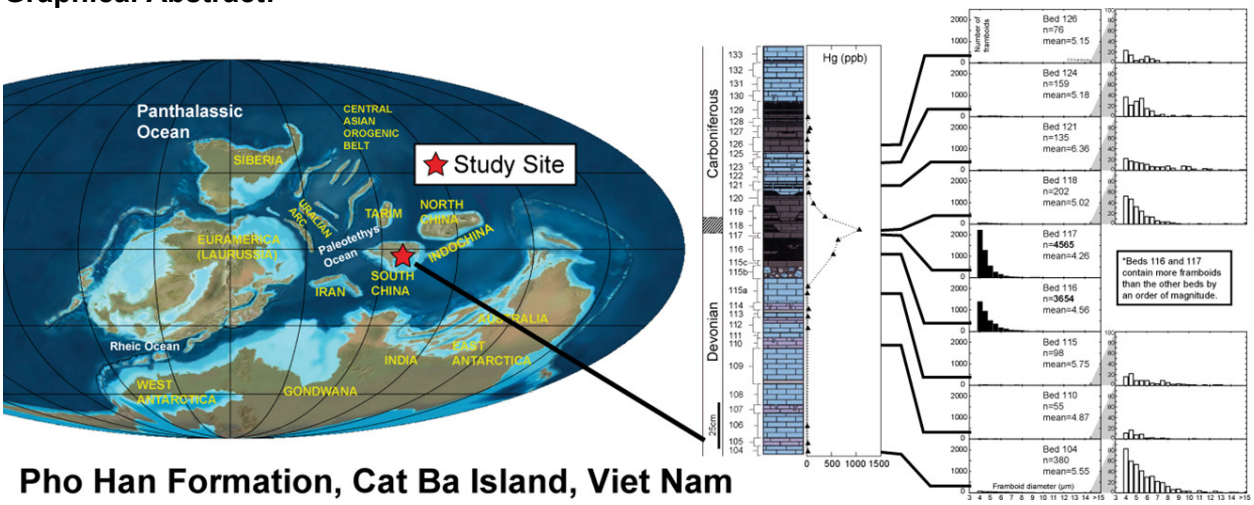

Highlights

- The Late Devonian Pho Han Formation represents a sediment-starved carbonate basin on the South China platform.
- The Cat Co 3 section experienced long-term anoxia/dysoxia in the Famennian, with euxinia during the Hangenberg Crisis.
- Hg chemostratigraphy indicates a possible volcanic trigger for the end-Devonian mass extinction event.

Article history:
Received 15 August 2018,
Revised 22 January 2019,
Accepted 31 January 2019,
Available online 4 February 2019.
Handling Editor: G. Racki

Keywords:
Hangenberg event; Ocean anoxia; Vietnam; Devonian-Carboniferous; Volcanic trigger

Abstract
The Devonian-Carboniferous transition (359 Ma) was a time of extreme climate and faunal change and is associated with the end-Devonian biodiversity crisis. The transition is characterized by transgressive/regressive cycles, which culminated in the onset of widespread ocean anoxia (the Hangenberg Black Shale event) and a remarkable sea-level fall close to the Devonian-Carboniferous boundary (the Hangenberg Sandstone event); together these are known as the Hangenberg Crisis. The Hangenberg Crisis has been documented around the globe, but the trigger mechanisms for its onset remain unknown. The Pho Han Formation on Cat Ba Island in northeastern Vietnam preserves the Devonian-Carboniferous transition and Hangenberg Crisis in a sediment-starved basinal facies on the South China carbonate platform. Although the Hangenberg Black Shale event is generally preserved as a discrete anoxic interval in Devonian-Carboniferous boundary sections of North America and Europe, the Pho Han Formation records sustained dysoxic/anoxic conditions from the Famennian (Upper Devonian) through the Tournasian (early Carboniferous), with severe anoxia (approaching euxinia) throughout the Hangenberg Black Shale event interval (as determined by trace element proxies, increased total organic carbon, and framboidal pyrite distributions). There is also significant mercury enrichment corresponding to the Hangenberg Crisis in the Pho Han Formation. The isolated paleogeography of the region suggests that the mercury is most likely sourced from distal volcanic emissions. It is therefore possible that large-scale volcanic activity acted as a trigger mechanism for the Hangenberg Crisis and biodiversity drop at the Devonian-Carboniferous transition, similar to other major mass extinction events.

1. Introduction

The Devonian-Carboniferous (D-C) transition and mass extinction is characterized as a period of severe ecological crisis, with major biotic and palaeoenvironmental changes in both terrestrial and marine ecosystems. The extinction eliminated about 20% of marine invertebrate genera, and primarily decimated pelagic organisms such as fish and cephalopods, reducing long-term biodiversity of all vertebrates by 50% (Sandberg et al., 2002; Sepkoski, 1996; Walliser, 1996). The ecological severity index by McGhee et al. (2013) characterizes the end Devonian extinction as the fourth most severe mass extinction event in Earth's history.

Historically, the D-C boundary has been defined via conodont biostratigraphy from the Global Stratotype Section and Point (GSSP) location La Serre Trench E' section in the Montagne Noire, France, where it is based on the first appearance of the basal Carboniferous conodont *Siphonodella sulcata* (Flajs and Feist, 1988; Paproth et al., 1991). However, these early siphonodellids are difficult to identify due to taxonomic uncertainties (Kaiser and Corradini, 2011), and *Siphonodella sulcata* is also found below the level that defines the La Serre GSSP (Kaiser, 2009). Furthermore, there is concern that the La Serre sediments have been reworked and are not correlatable to other sections (Sandberg and Ziegler, 1996; Ziegler and Sandberg, 1994). Therefore, the D-C boundary needs to be reevaluated, either via new biostratigraphic indicators (Aretz, 2013; Corradini et al., 2017) or via a combined biostratigraphic and sedimentological set of criteria (e.g. Becker et al., 2016; Walliser, 1984). As there are ongoing discussions for how to best define the D-C boundary using conodont biostratigraphy that have not yet been concluded at the time of this writing, the section studied in this paper will use a biostratigraphic correlation scheme based on the zonations from Kaiser (2009), Ziegler and Sandberg (1990), and Spalletta et al. (2017) (Fig. 1).

The D-C transition is not only associated with a mass extinction, but also a time of marine regression and widespread oceanic anoxia, called the Hangenberg Crisis. The Hangenberg Crisis has been recognized in sediments from epicontinental basins and continental margins around the world (see reviews by Becker et al., 2016; Kaiser et al., 2016). It can be subdivided into the Hangenberg Black Shale (HBS) event, which is marked by widespread deposition of black shale, and the regressive Hangenberg Sandstone (HSS) event, which at times is only visible in the rock record as an unconformity (Bábek et al., 2016; Cole et al., 2015; Kaiser et al., 2016). The global regression associated with the HSS Event appears to be related to continental icesheet growth in South America (Caputo et al., 2008; Isaacson et al., 1999; Lakin et al., 2016; Streel et al., 2000), North Africa (summarized in Isaacson et al., 2008) and mountain glaciers in the Appalachians of North America (Brezinski et al., 2010; Brezinski et al., 2009). Aside from a general agreement regarding a glacially influenced regression to explain the HSS Event, the mechanisms that triggered the anoxia of the HBS Event and related extinction at the D-C boundary are still debated (Caplan and Bustin, 1999; Caplan and Bustin, 2001; Caplan et al., 1996; Carmichael et al., 2016; Formolo et al.,

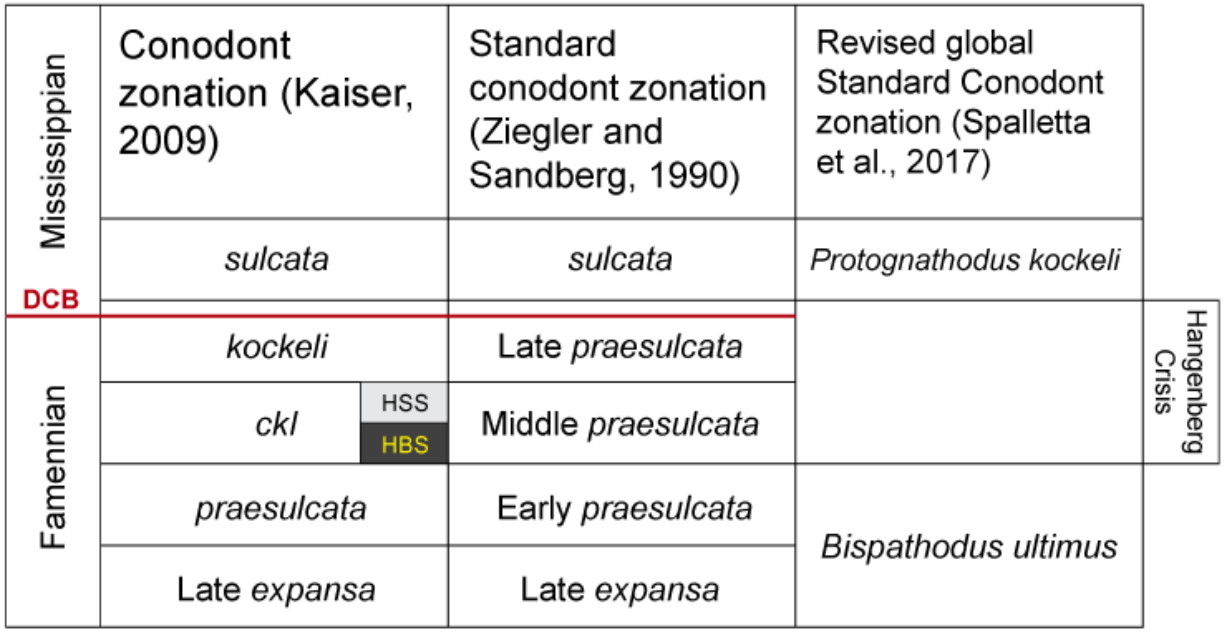

Figure 1. Overview of conodont zonation of the uppermost Devonian used to constrain the D-C boundary. HSS = Hangenberg Sandstone, HBS = Hangenberg Black Shale, *ckl* = *costatus kockelianus* interregnum according to Kaiser (2009). Figure modified from Ziegler and Sandberg (1990), Kaiser (2009), and Spalletta et al. (2017).

2014; Kumpan et al., 2019; Martinez et al., 2018; Marynowski and Filipiak, 2007; Marynowski et al., 2012; Matyja et al., 2015; Menor-Salván et al., 2010; Myrow et al., 2014; Prestianni et al., 2016).

In fact, the processes and mechanisms of all of the Devonian ocean anoxia events (such as the Dasberg, Kellwasser, and Eifelian Events, as well as the HBS Event) still remain contentious, as they likely represent a combination of long-term and short-term factors (see analyses by Carmichael et al., in review (this volume); Kaiser et al., 2016; McGhee, 2001; McGhee, 2005; Racki, 2005). Components of Late Devonian climate instability and changes in sediment/nutrient supply to the oceans include a dramatic decrease in atmospheric CO_2 via the evolution of complex land plant ecosystems, which would also increase the amount of nutrients supplied to the oceans (Algeo et al., 1995; Algeo and Scheckler, 1998). At the same time, there were active tectonic processes in the tropics that affected both climate and oceanographic processes (Averbuch et al., 2005; Copper, 1986). Trigger mechanisms for pulses of Devonian anoxia may include meteorite impacts (although this has long been refuted; see Racki (2012) for a comprehensive review), orbital forcing (De Vleeschouwer et al., 2014; De Vleeschouwer et al., 2017; De Vleeschouwer et al., 2018), the presence of large igneous provinces (LIPs) (Bond and Wignall, 2014; Kravchinsky, 2012), or prolonged volcanic activity from a variety of non-point sources (Racki et al., 2018b), at least for the Frasnian-Famennian extinction. One of the challenges of associating LIPs or massive volcanism with the D-C boundary is a lack of obvious LIPs preserved in the rock record, although there is a potential associated LIP from eastern Canada (Dessureau et al., 2000; Murphy et al., 1999). Furthermore, widespread volcanic activity near the stratigraphically-constrained D-C boundary in both Uzbekistan and Germany has been suggested through perturbations in the Hg cycle (Racki et al., 2018a), and submarine volcanism has been associated with the D-C boundary for sites in South China (Bai, 2001; Lai et al., 2014; Liu et al., 2012), while catastrophic volcanism has been suggested as a driver of ecological collapse at the D-C boundary in the Iberian pyrite belt in Spain (Moreno et al., 1996).

It is important to recognize that most of the information about the Late Devonian anoxia events is compiled from sites along tropical continental margins or within epicontinental basins in Europe and North America (Carmichael and Waters, 2015) many of which were receiving increased sediment supply due to active tectonism (Averbuch et al., 2005; Carmichael et al., in review (this volume); Carmichael and Waters, 2015; Carmichael et al., 2016). As a step towards addressing this problem of paleogeographic sample bias, here we discuss the Hangenberg Crisis in a new location in Vietnam, in a sediment-starved carbonate basin that is associated with the South China continental block and is far from any arc-derived sedimentary material. The multiproxy data gathered from this unusually isolated paleoenvironment also allows for the consideration of possible trigger mechanisms for the anoxia and extinction at the D-C boundary.

2. Regional Geology and Biostratigraphy

The Devonian to Carboniferous Pho Han Formation is exposed at the Cat Co 3 beach section on Cat Ba Island, Hai Phong Province, northeastern Vietnam (Fig. 2).

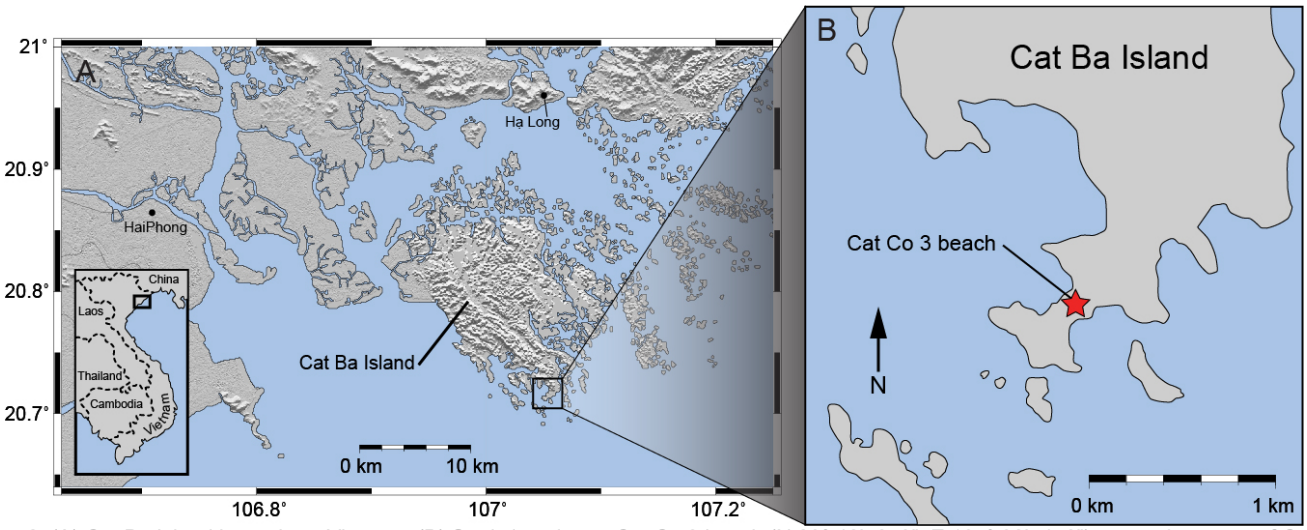

Figure 2. (A) Cat Ba Island in northern Vietnam. (B) Study location at Cat Co 3 beach (N 20° 42'58, 0", E 107° 02'54, 8") on southern part of Cat Ba Island. Figure modified from Komatsu et al. (2014).

Tectonic reconstructions (Fig. 3) and provenance analysis place this region within the South China block during the Late Devonian (Zhang et al., 2014), making the Cat Co 3 section one of the few sections on the eastern South China continental block of the Paleotethys Sea that preserves continuous deposition across the D-C boundary (Komatsu et al., 2014). According to the Standard Conodont Zonation (Ziegler and Sandberg, 1990), the section spans the *Palmatolepis expansa* conodont zone to the *Siphonodella duplicata* conodont zone (Komatsu et al., 2014; Ta Hoa and Doan, 2005; Ta Hoa and Doan, 2007) (Fig. 4). Using the Ziegler and Sandberg (1990) criteria, the D-C boundary definition is based on the first appearance of the conodont *Siphonodella sulcata* following the *Siphonodella praesulcata* subzone (Paproth et al., 1991; Sandberg et al., 1978; Ziegler and Sandberg, 1990). Bed 115c can be correlated with the Upper *Siphonodella praesulcata* subzone and *Siphonodella sulcata* appears for the first time in bed 119. More recent work by Corradini et al. (2017) suggests that the D-C boundary is instead between *Bispathodus ultimus* and *Protognathus kockeli* (Fig. 1), with the base of the Carboniferous defined at the first appearance of either *Protognathus kockeli* or *Siphonodella bransoni*. In the Cat Co 3 section, unfortunately, these conodonts were not found. The revised and less detailed stratigraphy of the uppermost Famennian (Fig. 1) by Corradini et al. (2017) is applicable to the Cat Co 3 section, even though conodonts are rare in beds 116-119. The *ultimus* Zone starts in bed 106 with the occurrence of *Pseudopolygnathus marburgensis trigonicus*, which disappears in the upper part of the *ultimus* Zone. *Siphonodella praesulcata* (found for the first time in bed 113) correlates in the middle part of this zone (Spalletta et al., 2017). Others, such as *Palmatolepis gracilis expansa* (found in bed 115c) disappear in the upper part of the *ultimus* Zone. According to the biostratigraphic record and the lithology such as the laminated black shale in bed 116, we conclude that this bed (116) is an equivalent to the HBS. The following two beds (117 and 118) contain fragments of *Pseudochaetetes elliotti* and *Parachaetetes* sp.as well as brachiopod shell hash; these shallow water faunas may represent an equivalent to the Hangenberg Sandstone (HSS) close to the D-C boundary. We place the D-C boundary at the top of bed 118, and use *Siphonodella sulcata* to define the beginning of the Carboniferous, which occurs for the first time in bed 119.

At the Cat Co 3 beach section, the Pho Han Formation is approximately 500 m thick and consists of ramp platform carbonates and slope deposits (Doan and Tong-Dzuy, 2006; Komatsu et al., 2014; Komatsu et al., 2012a; Ta Hoa and Doan, 2005; Ta Hoa and Doan, 2007). At the D-C boundary, the section is very condensed and the depositional environment is interpreted as a deep ramp to marginal basin plain, and primarily consists of micritic whitish gray to gray limestones, marls, and interbedded thin dark gray limestones and organic-carbon-rich, black, friable limestones (Komatsu et al., 2014) (Fig. 4). The zone around beds 115-118 shows alternating thin, dark gray limestone and black friable limestone with no evidence of bioturbation, whereas the light limestones in the rest of the section are occasionally bioturbated (Komatsu et al., 2014). The organic-rich black limestones of beds 116-118 most likely represent the equivalent of the HBS and HSS, and bed 118 represents the D-C boundary (Fig. 4). The overlying sediments are characterized by the increased number of calcareous algae and small brachiopod shell hash (mainly organic-rich bioclastic and intraclastic packstone). The overall fossil content of the carbonates is mainly composed of conodont elements, foraminifers, brachiopods, and crinoid stems in ascending order (Komatsu et al., 2014). The entire section mainly represents deep-ramp carbonate sediments which were likely deposited under long-term dysoxic/anoxic conditions.

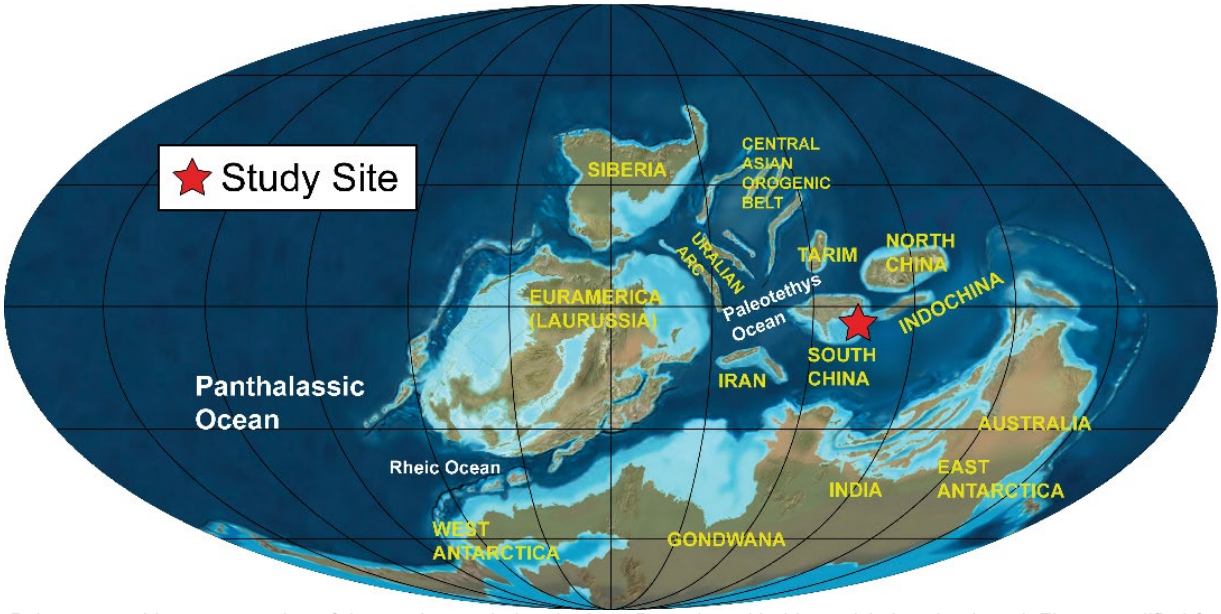

Figure 3. Paleogeographic reconstruction of the continents during the Late Devonian with this study's location in red. Figure modified from Blakey (2016), using updated paleogeographic data for Asia from Xiao et al. (2010) and Metcalfe (2009).

3. Materials and Methods

Whole rock geochemical analyses (major, trace, and rare earth element (REE) geochemistry) were performed by Activation Laboratories in Ancaster, Ontario, Canada, using the Total IDENT 4E-Research package, with Code 1G-Hg CV Hg-Cold Vapour FIMS for Hg analyses. Total organic carbon (TOC) data were taken from Komatsu et al. (2014).

Samples were analyzed for mineralogy and framboidal pyrite distributions using a JEOL JSM-IT300LV scanning electron microscope (SEM) with an Oxford AZtecEnergy integrated silicon drift energy dispersive X-ray spectroscopy (EDS) system at the Dewel Microscopy Facility at Appalachian State University in Boone, NC (USA). Automated feature detection, measurement, and analyses were performed with Oxford Aztec Feature Analysis to scan, count, and measure the diameters of pyrite framboids over a 1 cm^2 grid area, with 520 frames spaced evenly across the grid (resulting in a total analyzed area of 26.21 mm^2). Statistical analysis of 0% grid spacing (100 mm^2 total analyzed area, using 2028 images) vs. 100% grid spacing (26.21 mm^2 total analyzed area, using 520 images) shows that 100% spacing produces a framboid count and size distribution that is consistent with 0% spacing (see supplemental information for additional methodology details).

X-ray diffraction (XRD) was performed on a Shimadzu 6000 X-ray diffractometer at Appalachian State University, using a Cu tube X-ray source at 40 kV and 30 mA, and scanning from 5–80° or 10–80° 2Θ. Minerals were identified using the PDF/4+ database and/or Match! Phase Identification from Powder Diffraction software.

Carbon-isotope analyses for both calcite and organic carbon ($\delta^{13}C_{carb}$ and $\delta^{13}C_{org}$) were performed in the GeoZentrum Nordbayern at the Friedrich-Alexander Universität Erlangen-Nürnberg, Erlangen, Germany. Calcite samples were powdered and mixed with 100% phosphoric acid at 70°C, and analyzed via a Gasbench II system with a ThermoFinnigan Delta Five Plus mass spectrometer. $\delta^{13}C_{org}$ analysis was performed using a Carlo-Erba1110 elemental analyzer coupled with to a ThermoFinnigan Delta Plus mass spectrometer. All values are reported in ‰VPDB. The same methods were used across both $\delta^{13}C_{carb}$ sample sets.

Strontium isotope ($^{87}Sr/^{86}Sr$) analyses were performed at the University of North Carolina at Chapel Hill following the methodology of Carmichael et al. (2016). Between 3.5-5.9 mg of powdered rock sample was dissolved in 600 µL 3.5M HNO_3 for a minimum of 24 hours at room temperature. The subsequent solution was centrifuged, the supernatant was extracted, and was run through 50-100 µm Eichrome Sr-B100-S Sr Resin columns. 25-30 µL of 2M H_3PO_4 was added to the solution, then dried at 120°C. The resulting sample bead was rehydrated in 2 µL $TaCl_5$ and 2 µL 2M HCl and loaded onto Re filaments and analyzed with a VG Sector 54 thermal ionization mass spectrometer (TIMS). See Carmichael et al. (2016) for correction/normalization factors and instrument operating conditions.

Principal component analysis (PCA) was performed using program PAST 3.2 (Hammer et al., 2001) after geochemical data were converted to elemental weight percent and adjusted using the arcsine transform in Microsoft Excel. PCA was performed on whole-rock geochemical data, and repeated using trace elements only.

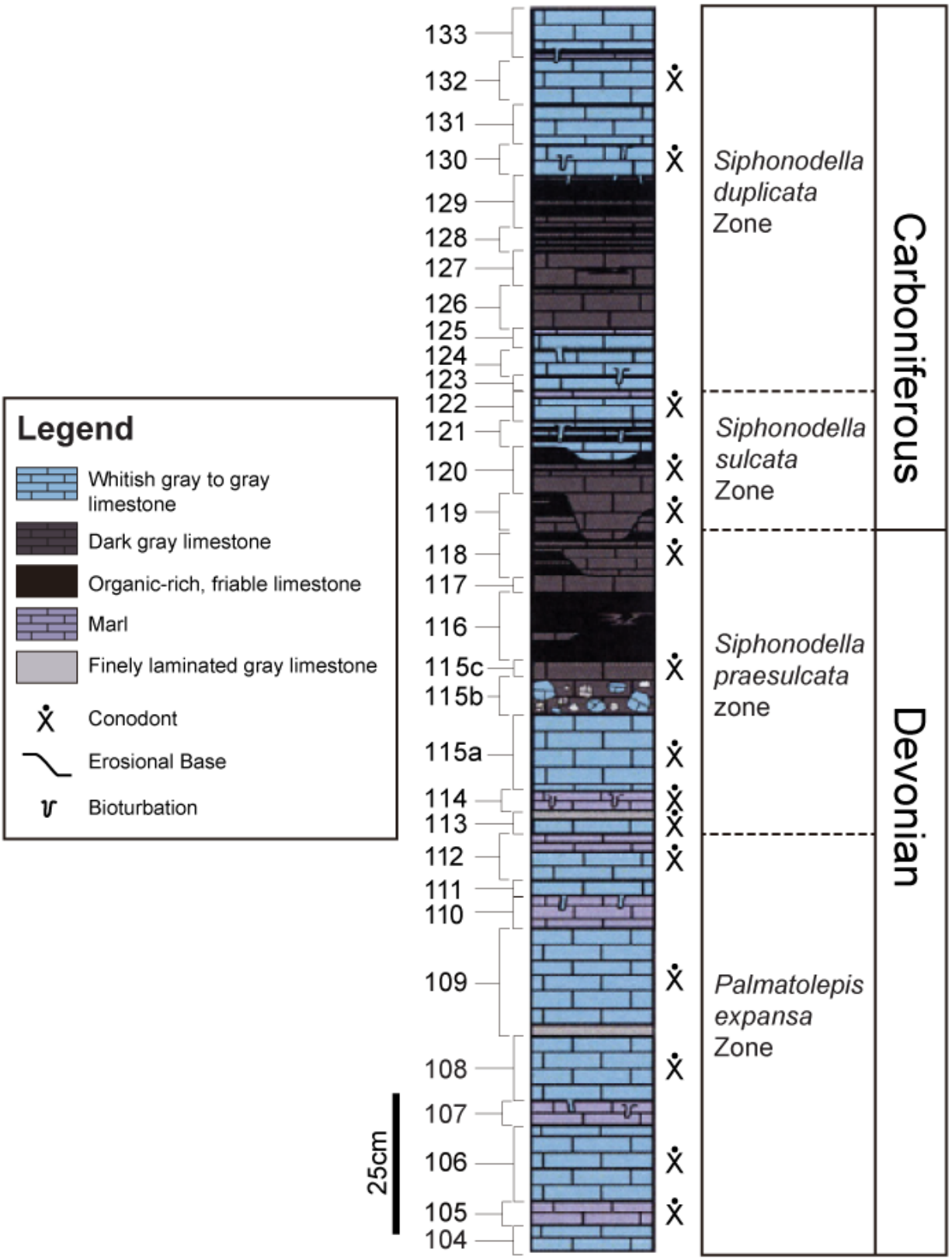

Figure 4. Lithological log of the Cat Ba Island section (Pho Han Formation) and conodont stratigraphy of the important conodont taxa modified from Komatsu et al. (2014) and Ta Hoa and Doan (2005). Based on the lack of index species, the revised conodont stratigraphy suggested by Spalletta et al. (2017) was not used; the Conodont Standard Zonation Ziegler and Sandberg (1990) was used instead (comparisons provided in Figure 1). The D-C boundary is placed at the top of bed 118.

4. Results and Discussion

4.1. Major and Trace Element Geochemistry

4.1.1. Lithology and resulting caveats on proxy data

Caution must be exercised when considering many redox and productivity proxies, as they can be inconsistent and strongly controlled by lithology and/or depositional environment (Brumsack, 2006; Carmichael et al., 2016; Piper and Calvert, 2009; Tribovillard et al., 2006; Ver Straeten et al., 2011). The Cat Co 3 section has generally consistent lithology (limestones, organic-rich limestones) with the exception of a minor increase in clay particles and an increase in total organic carbon (TOC) at the stratigraphic position of the Hangenberg Crisis. SEM-EDS imaging and analysis indicates there is little measurable non-carbonate input, aside from widely dispersed fine quartz silt and illite clay particles. The beds near the stratigraphic position of the D-C boundary (beds 116, 117, 120, and 121) do contain slightly more Al_2O_3 than the other samples (Fig. 5), but SEM-EDS analysis of these beds does not show a change in mean grain size or mineralogy in these samples, only changes in the relative abundance of calcite compared to quartz silt and illite clay. Supporting these SEM-EDS observations, there is no associated increase in the detrital proxies of Ti/Al, Si/Al, or Zr/Rb in these beds (Fig. 5) (see section 4.5 for discussion on Zr outlier data point at bed 115). Microfacies analysis also shows no major changes in depositional environment across the section (Komatsu et al., 2014). The lack of significant sand-size detrital input from coastal margins (either active or passive) precludes provenance analysis as described by Bhatia and Crook (1986), and microfacies analysis is consistent with a carbonate basin setting that is far offshore.

Although the constant lithology across the section *should* make interpretations of proxy data straightforward, the Cat Co 3 section has an extremely low detrital fraction (beds 116 and 117 at the expected location of the HBS Event are the most Al-rich samples in the section with an Al_2O_3 content of 2.9 wt % compared to the average background value of 0.32 wt % for the Famennian part of the section). The section's extremely low Al content makes trace element normalization to Al quite problematic for interpreting redox and productivity proxies (Tribovillard et al., 2006), as minor changes in Al content will amplify natural scatter in trace element data rather than reflect actual excursions. Average Al/Ti ratios in the Cat Co 3 section are 38.7, far higher than the average Al/Ti ratio of 17 found in the reference Post Archean Australian Shale (PAAS), and therefore indicate Al scavenging by organic matter in the water column and/or diagenetic clay formation

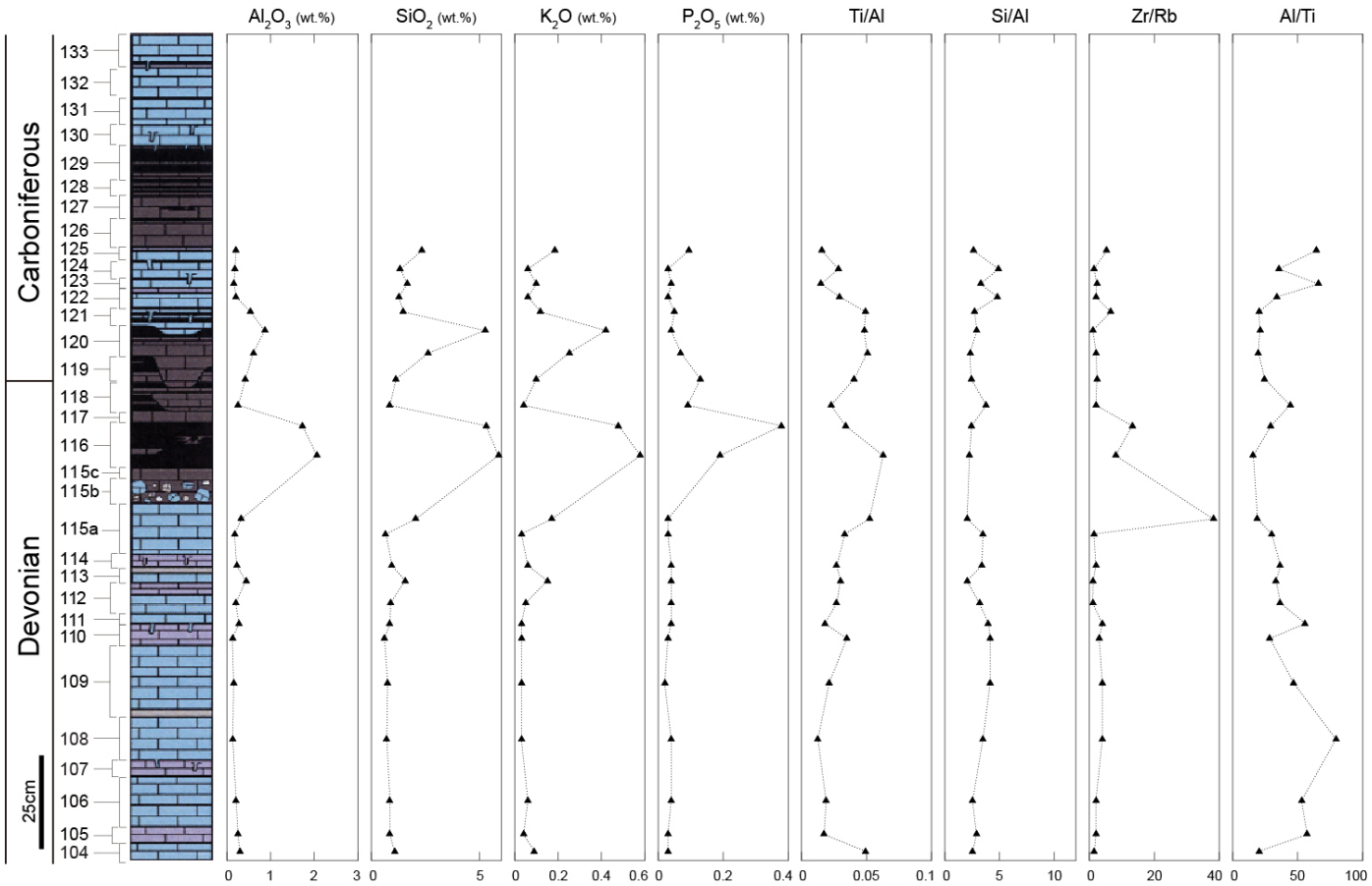

Figure 5. Chemostratigraphy plots of lithologic proxies (Al_2O_3, SiO_2, K_2O, Ti/Al, Si/Al, Zr/Rb, and Al/Ti).

rather than a detrital contribution (Murray and Leinen, 1996). Furthermore, using the methodology of Van der Weijden (2002) that compares the coefficient of variation (the standard deviation divided by the mean) for Al against that of individual trace elements, nearly all the standard anoxia and productivity trace element proxies used in this study become distorted and potentially useless when normalized to Al (as shown by coefficients of variation for the Cat Co 3 section in Supplemental Table S1; the full geochemical dataset is provided in Supplemental Table S2). In cases where the coefficients of variation for trace elements are smaller than the coefficients of variation for Al, normalizing to enrichment factors (EFs) in shales such as the PAAS is likewise problematic, according to Van der Weijden (2002). Taken together with the Al/Ti ratios, which indicate biological and/or diagenetic processes of Al deposition rather than detrital processes where normalization to shales would be useful, all geochemical proxy data used for the Cat Co 3 section have not been normalized. To maintain consistency across datasets for other D-C boundary sections, figures with Al- and PAAS-normalized proxy data are provided in the supplemental data (Figs. S1-S3), but we urge *extreme* caution in interpreting any trace element enrichment patterns from these supplemental figures. Supplemental Fig. S1 provides detailed information about the relationship between common redox and productivity proxies and Al content in the Cat Co 3 section; these plots likewise indicate that the elemental signatures for the majority of the section (where Al_2O_3 < 1, representing baseline conditions, i.e. no ecological crisis) are independent of lithology.

4.1.2. Increased clastic input versus shutdown of the carbonate factory

There is both increased TOC (Fig. 6) and corresponding increases in SiO_2, Al_2O_3, and K_2O (Fig. 5) within beds 116 and 117 (bed 116 is the expected location of the HBS Event in the Cat Co 3 section, based on both biostratigraphy as well as lithology and redox proxies, discussed in *4.1.3*). SEM-EDS and XRD analysis indicates that the increase in SiO_2, Al_2O_3, and K_2O corresponds to minor increases in the proportion of illite clay and quartz silt, although whether the source of the quartz and illite is biogenic, detrital, or diagenetic is unclear at this time. There are neither detrital nor authigenic K-feldspar grains in any of the samples, nor detrital albite. Fig. 5 also shows that beds 116 and 117 contain the highest amounts of P_2O_5, but SEM-EDS observations of the section do not indicate an increase in detrital apatite or monazite in beds 116-117. Increased P_2O_5 is only correlated with increases in SiO_2 and Al_2O_3 at the expected location of the HBS Event, but not with the other smaller increases throughout the section.

The middle part of the Hangenberg Crisis (HSS and equivalents) is characterized by a major eustatic sea-level fall of more than 100m (see Kaiser et al., 2016). The D-C boundary regression is most probably glacio-eustatic in origin due to the occurrence of diamictites and dropstones throughout Gondwana and global miospore correlations (Almond et al., 2002; Caputo et al., 2008; Melo et al., 1999; Streel et al., 2001; Streel et al., 2000). Based on palynological analysis, cold-humid conditions are reported from South America during the *R. lepidophyta - V. nitidus* Zone and cold-arid conditions are known from the Old Red Continent (Marshall et al., 2002; Streel et al., 2001). Therefore, the D-C boundary is often associated with major changes in sedimentation (reviewed in Becker et al., 2016), but in some paleoenvironments it can be difficult to determine if the dominant reason for changes in lithology across the Hangenberg Crisis was a regression or a shutdown in the carbonate factory.

Changes in the carbonate factory are frequently preserved in the rock record and have been studied for nearly 200 years, but the reasons for changes in carbonate production are still debated (see reviews by Pomar and Hallock, 2008; Schlager, 2003). Carbonate factory collapse rather than increased clastic sedimentation has been indicated at the HBS Event in mixed clastic/carbonate systems in the Rhenish Massif (Kumpan et al., 2015 and references therein), but in the Moravian Karst and Carnic Alps the relationship between carbonate factory sedimentation and terrigenous clastic input is less clear (Kumpan et al., 2014a), and in the Namur-Dinant basin the increase in clastic material is assigned to detrital input alone (Kumpan et al., 2014b; Kumpan et al., 2019).

The presence of shallow-water organisms in bed 117 (Komatsu et al., 2014) may be correlated with the dramatic sea-level fall associated with the HSS Event, but there are no sedimentological indicators of regression in the section, which is likely due to its distal, deep water paleoenvironmental setting. Although it is tempting to assign the increases in SiO_2, Al_2O_3, and K_2O in beds 116-117 to increased terrigenous clastic input during the regression associated with the Hangenberg Crisis, the microtextures and mineralogy of the sediments in these beds do not necessarily support a terrigenous sediment source. Thus, perturbations to the carbonate factory and preservation of biogenic phosphate appear to be the most reasonable explanation for the increased P_2O_5, SiO_2, K_2O and Al_2O_3 content of beds 116-117 instead of increased detrital input.

4.1.3. Anoxia/Redox proxies

TOC enrichment is a primary indicator of marine anoxia (Calvert and Pedersen, 1992; Tribovillard et al., 2006), and the section displays TOC enrichment between beds 115c and 120 (Komatsu et al., 2014), with a maximum of 5.8 wt.% in bed 116 versus an average background value of <0.5 wt.% (Fig. 6). Enrichments in total sulphur (S) are also used as a primary anoxia indicator (Lyons et al., 2003; Tribovillard et al., 2006) (Fig. 6). Beds 116 and 117 show up to 2 wt. % total S enrichment; SEM-EDS analysis indicates that S enrichment in these beds is controlled by the abundance of framboidal pyrite, as there are no other sulfur-bearing minerals in the section. Total iron (Fe) (Fig. 6) is strongly correlated with total S due to increased framboidal pyrite, described in 4.3, but can also be correlated with SiO_2, Al_2O_3, and K_2O due to increased illite.

Uranium (U) is a redox proxy that is rarely affected by detrital provenance (Tribovillard et al., 2006). Authigenic uranium (U_{auth}) is distinguished from detrital U and calculated with the following formula: $U_{auth} = U_{total} - Th/3$, where Th/3 approximates detrital U (Wignall and Myers, 1988). Bed 117 contains the largest amount of U_{auth} (24.5 ppm), and surrounding beds 116-119 also display elevated levels (>5 ppm), compared to baseline levels that are close to 0 ppm (Fig. 6). U can also be used as a redox proxy in the form of U/Th, where U/Th ratios <0.75 indicate oxic conditions, ratios 0.75-1.25 indicate dysoxic conditions, and ratios >1.25 indicate anoxia (Jones and Manning, 1994). Only one Cat Co 3 bed has U/Th values less than 1.25 (bed 105), indicating that nearly the entire section documents anoxic conditions for most of the recorded history. The section shows a maximum of 39.86 in bed 118, at the expected location of the HBS Event. In the presence of excessive TOC (such as seen in beds 116-117), it is possible that U can remobilize and migrate vertically upwards in the sediment column to reprecipitate where conditions are more favorable (McManus et al., 2005; Tribovillard et al., 2006); this may explain why the highest U/Th enrichment is stratigraphically just above the HBS region, which contains the highest TOC content (Fig. 6).

Molybdenum (Mo) accumulates in restricted basins under long-term anoxic conditions, with concentrations

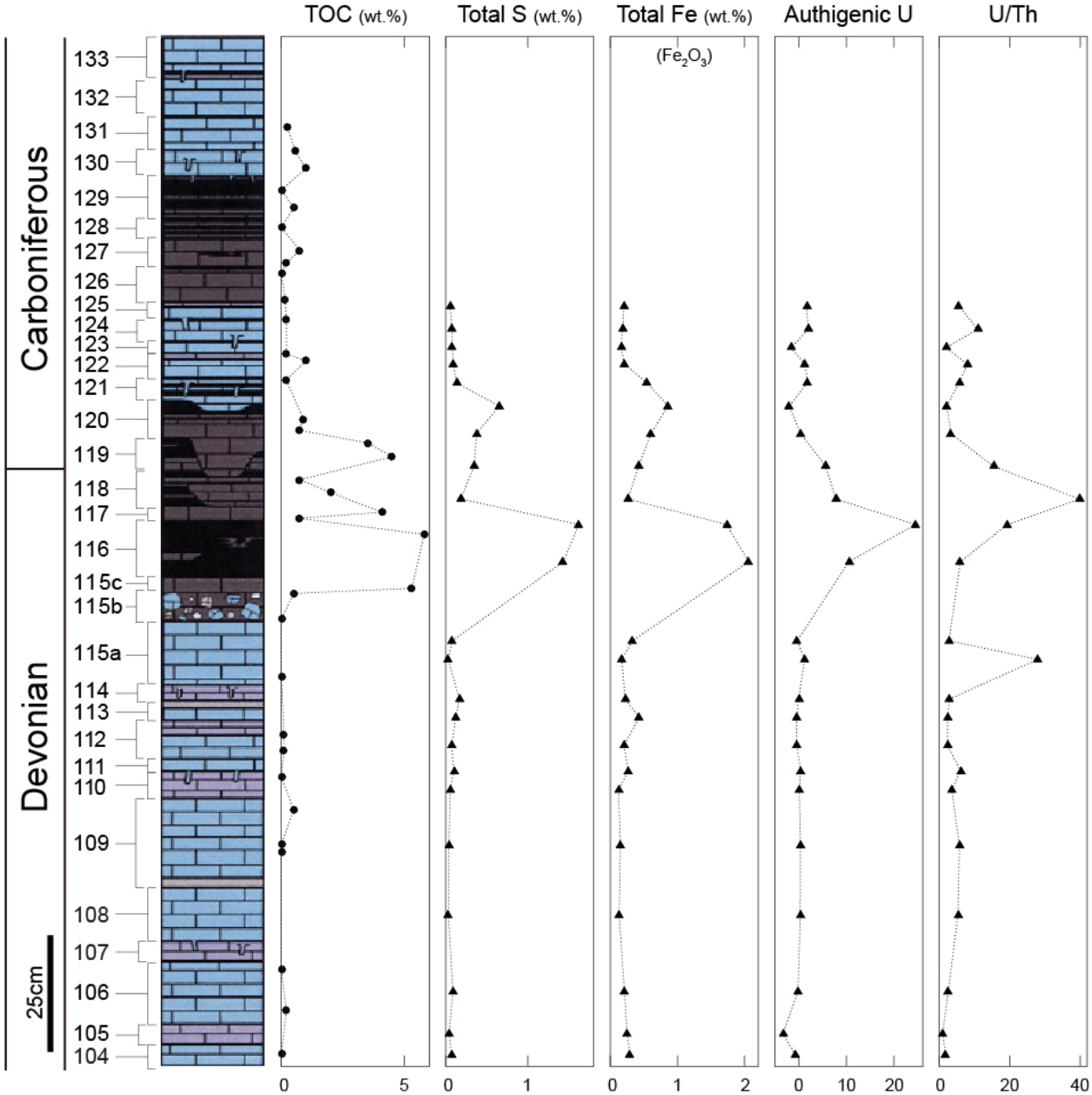

Figure 6. Chemostratigraphy plots of TOC, S, Fe, authigenic U, and U/Th. TOC data from Komatsu et al. (2014). Beds 115-120 generally show enrichments in TOC, authigenic U and U/Th, while beds 116-117 show increased S and Fe (due to pyrite framboids), Enrichment factors and normalization to Al were not used due to low Al concentrations (see 4.1.1 in text for justification).

reaching 50-200 ppm (Algeo and Lyons, 2006; Algeo et al., 2007; Algeo and Maynard, 2008), and is rarely affected by detrital input (Tribovillard et al., 2006). Beds 116 and 117 show a dramatic enrichment in Mo, with values 123 ppm and 44 ppm, respectively. Only five other beds (118, 119, 120, 121, and 124) contain Mo measurements that are above the detection limit (2 ppm), but none exceed 10 ppm. Mo values of 0-20 ppm are correlated to non-euxinic conditions, 20-40 ppm to possible euxinia, 40-70 ppm to seasonal euxinia, and 70-90 ppm to possible well-established euxinia, and Mo values >90 ppm are diagnostic of persistent euxinic conditions (Formolo et al., 2014). However, Mo values can underestimate actual euxinic conditions due to Mo sequestration overtaking Mo resupply under sulfidic and euxinic conditions (Algeo, 2004). In these cases, additional proxies can be used, such as Mo/TOC ratios (Algeo and Lyons, 2006). The largest Mo/TOC ratio (>20) is in bed 116 (Fig. 7) and may indicate sulfidic depositional conditions (Algeo and Lyons, 2006). Therefore, the Mo > 90 ppm in bed 116 indicates highly euxinic conditions, consistent with the HBS Event.

Vanadium (V) ratios, such as V/Cr and V/(V+Ni), are also commonly used as redox proxies and have been used in a variety of studies. Other sections that record the D-C boundary in mudstones or mixed lithologies have shown dramatic increases in V/Cr through the HBS (Beier and Hayes, 1989; Caplan and Bustin, 1998; Marynowski et al., 2012; Perkins et al., 2008; Rimmer, 2004). Early work by Ernst (1970) and Jones and Manning (1994) suggested that sedimentary V/Cr values >4.25 record anoxia, 2.0-4.5 record dysoxia, and <2.0 record fully oxic conditions. Hoffman et al. (1998) and Averbuch et al. (2005) countered that V/Cr = 1.0 is the dysoxic-anoxic boundary, and values 1-5 are anoxic. Modern euxinic environments including the Black Sea, the Cariaco Basin, the Saanich Inlet, and the Framvaren Fjord have V/Cr values ranging between 0.68 and 2.25 (calculated from Algeo and Maynard, 2004). The boundary between oxic and anoxic conditions as recorded by V/Cr ratios obviously varies with different studies, but in general increasing V/Cr ratios have been correlated with increased anoxia (e.g. Marynowski et al., 2012). Using the V/Cr criteria of Jones and Manning (1994) and Ernst (1970), most of the section is oxic, with the exception of beds 109, 110, 111, 116, and 123 (Fig. 6). Using the criteria of Hoffman et al. (1998), Averbuch et al. (2005), and Algeo and Maynard (2004), the entire section is anoxic (Fig. 7).

In the case of the Cat Co 3 section, V/(V+Ni) is possibly a better redox proxy than V/Cr because Cr has a strong detrital influence (Tribovillard et al., 2006), whereas V and nickel (Ni) are better preserved under anaerobic depositional conditions (Hatch and Leventhal, 1992). According to Hatch and Leventhal (1992), V/(V+Ni) ratios ≤0.46 indicate oxic conditions, >0.46 and ≤0.60 indicate dysoxic conditions, >0.54 and ≤0.82 indicate suboxic to anoxic conditions, and >0.84 indicate euxinia. All beds have V/(V+Ni) values equal to or greater than 0.5., indicating prolonged dysoxia as a minimum estimate (Fig. 7). A majority of the beds record suboxic to anoxic conditions, and beds 104, 115a, 124, and 126 record euxinia.

Cobalt (Co), antimony (Sb), and thallium (Tl) can also be used as redox proxies (Brumsack, 2006; Piper and Calvert, 2009), but only Tl is not lithologically controlled (Tribovillard et al., 2006) (values provided in Supplemental Table S2 and in Figs. S1-S3). Given the somewhat inconclusive and/or contradictory results from proxies with a strong detrital influence (all proxies containing Cr and Co) or proxies with numerous speciation complications (Ce_{anom}) (Fig. S7; also discussed in detail in the supplemental data), concurrent enrichments in U, V, Mo, S and TOC may be better indicators of anoxia and euxinia for the Cat Co 3 section. Correlated enrichments in these elements and TOC indicate euxinic conditions, because under reducing conditions most of these ions form insoluble precipitates or are adsorbed onto organic material (Hoffman et al., 1998; Tribovillard et al., 2006). This coupling is seen only in beds 116-118, which are within the expected HBS Event interval. Therefore, we conclude that the most severe anoxia/euxinia is recorded in strata 116-118, representing the interval of the Hangenberg Crisis, but also suggest that the basin experienced oxygen stress (dysoxic/suboxic conditions) throughout the history documented here.

4.1.4. Productivity proxies

Phosphorous is commonly used as a proxy for biological productivity, necromass deposition, or secondary eutrophication (Middelburg and Levin, 2009; Schmitz et al., 1997; Tribovillard et al., 2006). In the Cat Co 3 section, P_2O_5 is enriched in beds 116 and 117 (Fig. 8). Although Tribovillard et al. (2006) note that Ba enrichments are rarely affected by detrital provenance, anoxic depositional environments and the degree of sulfate reduction can lead to dissolution or undersaturation of barite (McKay and Pedersen, 2008). Furthermore, Ba can vary with water depth, and barite preservation can also vary with sedimentation rates (Dymond et al., 1992; McKay and Pedersen, 2008). Although excess barium (Ba) increases in the expected HBS Event interval in the Cat Co 3 section (Fig. 8), it is probably an unreliable paleoproxy due to the prolonged suboxic/dysoxic depositional environment indicated by many of the redox proxies (discussed in *4.1.3*).

Excess SiO_2 is a proxy for biogenic opal (Schmitz et al., 1997) or the presence of algal cysts (Schieber et al., 2000). There are no other aluminosilicate minerals besides illite in the measured section (mineralogy confirmed by SEM-EDS and XRD), so excess SiO_2 is used as a productivity proxy to determine the percentage of SiO_2 that is not incorporated into the illite fraction of the sediment. For the Cat Co 3 section, excess SiO_2 = SiO_2 - (Al_2O_3 + K_2O + Na_2O + 0.6*MgO); FeO is not included in the excess SiO_2 calculation as SEM-EDS analysis did not indicate the presence of Fe in the illite grains. There are positive excursions in excess SiO_2 in beds 116, 117, and 121, indicating the presence of biogenic silica (Fig. 8).

Copper (Cu) and zinc (Zn) are micronutrients that are enriched during necromass deposition and are usually included as solid solution phases in pyrite (Tribovillard et al., 2006). Both Cu and Zn are enriched within beds 116-117 interval (Fig. 8), consistent with enrichments in S (Fig.

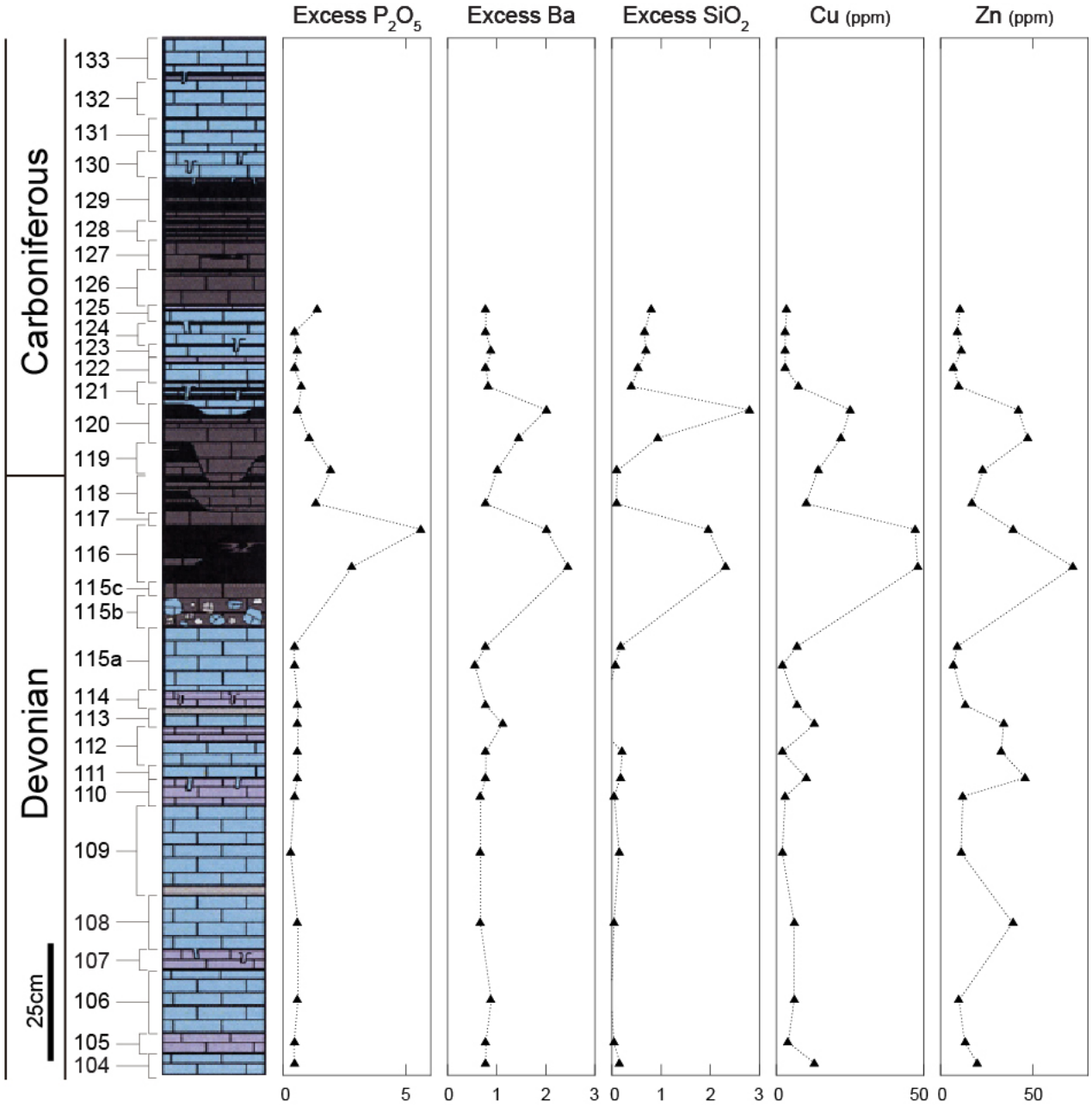

Figure 8. Chemostratigraphy plots of common productivity proxies, including excess P_2O_5, excess Ba, excess SiO_2, Cu, and Zn. All show increased productivity in beds 116-117. Enrichment factors and normalization to Al were not used due to low Al concentrations (see 4.1.1 in text for justification).

6). Taken together with the TOC values, the productivity proxies (excess P_2O_5, excess Ba, excess SiO_2, Cu, and Zn) do indicate an increase in productivity recorded in the expected HBS Event interval.

4.1.5 Hydrothermal activity and impact event geochemical proxies

Potential hydrothermal influences can be distinguished from terrestrial inputs by sedimentary REE signatures and Al/(Al+Fe+Mn) ratios (Huang et al., 2013; Kalvoda et al., 2018; Kumpan et al., 2019; Racki et al., 2002; Xu et al., 2008; Zeng et al., 2011); these data are provided in Figs. S4-S5. Al/(Al+Fe+Mn) signatures in the Cat Co 3 section are obscured by the extremely low Al values in the section, but REE concentrations are elevated in beds 116-117 and 124 (Fig. S5). These higher concentrations of REEs in the beds associated with the HBS Event could be a function of illite clay adsorption rather than increased hydrothermal activity, however. Despite the increased REE amounts in beds 116-117, PAAS-normalized REE signatures are all remarkably consistent with each other with the exception of bed 124 (Fig. S4), which shows relative enrichment in the heavy REE elements and a pronounced europium anomaly, suggesting the presence of terrestrially-derived plagioclase in the rock (although plagioclase was not noted in SEM-EDS or XRD analysis of bed 124). Although

hydrothermal activity was likely occurring on the South China tectonic block during deposition of the Cat Co 3 section (Chen et al., 2006), the section itself does not record the presence of significant hydrothermal activity.

Meteorite impacts were initially invoked as a potential cause of Late Devonian extinction events, both in southern China and Australia using iridium (Ir) anomalies (Bai, 2001; Playford et al., 1984; Wang et al., 1993; Wang et al., 1991). Both Racki (2012) and Wang et al. (1993) state that Ir anomalies do not form sufficient evidence for a meteorite impact and simply record local anoxic/euxinic conditions, and Bai (2001) shows that the mineral chemical compositions of D-C beds containing Ni-Ir anomalies suggest a submarine hydrothermal source of Ir. Ir anomalies in four samples of the Cat Co 3 section (above 1 ppb background levels, shown in Table S2) are therefore most likely associated with local redox conditions rather than impact events.

4.2. Principal component analysis

Due to the somewhat contradictory geochemical signals of some of the trace elements that are associated with a strong detrital component, principal component analysis (PCA) was used to clarify trace element enrichment and correlation between samples. PCA is a statistical analysis tool rooted in linear algebra. PCA is used to emphasize and visualize variations in multidimensional datasets, particularly to determine which elements or proxies account for the most geochemical variation in the samples. This method can reveal which samples are relatively enriched in certain elements. In cases like the Cat Co 3 section where the detrital component is minimal and the standard Al and EF normalizations are inappropriate to use (*4.1.1*), PCA is a particularly useful tool.

PCA of major, minor, trace, and rare earth elements (Fig. 9a) shows that the most variance is caused by changes in mineralogy, with the largest variations in silicon (Si), aluminum (Al), Fe, manganese (Mn), calcium (Ca), potassium (K), and titanium (Ti). Beds 115-117, 119-121, and 126 plot positive on the PCA 1 axis, indicating either a detrital component or a relative lack of carbonate deposition compared to the other beds. The rest of the beds are relatively enriched in Ca, indicating a carbonate-rich lithology. These findings are consistent with SEM-EDS observations. PCA of only trace elements and the geochemical proxies described in 4.1.3 and 4.1.4 reduced the influence of lithology in the analysis (Fig. 9b). Positive values on the PCA 1 axis display relative enrichment in Mo, Cu, Ni, arsenic (As), Co, Ce, lanthanum (La), excess SiO_2, and excess Ba, indicating coupled anoxia and increased primary productivity. Samples that are positive on the PCA 1 axis are beds 113, 116-121, and 124, which is consistent with the expected location of the HBS Event, at least for beds 116-121.

Using PCA plots (Fig. 9) in combination with standard chemostratigraphy (Figs. 5-8) can help decipher some of the processes involved in sediment deposition. While it is possible to determine the mechanism of trace element transport in water columns that are generally oxic using the covariation of Fe, P, Mo, As, and Sb, this process is obscured in anoxic water columns (Tribovillard et al., 2015). One way to determine if the particulate shuttle or framboidal pyrite deposition from anoxic waters is the cause of elevated Mo, As, and Sb in organic-rich rocks is via comparison with U; these elements will all be coupled when they are deposited from an anoxic water column, but U will be decoupled from the group in the case of metal deposition via Fe particulate shuttles (Tribovillard et al., 2015). In the case of the Cat Co 3 section, U concentrations are generally coupled with the metals, indicating deposition under anoxic conditions (Fig. 9b).

4.3 Framboidal pyrite

Circular aggregates of pyrite microcrysts (pyrite framboids) and their shape, size, and distribution can indicate varying degrees of dysoxia, anoxia, or euxinia in the water column (Wignall and Newton, 1998; Wilkin and Barnes, 1997; Wilkin et al., 1996; Wilkin et al., 1997). Framboids that formed in anoxic water columns tend to have a narrow size range, with individual framboids <5 μm in diameter, and be dispersed uniformly throughout the sediment rather than in large clumps or within burrows (Bond et al., 2004; Carmichael et al., 2016; Wang et al., 2013; Wignall and Newton, 1998; Wilkin and Barnes, 1997; Wilkin et al., 1996; Wilkin et al., 1997). Framboids in fluctuating dysoxic/oxic/anoxic/suboxic environments are typically larger and more variable in size, and less abundant (Wignall and Newton, 1998). A lack of framboids usually indicates oxic conditions, but can also be explained by rare euxinic depositional environments where the amount of available Fe is insufficient to form framboids (Wilkin and Barnes, 1997). Framboids that are found in burrows or pore spaces, as well as ovoid-shaped framboids that are >25 μm in diameter likely formed at or below the sediment-water interface and do not indicate water column anoxia (Carmichael et al., 2016; Rowan et al., 2009; Wang et al., 2013). Histogram shapes of the size distribution of framboids (Fig. 10) also provide useful information about the degree of water column anoxia (Wignall and Newton, 1998).

Framboidal pyrite is abundant in all analyzed samples from the section, and these framboids are generally very small (<10 μm). Nine representative samples (beds 104, 110, 115, 116, 117, 118, 121, 124, and 126) were analyzed in detail for pyrite framboid size distributions (Fig. 11). Mean framboid size ranged between 4 and 7 μm, with most measured framboid diameters between 4 and 5 μm. Framboid sizes < 3.5 μm could not be accurately measured at the resolution used for the image processing and are not included in this analysis. Beds 116 and 117 have an order of magnitude more framboids than the surrounding beds, as shown by the first column of histograms in Fig. 9, which may also explain their elevated sulfur content (Fig. 6). The average framboid sizes in beds 116 and 117 are 4.56 μm and 4.26 μm, respectively, indicating deposition under anoxic to euxinic water conditions. Histogram shape comparisons between individual beds (Fig. 11) and previous studies (Fig. 10) suggest that the lower part of the

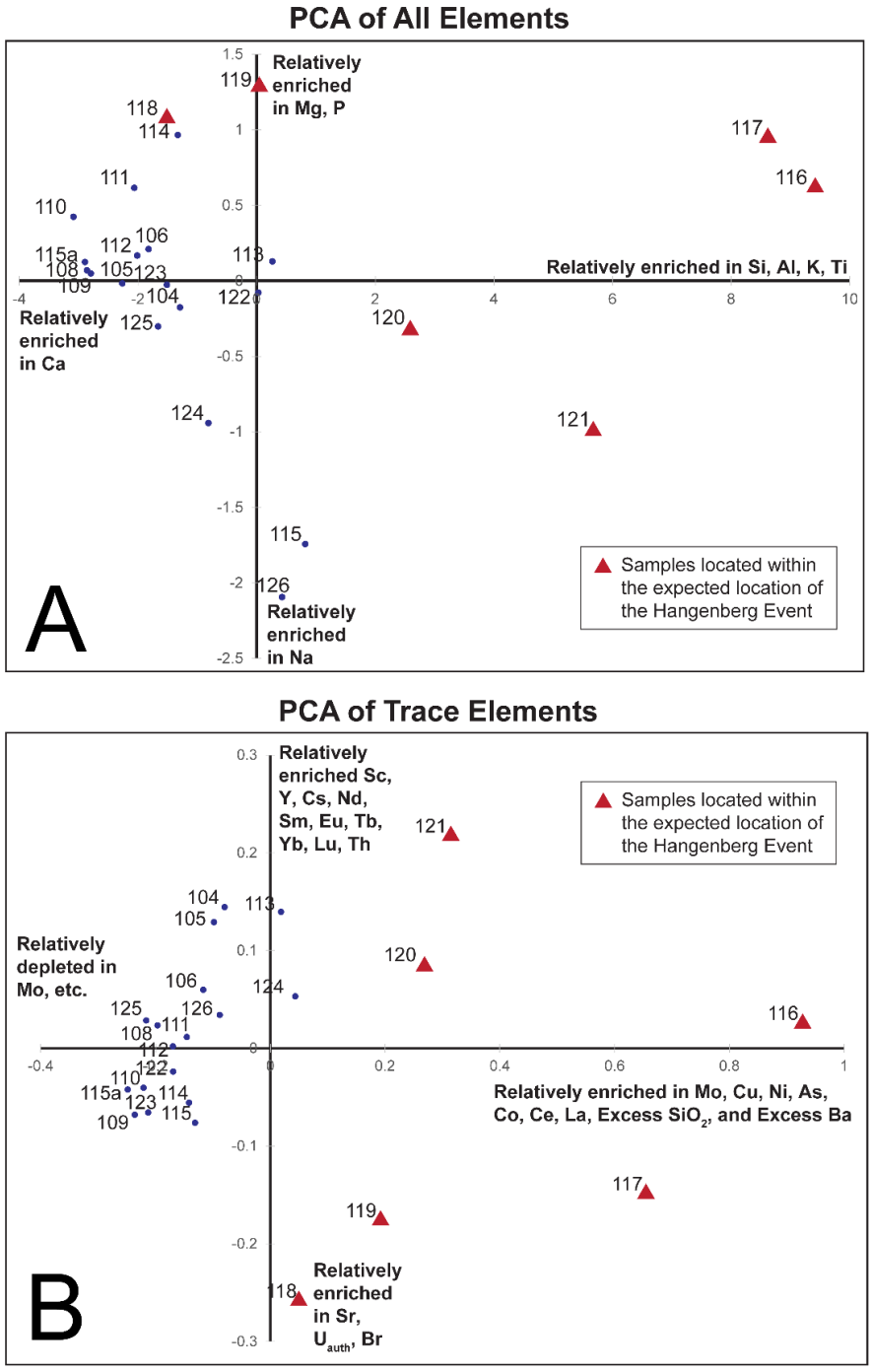

Figure 9: (A) Principal component analysis (PCA) of all elements, including major and trace elements. The major elements account for the most variation within all samples (Si, Al, K, Ti, and Ca). The red triangles represent beds that are near the expected location of the Hangenberg Crisis. (B) PCA of trace elements (all major elements removed from analysis). The beds surrounding the expected location of the Hangenberg Crisis are relatively enriched in Mo, Cu, Ni, As, Co, Ce, La, excess SiO2, and excess Ba, most of which are indicative of anoxic depositional environments or increased productivity.

section (beds 104, 110, and 115) ranges from depositional conditions that are intermittently dysoxic to upper dysoxic, anoxic to euxinic for beds 116 and 117, and upper dysoxic for the upper part of the section (beds 121, 124, and 126).

All analyzed samples within beds 104-126 contain disseminated framboids, revealing that the basin remained at least dysoxic throughout most of its history. This interpretation is consistent with redox proxies (discussed in *4.1.3*) that also show persistent, long-term dysoxic conditions within the basin. The exception is beds 116 and 117, which (regardless of proxy) exhibit highly anoxic to euxinic conditions, and are within the expected biostratigraphic location of the HBS Event.

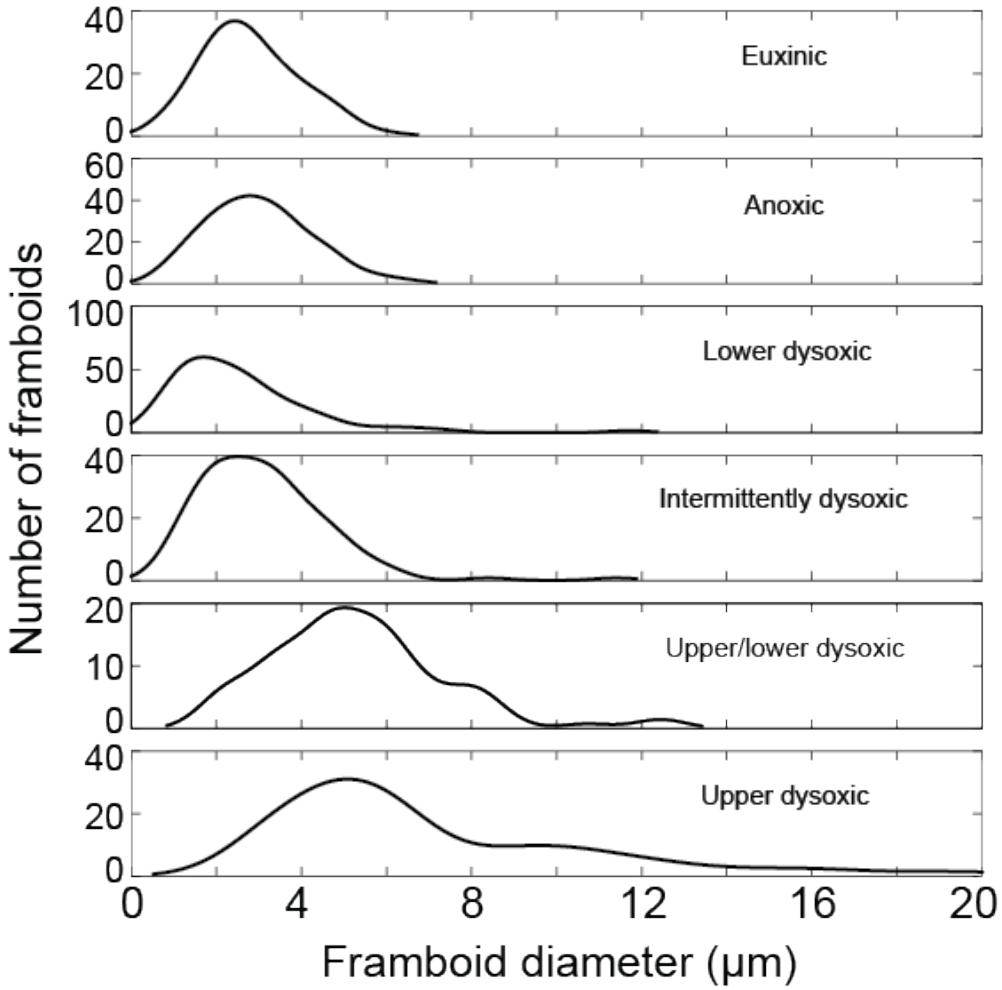

Figure 10. Size distributions of framboids from depositional environments with variable degrees of anoxia. Histogram density functions were computed using the kernel distribution fit in MATLAB. Data from Wignall and Newton (1998).

4.4. Stable isotopes

Although preliminary carbon isotope data of Komatsu et al. (2012b) suggested a series of positive $\delta^{13}C$ values for bulk carbonate in beds 114-116, 117-119 and 124-129, newer data presented in this study do not show any distinct trends throughout the section, either in $\delta^{13}C_{carb}$ or $\delta^{13}C_{org}$ (Fig. 12). While there are positive $\delta^{13}C_{org}$ excursions of ~1.5‰ VPDB in beds 116 and 121, these conflict with the $\delta^{13}C_{carb}$ data, which do not show excursions in these beds. Furthermore, the $\delta^{13}C_{carb}$ signatures show significant scatter (up to 2‰) in beds 118-123, but they are relatively stable through the HBS Event beds.

Many studies from Europe show a positive (up to 3‰) $\delta^{13}C_{carb}$ excursion across the Hangenberg Crisis (Buggisch and Joachimski, 2006; Kaiser et al., 2016; Kaiser et al., 2008; Kaiser et al., 2006; Kumpan et al., 2014a; Kumpan et al., 2014b). This excursion is not ubiquitous for all locations, however, and excursions may be offset into the surrounding strata, or not present at all (Brand et al., 2004; Cramer et al., 2008; Kumpan et al., 2014a; Kumpan et al., 2014b). The sites that do not exhibit positive $\delta^{13}C$ signatures may be affected by stratigraphic gaps, problems with biostratigraphic control, and/or paleoenvironmental bias (as discussed in Bábek et al., 2016; Carmichael et al., 2016), so the absence of an *obvious* positive $\delta^{13}C$ excursion at the HBS Event does not negate carbon cycle perturbations. This is similar to other D-C boundary sites within the South China cratonic block, where there are inconsistent $\delta^{13}C$ values across the Hangenberg Crisis (Bai et al., 1994; Liu et al., 2016; Qie et al., 2015). We are reluctant to correlate the $\delta^{13}C$ excursions shown in this data to global excursions due to the condensed nature of the section, contradictions between carbonate and organic carbon signatures, and the high degree of variability within the data.

$^{87}Sr/^{86}Sr$ isotope ratios (Fig. 12) are similar to the value of the global curve at the D-C transition presented in McArthur et al. (2012). Therefore, the section records a strontium signature that is generally close to Late Devonian global seawater chemistry, does not indicate diagenetic alteration, and does not indicate major changes in $^{87}Sr/^{86}Sr$ across the D-C boundary. The values in this study show less variability across the D-C boundary than earlier work by Kürschner et al. (1993) and Brand et al. (2004) in Europe and by Carmichael et al. (2016) in the Central Asian Orogenic Belt, but these differences may be due to differences in sample type and/or methodology between each of the studies.

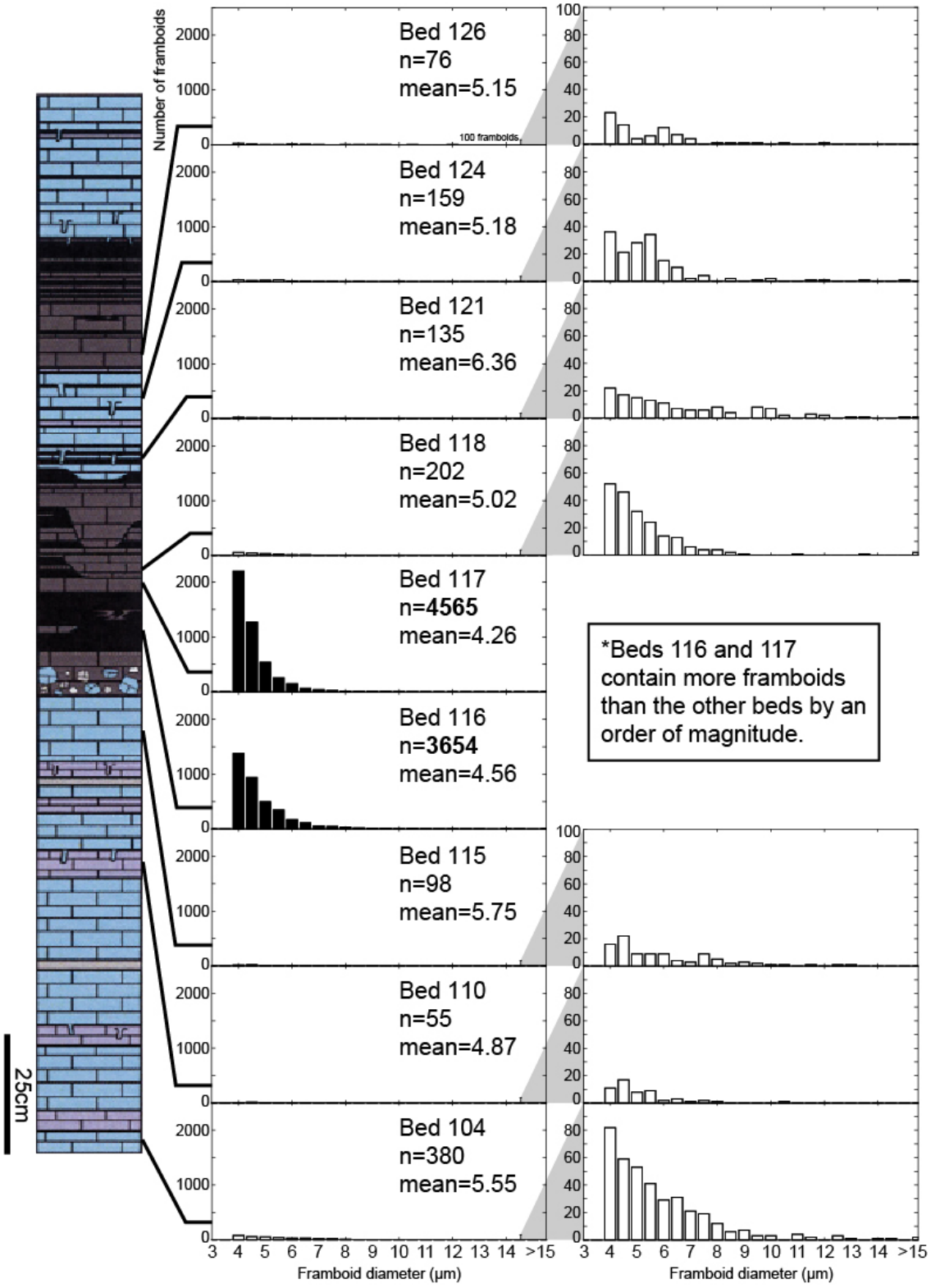

Figure 11. Abundance and size distribution of pyrite framboids in representative samples throughout the section. Framboid diameter bin size for histograms is 0.5 µm. Graphs on the left represent framboid distributions for all beds; graphs on the right represent framboid distributions for beds with <1000 framboids per cm^2.

4.5 Hg chemostratigraphy and volcanism proxies

Mercury (Hg) chemostratigraphy can be very useful for correlating the timing of sediment deposition with volcanic events, as volcanism is the largest natural source of Hg, which has a relatively long residence time in the atmosphere (0.5 - 2 years) that allows for wide distribution in the sedimentary record (Bergquist, 2017; Charbonnier et al., 2017; Grasby et al., 2016; Percival et al., 2017; Thibodeau et al., 2016 and others). Positive mercury anomalies have been linked to large-scale volcanism (Bergquist, 2017; Grasby et al., 2016; Percival et al., 2017; Racki et al., 2018b), although other mechanisms of Hg deposition are possible (see discussion in Thibodeau and Bergquist, 2017), including complexation with organic matter or hydrous Fe oxides (Charbonnier et al., 2017), terrestrial runoff (Them et al., 2019), or deposition during fluctuating redox processes (Percival et al., 2017).

Within the Cat Co 3 sediments surrounding the D-C boundary, a marked Hg enrichment exceeding 1000 ppb is present (Fig. 13). To refine the mode of deposition, Hg was normalized to Al, Fe, S, and TOC values (Fig. 13). Hg/Al normalization reduces the signature of potential detrital or local volcaniclastic source material, resulting in excursions across the HBS Event and D-C boundary interval. The Cat Co 3 section sediments have an extremely low detrital component (*4.1.1*), so a detrital (i.e. fluvial) Hg source is unlikely and atmospheric deposition is a more reasonable source, consistent with a volcanic signature. This interpretation is consistent with the conclusions of Them et al. (2019) for Hg anomalies in Pliensbachian-Toarcian distal, deep-water environments.

Normalization to Fe minimizes the Hg component due to complexation to hydrous Fe oxides, and normalization to S reduces the effect of Hg sequestration into pyrite under anoxic conditions (which the section experienced). Normalization of Hg to TOC can unfortunately result in anomalously high Hg/TOC spikes in beds with very low TOC (Grasby et al., 2016; Percival et al., 2017); many of the Famennian beds with TOC levels below the detection limit in the Cat Co 3 section are likewise problematic. Conversely, Hg/TOC signatures in beds with very high TOC values (such as beds 116-117 in the Cat Co 3 section) may show anomalously low Hg/TOC ratios, consistent with observations in various Mesozoic sediments (Charbonnier and Föllmi, 2017; Percival et al., 2015). Thus, the combination of enhanced Hg deposition with a rapid increase in biological productivity can complicate the interpretation of Hg excursions. Further complicating matters, the presence of up to 2% illite clay in beds 116-117 may slightly elevate the Hg signature of these beds compared to the surrounding beds, as experimental data shows that Hg tends to sorb to illite vs. other minerals at seawater pH conditions (Reimers and Krenkel, 1974). This adsorption process has likewise been observed in the rock record (Sial et al., 2013). Therefore, Hg results are provided in both normalized and non-normalized formats (Fig 13, Table 1) to best view the data.

Table 1. Hg, TOC, Al_2O_3, Mo data as well as Hg/TOC and Hg/Al_2O_3 ratios from the Pho Han Formation, using the methodology of Racki et al. (2018b). NA = Hg not analyzed (also gray shading). The last column shows which beds have TOC=0, for which we substituted TOC=0.08 (~3/4 detection limit) for Hg/TOC calculations. Green shading represents data points that are greater than three times the median value. Yellow shading represents elevated values above the median (but less than three times the median value). The median values of Hg, Hg/TOC, and Hg/Al_2O_3 are 20 ppb, 100, and 67, respectively.

Sample	Hg (ppb) M = 20	TOC (%)	Al_2O_3 (%)	Mo (ppm)	Hg/TOC M = 100	Hg/Al_2O_3 M = 67	TOC approximated?
VN06-104	18	0.08	0.37	4	225	49	yes
VN06-2014-105	20	0.2	0.26	5	100	77	
VN06-2014-106	14	0.08	0.30	6	175	47	yes
VN06-2014-108	NA	0.08	0.18	4	NA	NA	yes
VN06-2014-109	NA	0.08	0.16	4	NA	NA	yes
VN06-2014-110	NA	0.5	0.13	5	NA	NA	
VN06-2014-111	NA	0.08	0.19	7	NA	NA	
VN06-112	21	0.1	0.25	5	210	84	
VN06-2014-113	18	0.1	0.68	21	180	26	
VN06-2014-114	36	0.08	0.25	6	450	144	yes
VN-115	19	0.08	0.89	7	237.5	21	yes
VN06-115A	10	0.5	0.17	2	20	59	
VN-116	548	5.3	2.29	58	103	239	
VN-117	649	5.8	1.91	32	112	340	
VN06-2014-118	1090	0.7	0.20	5	1557	5450	
VN06-2014-119	372	4.1	0.42	14	91	886	
VN06-2014-120	132	2	1.01	33	66	131	
VN06-2014-121	30	0.8	1.58	35	38	19	
VN06-122	51	4.5	0.48	6	11	106	
VN06-2014-123	11	3.5	0.23	6	3	48	
VN06-2014-124	15	0.7	0.45	5	21	33	
VN06-2014-125	16	0.9	0.24	4	18	67	
VN06-126	13	0.2	0.81	3.5	65	16	

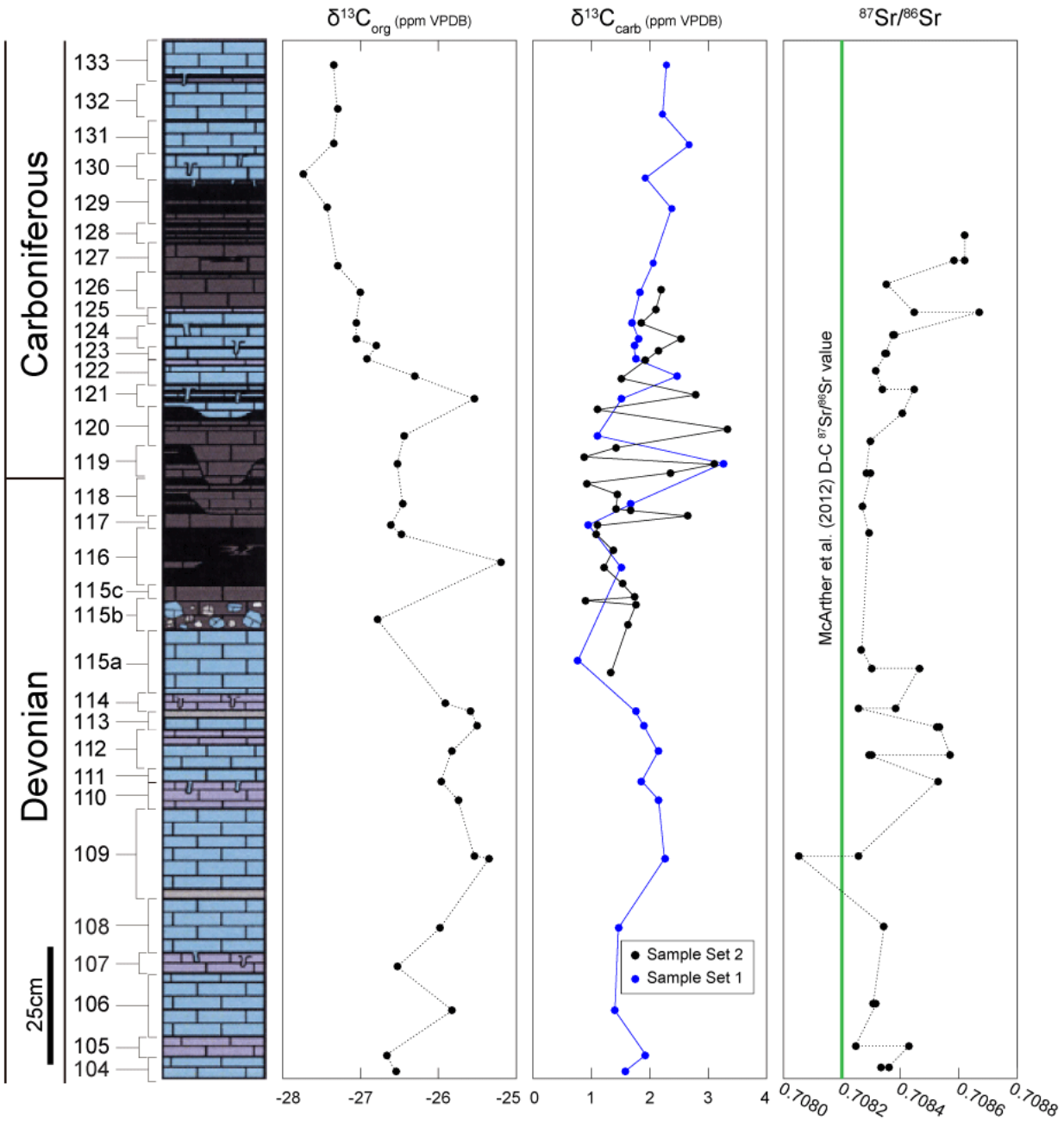

Figure 12. Chemostratigraphy of isotope geochemistry for $\delta^{13}C_{carb}$, $\delta^{13}C_{org}$, and $^{87}Sr/^{86}Sr$. There are potential positive $\delta^{13}C_{org}$ excursions in beds 116 and 121, but these are based on a single data point, and do not match the excursions in $\delta^{13}C_{carb}$. The $\delta^{13}C_{carb}$ data shows significant variation starting in bed 117 up through bed 121, based on measurements from two separate sample sets (shown by black and blue markers, where the black markers of Sample Set 2 represent a more concentrated sampling interval compared to Sample Set 1, shown by the blue markers). Although it is possible that this increase in variability represents a positive excursion, the expression is masked and $\delta^{13}C$ results are inconclusive at this time. $^{87}Sr/^{86}Sr$ values represent relatively stable values throughout the HBS and HSS intervals that are similar to modeled $^{87}Sr/^{86}Sr$ composition of Devonian-Carboniferous seawater using the LOWESS model of McArthur et al. (2012).

Smit et al. (2016) and Zhu et al. (2018) note that Hg can migrate up-section via dissolution/reprecipitation reactions when anoxic sediments are overlain by a more oxic facies. As the Cat Co 3 section is extremely condensed and contains both high TOC values and evidence for anoxia/euxinia in HBS Event beds 116-117, Hg may have migrated from the underlying 116 and 117 beds up into D-C boundary bed 118, leading to the extremely high Hg/TOC, Hg/Fe, and Hg/S signatures in bed 118. The high Fe, U, Zn, S, and As values in beds 116-117 likewise support a scenario with Hg upward mobility due to dissolution/reprecipitation within underlying anoxic sediments, per the criteria of Smit et al. (2016).

Using the methodology of Racki et al. (2018b), Hg/TOC anomalies exceeding 3x the median Hg/TOC values for the section are categorized as volcanic in source (Table 1). For beds where TOC was below the detection limit (104, 106, 114, and 115), we substituted the value 0.08 for estimating Hg/TOC values, per the methodology of Racki et al. (2018a). Hg anomalies are detected in beds 114 and 118

of the Cat Co 3 section (Table 1), while beds 116-117 have elevated Hg/TOC values that correspond neatly with the HBS Event and D-C transition. Only one Hg anomaly is *undoubtedly* recorded in bed 118, which has Hg/TOC, Hg/Fe, and Hg/S values that are distinctly higher than all the others (Fig. 13).

In addition to Hg, Ti/Al and Zr/Al values have also been used as a proxy for volcanic input in sediments (Kumpan et al., 2019; Marynowski et al., 2012; Pujol et al., 2006; Racki et al., 2002; Racki et al., 2018b; Suzuki et al., 1998; Yudina et al., 2002), but their utility is limited in the Cat Co 3 section due to the extremely low Al values throughout the section (as discussed in detail in *4.1.1*). Zr/Al does not show an excursion in bed 118, but does show a marked excursion in bed 115 (Fig. 13). This excursion in bed 115 is inconsistent with the Hg excursions in beds 116-118, and may simply reflect a single outlier data point, due to lack of coupling with expected analogous Ti/Al excursions (Fig. 5) or elevated REE, U, and Y concentrations (Table S2) that would be expected if there was a significant zircon concentration in bed 115. The Zr/Al excursions in beds 116 and 117 are somewhat masked by their higher Al content in comparison with bed 115. The Ti/Al data do not show any particular trend, but the highest values are in beds 116 and 122. Due to limited use of Al-normalized proxies in this section, however, Hg/TOC, Hg/Fe, and Hg/S are more appropriate proxies for volcanic input.

Although background (Famennian) Hg values are somewhat difficult to assess for the Cat Co 3 section, an Hg-cycle perturbation did occur near the D-C boundary and HBS Event, consistent with D-C boundary sections in Germany and Uzbekistan (Racki et al., 2018a). It is clear that Hg cycling is more complex in natural systems than in the laboratory, and measurements of Hg isotopes (which are outside the scope of this study) would be a more robust method of determining Hg sources, sinks, and pathways in the rock record (Grasby et al., 2017; Thibodeau and Bergquist, 2017). Due to its low detrital component, the Cat Co 3 section of the Pho Han Formation would be an excellent candidate for Hg isotope analysis of the D-C boundary.

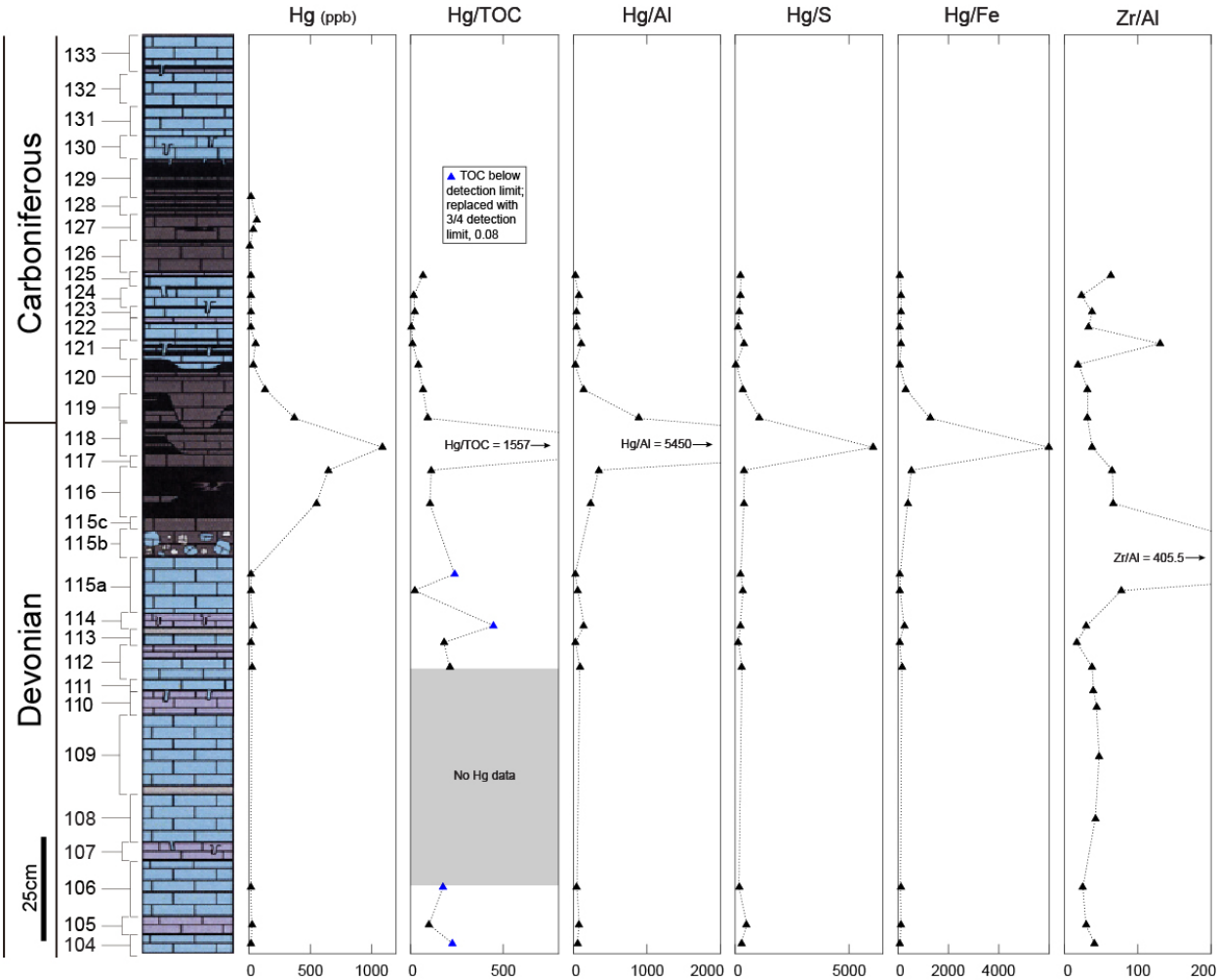

Figure 13. Chemostratigraphy of volcanism proxies. Beds 116-120 all show total Hg above background levels, while Hg/TOC, Hg/Al, Hg/S, and Hg/Fe all show a significant spike at bed 118 (at the D-C boundary). Blue markers in the Hg/TOC graph indicate TOC values below the detection limit. Zr/Al shows an anomalous enrichment in bed 115, but Hg and other lithology proxies (Fig. 5) do not support a volcanic contribution in this bed, so this may be an outlier data point.

5. Summary, Implications and Conclusions

The Hangenberg Black Shale (HBS) and Hangenberg Sandstone (HSS) events have been studied extensively in mudstones and mixed lithologies along active margins and within the epeiric seas of large continental blocks of Laurussia and northern Gondwana, so it is important to determine in what ways these events are preserved in different paleogeographic and paleoenvironmental locations. Although trace element anoxia and productivity proxies are not always reliable in carbonates with very low detrital input, they are very useful for identifying anoxia events when used in conjunction with PCA and pyrite framboid distributions.

5.1 Detection of the HBS and HSS Events

Using this multi-proxy approach, our study shows that the HBS Event was present in a sediment-starved basin that was experiencing long-term oxygen stress. During the HBS Event (recorded in beds 116-117) the normally dysoxic to anoxic water column became euxinic and the basin experienced a total shutdown of the carbonate factory. A regressive equivalent to the HSS Event is not obvious in the major/trace element data nor in the sediment composition and texture (as observed in SEM-EDS) of the Cat Co 3 section. It is possible that the Cat Co 3 section was isolated enough within the basin that gravity-flow sediment transport associated with the HSS Event did not reach it (see schematic model in Fig. 11 of Bábek et al., 2016), as the sequences in the South China block represent a variety of paleoenvironments that had complex water circulation among numerous platforms and basins (Liu et al., 2016). Conversely, the lack of preservation of an HSS Event could be due to local tectonic forces (Komatsu et al., 2014), as tectonic reconstructions of this region during the Late Devonian are still debated (Halpin et al., 2016; Lai et al., 2014; Osanai et al., 2004). The occurrence of shallow-water organisms (solenoporids) in bed 117 (Komatsu et al., 2014) provides conjectural evidence for a sea level fall (equivalent to HSS?), but an obvious sedimentological record of transgressive-regressive cycles in this deep, offshore paleoenvironment is lacking.

5.2 Mechanisms for Anoxia

The mechanism for anoxia in the Pho Han Formation is not entirely clear. Upwelling of nutrient-rich waters into basins during transgression is commonly invoked as a causal mechanism for anoxia within the HBS Event, both in the Cat Co 3 section (Komatsu et al., 2014) and elsewhere (Algeo et al., 2007; Caplan and Bustin, 1999; Caplan et al., 1996; Cramer et al., 2008; Formolo et al., 2014; Komatsu et al., 2014; Smith and Bustin, 1998). Others disagree, and suggest that HBS anoxia was a result of eutrophication due to runoff from terrestrial sources (Averbuch et al., 2005; Bábek et al., 2016; Caplan and Bustin, 1998; Carmichael et al., 2016; Liu et al., 2016; Qie et al., 2015). As there are no obvious terrestrial sources that have contributed to sediment deposition in the Cat Co 3 section, the eutrophication due to terrestrial runoff scenario is unlikely. It is possible that changes in plankton and microbial populations at the D-C boundary contributed to the rise in primary productivity (Riding, 2009; Yao et al., 2016), although Martinez et al. (2018) do not note any particular changes in either abundance or community structure in microbial populations preserved in the rock record through the HBS Event. Organic biomarker analysis of the Cat Co 3 section could help to resolve this question.

5.3. Volcanism at the D-C boundary

A link between Hg anomalies, massive volcanism, and mass extinctions has recently been suggested for a number of different environmental crises in Earth's history (Bergquist, 2017; Charbonnier and Föllmi, 2017; Charbonnier et al., 2017; Font et al., 2016; Percival et al., 2015; Percival et al., 2017; Sial et al., 2013; Thibodeau and Bergquist, 2017; Thibodeau et al., 2016), and now includes both the Frasnian-Famennian (F-F) and D-C boundaries in the Late Devonian (Racki et al., 2018a; Racki et al., 2018b). Hg enrichment is present at/near the HBS Event and D-C boundary beds (116-118) in the Cat Co 3 section (Fig. 13), and as there is no obvious *local* source of Hg for these sediments, the presence of Hg anomalies in a sediment-starved carbonate basin is particularly notable. Bed 118 at the D-C boundary shows particularly high Hg enrichment, but as this location is stratigraphically above the base of the HBS Event, it technically should refute the hypothesis that massive volcanism triggered the climatic changes leading to the Hangenberg Crisis. Furthermore, the combination of Hg enrichments with positive $\delta^{13}C$ values in the rock record precludes biomass/soil burning as a source of Hg (Bergquist, 2017). However, the mechanisms of Hg preservation in the rock record are still debated (Bergquist, 2017), particularly as Hg speciation and deposition are dependent on local redox conditions and availability of organic matter (Outridge et al., 2007), and Hg sequestration is dependent on post-depositional processes (Moreno et al., 2018; Smit et al., 2016; Zheng et al., 2018). It is therefore possible that Hg deposition happened in the lower HBS Event interval and then migrated upward to the D-C boundary in bed 118 (see discussion in *4.5* for details).

One of the complications of correlating Late Devonian Hg anomalies with LIPs is a lack of obvious LIP candidates in the rock record. While many of the other major mass extinctions are known to be associated with LIPs (Bond and Wignall, 2014; Kravchinsky, 2012), there are no LIPs that have *definitively* been associated with any of the Late Devonian biotic crises. The F-F extinction has been linked to LIP activity at the Viluy Traps in Siberia (Courtillot et al., 2010; Rodionov et al., 2018; Tomshin et al., 2018), the Khibiny Massif (Rodionov et al., 2018), rift basalts in eastern Europe (i.e. the Kola, Vyatka, and Pripyat–Dniepr–Donets systems) (Kravchinsky, 2012), massive and widespread arc volcanism (Racki et al., 2018b), and submarine volcanism (Xu et al., 2008). New and more precise U/Pb dates for the F-F boundary are helping to refine associations between the F-F extinction and potential LIP activity in Russian and eastern European rift systems, whose ages are still not well-constrained (Percival et al., 2018).

Until very recently, the D-C boundary has not been associated with large scale volcanism. Racki et al. (2018a) used Hg chemostratigraphy to suggest that widespread volcanism was occurring at the D-C boundary in both Germany and Uzbekistan, despite the lack of an obvious LIP candidate. LIP magmatism is not out of the question, as the lack of preservation of a LIP does not preclude the original presence of one (Percival et al., 2018). Instead of a single LIP candidate for the Hg source, Racki et al. (2018b) suggested that widespread explosive arc volcanism (in combination with ongoing environmental stressors) triggered the F-F biotic crisis, which is consistent with the extensive volcanic arc systems that were active in the Late Devonian (i.e., the Variscan/Appalachian orogen, the Central Asian Orogenic Belt, etc.). Furthermore, sources for catastrophic, explosive volcanism from arc volcanoes (versus LIPs) rarely remain in the rock record (Frazer et al., 2014; Lundstrom and Glazner, 2016). A precise temporal agreement of volcanism with the D-C boundary is likely to be conjectural for some time, because correlation between the events is still inexact and radiometric dates of igneous candidates are still being constrained (Filipiak and Racki, 2010; Percival et al., 2018). However, the presence of volcanic ash/tuff deposits in Spain and Portugal (Gonzalez et al., 2006), South China (Liu et al., 2012), Poland (Filipiak and Racki, 2010; Marynowski et al., 2012) and Ireland (Pracht and Batchelor, 1998) together suggest that both local and potentially large-scale volcanic activity were occurring at the D-C boundary. In particular, the presence of catastrophic volcanism at the D-C boundary is supported by palynological observations that compared miospores from the crisis interval to miospores from the Holocene that were known to have been affected by volcanism or analogous anthropogenic SO_2 and chloride/fluoride pollution (Filipiak and Racki, 2010). Coeval ash/tuff deposits with geochemical/lithological evidence for wildfires in Hangenberg Crisis sediments in Poland (Marynowski et al., 2012) and Spain (Menor-Salván et al., 2010) provide additional indirect evidence for intense volcanic activity at the D-C boundary. Bulk Hg concentrations on their own probably do not provide enough information to fingerprint a point source for the Hg, but these anomalies do suggest that massive volcanism may have been a factor in the Hangenberg Crisis and end-Devonian biodiversity crisis. To further confirm this global widespread volcanism hypothesis, terrestrial sediments from the D-C transition need to be analyzed, which would be independent of ocean redox conditions and marine Hg cycling (Percival et al., 2017).

Acknowledgements

O. Paschall received funding from Appalachian State University, the American Association of Petroleum Geologists and the Geological Society of America. S. Carmichael received funding from National Geographic (CP-113R-17). Deutsche Forschungsgemeinschaft (DFG) provided financial support (DFG KO-1622/15-1) to P. Königshof. Phuong H. Ta has received funding from the National Foundation for Science & Technology (NAFOSTED project No. 105.03 – 2016.19). A. Dombrowski received funding from Appalachian State University. This paper is a contribution to IGCP Project 596 (Climate Change and Biodiversity Patterns in the Mid-Paleozoic). We are grateful to Michael Joachimski for providing carbon isotope data, and Drew Coleman and Cameron Batchelor for providing $^{87}Sr/^{86}Sr$ data, and K. Krommes for providing XRD data. We thank our reviewers for constructive feedback that has greatly improved our manuscript.

References

Algeo, T.J., 2004. Can marine anoxic events draw down the trace element inventory of seawater? Geology, 32(12), 1057-1060.

Algeo, T.J., Berner, R.A., Maynard, J.B. and Scheckler, S.E., 1995. Late Devonian oceanic anoxic events and biotic crises:“rooted” in the evolution of vascular land plants. GSA today, 5(3), 63-66.

Algeo, T.J. and Lyons, T.W., 2006. Mo–total organic carbon covariation in modern anoxic marine environments: Implications for analysis of paleoredox and paleohydrographic conditions. Paleoceanography, 21(1).

Algeo, T.J., Lyons, T.W., Blakey, R.C. and Over, D.J., 2007. Hydrographic conditions of the Devono–Carboniferous North American Seaway inferred from sedimentary Mo–TOC relationships. Palaeogeography, Palaeoclimatology, Palaeoecology, 256(3), 204-230.

Algeo, T.J. and Maynard, J.B., 2004. Trace-element behavior and redox facies in core shales of Upper Pennsylvanian Kansas-type cyclothems. Chemical Geology, 206(3–4), 289-318.

Algeo, T.J. and Maynard, J.B., 2008. Trace-metal covariation as a guide to water-mass conditions in ancient anoxic marine environments. Geosphere, 4(5), 872-887.

Algeo, T.J. and Scheckler, S.E., 1998. Terrestrial-marine teleconnections in the Devonian: links between the evolution of land plants, weathering processes, and marine anoxic events. Philosophical Transactions of the Royal Society of London. Series B: Biological Sciences, 353(1365), 113-130.

Almond, J., Marshall, J. and Evans, F., 2002. Latest Devonian and earliest Carboniferous glacial events in South Africa, 16th International Sedimentological Congress. International Association of Sedimentologists, Rands Afrikaans University, Johannesburg, pp. 12.

Aretz, M., 2013. Report on the workshop of the task group for defining the Devonian-Carboniferous boundary. In: M. Aretz, B. Richards, P. Kabanov and S. Nikolaeva (Eds.). Newsletter on Carboniferous Stratigraphy. International Union of Geological Sciences, Subcommission on Carboniferous Stratigraphy, pp. 31-35.

Averbuch, O. et al., 2005. Mountain building-enhanced continental weathering and organic carbon burial as major causes for climatic cooling at the Frasnian–Famennian boundary (c. 376 Ma)? Terra Nova, 17(1), 25-34.

Bábek, O., Kumpan, T., Kalvoda, J. and Grygar, T.M., 2016. Devonian/Carboniferous boundary glacioeustatic fluctuations in a platform-to-basin direction: a geochemical

approach of sequence stratigraphy in pelagic settings. Sedimentary geology, 337, 81-99.

Bai, S.-L., 2001. Ni-Ir Anomaly, Microtektites, and the Biotic Crisis across the Devonian–Carboniferous Boundary, Southern China. International Geology Review, 43(3), 265-275.

Bai, S.-l., Bai, Z.Q., Ma, X.P., Wang, D.R. and Sun, Y.L., 1994. Devonian Events and Biostratigraphy of South China. Peking University Press, Beijing, China.

Becker, R.T., Kaiser, S.I. and Aretz, M., 2016. Review of chrono-, litho-and biostratigraphy across the global Hangenberg Crisis and Devonian–Carboniferous Boundary. Geological Society, London, Special Publications, 423(1), 355-386.

Beier, J.A. and Hayes, J.M., 1989. Geochemical and isotopic evidence for paleoredox conditions during deposition of the Devonian-Mississippian New Albany Shale, southern Indiana. Geological Society of America Bulletin, 101(6), 774-782.

Bergquist, B.A., 2017. Mercury, volcanism, and mass extinctions. Proceedings of the National Academy of Sciences, 114(33), 8675–8677.

Bhatia, M.R. and Crook, K.A.W., 1986. Trace element characteristics of graywackes and tectonic setting discrimination of sedimentary basins. Contributions to Mineralogy and Petrology, 92(2), 181-193. English

Blakey, R., 2016. Devonian - 380 Ma, Global Paleogeography and Tectonics in Deep Time Series. Deep Time Maps™ Paleogeography.

Bond, D., Wignall, P.B. and Racki, G., 2004. Extent and duration of marine anoxia during the Frasnian–Famennian (Late Devonian) mass extinction in Poland, Germany, Austria and France. Geological Magazine, 141(02), 173-193.

Bond, D.P. and Wignall, P.B., 2014. Large igneous provinces and mass extinctions: An update. Geological Society of America Special Papers, 505, SPE505-02.

Brand, U., Legrand-Blain, M. and Streel, M., 2004. Biochemostratigraphy of the Devonian−Carboniferous boundary global stratotype section and point, Griotte Formation, La Serre, Montagne Noire, France. Palaeogeography, Palaeoclimatology, Palaeoecology, 205(3–4), 337-357.

Brezinski, D.K., Cecil, C.B. and Skema, V.W., 2010. Late Devonian glacigenic and associated facies from the central Appalachian Basin, eastern United States. Geological Society of America Bulletin, 122(1-2), 265-281.

Brezinski, D.K., Cecil, C.B., Skema, V.W. and Kertis, C.A., 2009. Evidence for long-term climate change in Upper Devonian strata of the central Appalachians. Palaeogeography, Palaeoclimatology, Palaeoecology, 284(3), 315-325.

Brumsack, H.-J., 2006. The trace metal content of recent organic carbon-rich sediments: implications for Cretaceous black shale formation. Palaeogeography, Palaeoclimatology, Palaeoecology, 232(2), 344-361.

Buggisch, W. and Joachimski, M.M., 2006. Carbon isotope stratigraphy of the Devonian of Central and Southern Europe. Palaeogeography, Palaeoclimatology, Palaeoecology, 240(1), 68-88.

Calvert, S. and Pedersen, T., 1992. Organic carbon accumulation and preservation in marine sediments: How important is anoxia. Organic matter: productivity, accumulation, and preservation in recent and ancient sediments, 533, 231-263.

Caplan, M.L. and Bustin, R.M., 1998. Palaeoceanographic controls on geochemical characteristics of organic-rich Exshaw mudrocks: role of enhanced primary production. Organic Geochemistry, 30(2–3), 161-188.

Caplan, M.L. and Bustin, R.M., 1999. Devonian–Carboniferous Hangenberg mass extinction event, widespread organic-rich mudrock and anoxia: causes and consequences. Palaeogeography, Palaeoclimatology, Palaeoecology, 148(4), 187-207.

Caplan, M.L. and Bustin, R.M., 2001. Palaeoenvironmental and palaeoceanographic controls on black, laminated mudrock deposition: example from Devonian–Carboniferous strata, Alberta, Canada. Sedimentary Geology, 145(1–2), 45-72.

Caplan, M.L., Bustin, R.M. and Grimm, K.A., 1996. Demise of a Devonian-Carboniferous carbonate ramp by eutrophication. Geology, 24(8), 715-718.

Caputo, M.V., de Melo, J.G., Streel, M., Isbell, J.L. and Fielding, C., 2008. Late Devonian and early Carboniferous glacial records of South America. Geological Society of America Special Papers, 441, 161-173.

Carmichael, S.K., Waters, J., Königshof, P., Suttner, T.J. and Kido, E., in review (this volume). Looking for the Kellwasser Event in all the "wrong" places: how does paleogeographic and paleoenvironmental bias limit our knowledge? submitted to Global and Planetary Change, TBA.

Carmichael, S.K. and Waters, J.A., 2015. A decade of deciphering the Late Devonian: more answers, but many more questions. In: B. Mottequin, J. Denayer, P. Koenigshof, C. Prestianni and S. Olive (Eds.), IGCP596-SDS Symposium. STRATA. Association STRATA, Brussels, Belgium, pp. 27-29.

Carmichael, S.K. et al., 2016. Climate instability and tipping points in the Late Devonian: Detection of the Hangenberg Event in an open oceanic island arc in the Central Asian Orogenic Belt. Gondwana Research, 32, 213-231.

Charbonnier, G. and Föllmi, K.B., 2017. Mercury enrichments in lower Aptian sediments support the link between Ontong Java large igneous province activity and oceanic anoxic episode 1a. Geology, 45(1), 63-66.

Charbonnier, G. et al., 2017. Mercury enrichment indicates volcanic triggering of Valanginian environmental change. Scientific Reports 7.

Chen, D., Qing, H., Yan, X. and Li, H., 2006. Hydrothermal venting and basin evolution (Devonian, South China): Constraints from rare earth element geochemistry of chert. Sedimentary Geology, 183(3-4), 203-216.

Cole, D., Myrow, P.M., Fike, D.A., Hakim, A. and Gehrels, G.E., 2015. Uppermost Devonian (Famennian) to Lower Mississippian events of the western U.S.: Stratigraphy, sedimentology, chemostratigraphy, and detrital zircon geochronology. Palaeogeography, Palaeoclimatology, Palaeoecology, 427, 1-19.

Copper, P., 1986. Frasnian/Famennian mass extinction and cold-water oceans. Geology, 14(10), 835-839.

Corradini, C., Spalletta, C., Mossoni, A., Matyja, H. and Over, D.J., 2017. Conodonts across the Devonian/Carboniferous boundary: a review and implication for the redefinition of the boundary and a proposal for an updated conodont zonation. Geological Magazine, 154(4), 888-902.

Courtillot, V., Kravchinsky, V.A., Quidelleur, X., Renne, P.R. and Gladkochub, D.P., 2010. Preliminary dating of the Viluy traps (Eastern Siberia): Eruption at the time of Late Devonian extinction events? Earth and Planetary Science Letters, 300(3), 239-245.

Cramer, B., Saltzman, M., Day, J.E. and Witzke, B.J., 2008. Record of the Late Devonian Hangenberg global positive carbon-isotope excursion in an epeiric sea setting: carbonate production, organic-carbon burial and paleoceanography during the Late Famennian. Dynamics of Epeiric Seas, Geological Association of Canada Special Paper, 48, 103-118.

De Vleeschouwer, D., Crucifix, M., Bounceur, N. and Claeys, P., 2014. The impact of astronomical forcing on the Late Devonian greenhouse climate. Global and Planetary Change, 120, 65-80.

De Vleeschouwer, D. et al., 2017. Timing and pacing of the Late Devonian mass extinction event regulated by eccentricity and obliquity. Nature communications, 8(1).

De Vleeschouwer, D., Königshof, P. and Claeys, P., 2018. Reading time and paleoenvironmental change in the Emsian–Eifelian boundary GSSP section (Wetteldorf, Germany): A combination of cyclostratigraphy and facies analysis. Newsletters on Stratigraphy, 51(2), 209-226.

Dessureau, G., Piper, D.J.W. and Pe-Piper, G., 2000. Geochemical evolution of earliest Carboniferous continental tholeiitic basalts along a crustal-scale shear zone, southwestern Maritimes basin, eastern Canada1Geological Survey of Canada contribution, 1999035.1. Lithos, 50(1), 27-50.

Doan, T.N. and Tong-Dzuy, T., 2006. Upper Paleozoic. In: T. Tong-Dzuy and V. Khuc (Eds.), Stratigraphic Units of Vietnam. Vietnam National University Publishing House, Hanoi, Vietnam, pp. 201-244.

Dymond, J., Suess, E. and Lyle, M., 1992. Barium in deep-sea sediment: A geochemical proxy for paleoproductivity. Paleoceanography, 7(2), 163-181.

Ernst, W., 1970. Geochemical facies analysis, 11. Elsevier, 152 pp.

Filipiak, P. and Racki, G., 2010. Proliferation of abnormal palynoflora during the end-Devonian biotic crisis. Geological Quarterly, 54(1), 1–14.

Flajs, G. and Feist, R., 1988. Index conodonts, trilobites and environment of the Devonian-Carboniferous boundary beds at La Serre (Montagne Noire, France). Courier Forschungsinstitut Senckenberg, 100, 53-107.

Font, E. et al., 2016. Mercury anomaly, Deccan volcanism, and the end-Cretaceous mass extinction. Geology, 44(2), 171-174.

Formolo, M.J., Riedinger, N. and Gill, B.C., 2014. Geochemical evidence for euxinia during the Late Devonian extinction events in the Michigan Basin (USA). Palaeogeography, Palaeoclimatology, Palaeoecology, 414, 146-154.

Frazer, R.E., Coleman, D.S. and Mills, R.D., 2014. Zircon U-Pb geochronology of the Mount Givens Granodiorite: Implications for the genesis of large volumes of eruptible magma. Journal of Geophysical Research: Solid Earth, 119(4), 2907-2924.

Gonzalez, F., Moreno, C. and Santos, A., 2006. The massive sulphide event in the Iberian Pyrite Belt: confirmatory evidence from the Sotiel-Coronada Mine. Geological Magazine, 143(6), 821-827.

Grasby, S.E., Beauchamp, B., Bond, D.P., Wignall, P.B. and Sanei, H., 2016. Mercury anomalies associated with three extinction events (Capitanian crisis, latest Permian extinction and the Smithian/Spathian extinction) in NW Pangea. Geological magazine, 153(2), 285-297.

Grasby, S.E. et al., 2017. Isotopic signatures of mercury contamination in latest Permian oceans. Geology, 45(1), 55-58.

Halpin, J.A. et al., 2016. U–Pb zircon geochronology and geochemistry from NE Vietnam: A 'tectonically disputed'territory between the Indochina and South China blocks. Gondwana Research, 34, 254-273.

Hammer, Ø., Harper, D. and Ryan, P., 2001. PAST: Paleontological Statistics Software Package for Education and Data Analysis, Palaeontologia Electronica, pp. 2009.

Hatch, J. and Leventhal, J., 1992. Relationship between inferred redox potential of the depositional environment and geochemistry of the Upper Pennsylvanian (Missourian) Stark Shale Member of the Dennis Limestone, Wabaunsee County, Kansas, USA. Chemical Geology, 99(1-3), 65-82.

Hoffman, D. et al., 1998. Regional and stratigraphic variation in bottomwater anoxia in offshore core shales of Upper Pennsylvanian cyclothems from the Eastern Midcontinent Shelf (Kansas), USA. In: J. Schieber, W. Zimmerle and P.S. Sethi (Eds.), Shales and Mudstones. Schweizerbartische Verlagsbuchhandlung, Stuttgart, Germany, 1, pp. 243-269.

Huang, H. et al., 2013. Depositional chemistry of chert during late Paleozoic from western Guangxi and its implication for the tectonic evolution of the Youjiang Basin. Science China Earth Sciences, 56(3), 479-493.

Isaacson, P. et al., 2008. Late Devonian–earliest Mississippian glaciation in Gondwanaland and its biogeographic consequences. Palaeogeography, Palaeoclimatology, Palaeoecology, 268(3), 126-142.

Isaacson, P., Hladil, J., Shen, J., Kalvoda, J. and Grader, G., 1999. Late Devonian (Famennian) glaciation in South America and marine offlap on other continents. Abhandlungen-Geologischen Bundesanstalt, 54, 239-258.

Jones, B. and Manning, D.A., 1994. Comparison of geochemical indices used for the interpretation of palaeoredox conditions in ancient mudstones. Chemical Geology, 111(1), 111-129.

Kaiser, S.I., 2009. The Devonian/Carboniferous boundary stratotype section (La Serre, France) revisited. Newsletters on Stratigraphy, 43(2), 195-205.

Kaiser, S.I., Aretz, M. and Becker, R.T., 2016. The global Hangenberg Crisis (Devonian–Carboniferous transition): review of a first-order mass extinction. Geological Society, London, Special Publications, 423, 387–437.

Kaiser, S.I. and Corradini, C., 2011. The early siphonodellids (Conodonta, Late Devonian-Early Carboniferous): overview and taxonomic state. Neues Jahrbuch für Geologie und Paläontologie-Abhandlungen, 261(1), 19-35.

Kaiser, S.I., Steuber, T. and Becker, R.T., 2008. Environmental change during the Late Famennian and Early Tournaisian (Late Devonian–Early Carboniferous): implications from stable isotopes and conodont biofacies in southern Europe. Geological Journal, 43(2-3), 241-260.

Kaiser, S.I., Steuber, T., Becker, R.T. and Joachimski, M.M., 2006. Geochemical evidence for major environmental change at the Devonian–Carboniferous boundary in the Carnic Alps and the Rhenish Massif. Palaeogeography, Palaeoclimatology, Palaeoecology, 240(1–2), 146-160.

Kalvoda, J. et al., 2018. Fine-scale LA-ICP-MS study of redox oscillations and REEY cycling during the latest Devonian Hangenberg Crisis (Moravian Karst, Czech Republic). Palaeogeography, Palaeoclimatology, Palaeoecology, 493, 30-43.

Komatsu, T. et al., 2014. Devonian–Carboniferous transition containing a Hangenberg Black Shale equivalent in the Pho Han Formation on Cat Ba Island, northeastern Vietnam. Palaeogeography, Palaeoclimatology, Palaeoecology, 404, 30-43.

Komatsu, T. et al., 2012a. Devonian–Carboniferous transition in the Pho Han Formation on Cat Ba Island, northeastern Vietnam. The Journal of the Geological Society of Japan, 118(6), V-VI.

Komatsu, T. et al., 2012b. Devonian to Carboniferous transitional beds on Cat Ba Island, northeastern Vietnam - a preliminary assessment. Acta Geoscientica Sinica, 33(Supplement 1), 38.

Kravchinsky, V.A., 2012. Paleozoic large igneous provinces of Northern Eurasia: Correlation with mass extinction events. Global and Planetary Change, 86, 31-36.

Kumpan, T., Bábek, O., Kalvoda, J., Frýda, J. and Matys Grygar, T., 2014a. A high-resolution, multiproxy stratigraphic analysis of the Devonian–Carboniferous boundary sections in the Moravian Karst (Czech Republic) and a correlation with the Carnic Alps (Austria). Geological Magazine, 151(02), 201-215.

Kumpan, T. et al., 2015. Petrophysical and geochemical signature of the Hangenberg Events: an integrated stratigraphy of the Devonian-Carboniferous boundary interval in the Northern Rhenish Massif (Avalonia, Germany). Bulletin of Geosciences, 90(3), 667-694.

Kumpan, T., Bábek, O., Kalvoda, J., Matys Grygar, T. and Frýda, J., 2014b. Sea-Level and Environmental Changes Around the Devonian–Carboniferous Boundary in the Namur–Dinant Basin (S Belgium, NE France): A Multi-proxy Stratigraphic Analysis of Carbonate Ramp Archives and its Use in Regional and Interregional Correlations. Sedimentary Geology, 311, 43-59.

Kumpan, T., Kalvoda, J., Bábek, O., Holá, M. and Kanický, V., 2019. Tracing paleoredox conditions across the Devonian–Carboniferous boundary event: A case study from carbonate-dominated settings of Belgium, the Czech Republic, and northern France. Sedimentary Geology, 380, 143-157.

Kürschner, W., Becker, R.T., Buhl, D. and Veizer, J., 1993. Strontium isotopes in conodonts: Devonian-Carboniferous transition, the northern Rhenish Slate Mountains, Germany. Annales de la Société géologique de Belgique, 115(2), 595-622.

Lai, C.-K. et al., 2014. The Western Ailaoshan Volcanic Belts and their SE Asia connection: A new tectonic model for the Eastern Indochina Block. Gondwana Research, 26(1), 52-74.

Lakin, J., Marshall, J., Troth, I. and Harding, I., 2016. Greenhouse to icehouse: a biostratigraphic review of latest Devonian–Mississippian glaciations and their global effects. Geological Society, London, Special Publications, 423, SP423. 12.

Liu, J. et al., 2016. Changes in marine nitrogen fixation and denitrification rates during the end-Devonian mass extinction. Palaeogeography, Palaeoclimatology, Palaeoecology, 448, 195-206.

Liu, Y.-Q. et al., 2012. U–Pb zircon age, sedimentary facies, and sequence stratigraphy of the Devonian–Carboniferous boundary, Daposhang Section, Guizhou, China. Palaeoworld, 21(2), 100-107.

Lundstrom, C.C. and Glazner, A.F., 2016. Silicic magmatism and the volcanic–plutonic connection. Elements, 12(2), 91-96.

Lyons, T.W., Werne, J.P., Hollander, D.J. and Murray, R., 2003. Contrasting sulfur geochemistry and Fe/Al and Mo/Al ratios across the last oxic-to-anoxic transition in the Cariaco Basin, Venezuela. Chemical Geology, 195(1), 131-157.

Marshall, J., Astin, T., Evans, F. and Almond, J., 2002. The palaeoclimatic significance of the Devonian-Carboniferous boundary. Palaeontology Newsletter, 51, 103.

Martinez, A.M., Boyer, D.L., Droser, M.L., Barrie, C. and Love, G.D., 2018. A stable and productive marine microbial community was sustained through the end-Devonian Hangenberg Crisis within the Cleveland Shale of the Appalachian Basin, United States. Geobiology, 10.1111/gbi.12314, 1-16.

Marynowski, L. and Filipiak, P., 2007. Water column euxinia and wildfire evidence during deposition of the Upper Famennian Hangenberg event horizon from the Holy Cross

Mountains (central Poland). Geological Magazine, 144(3), 569-595.

Marynowski, L. et al., 2012. Deciphering the upper Famennian Hangenberg Black Shale depositional environments based on multi-proxy record. Palaeogeography, Palaeoclimatology, Palaeoecology, 346, 66-86.

Matyja, H., Sobie, K. and Marynowski, L., 2015. The expression of the Hangenberg Event (latest Devonian) in a relatively shallow-marine succession (Pomeranian Basin, Poland): the results of a multi-proxy investigation. Geological Magazine, 10.1017/S001675681400034X, 1-29.

McArthur, J., Howarth, R. and Shields, G., 2012. Strontium Isotope Stratigraphy. The Geologic Time Scale, 1, 127-144.

McGhee, G.R., 2001. Extinction: Late Devonian Mass Extinction, eLS. John Wiley & Sons, Ltd, 10.1002/9780470015902.a0001653.pub3.

McGhee, G.R., 2005. Modelling Late Devonian extinction hypotheses. In: D.J. Over, J.R. Morrow and P.B. Wignall (Eds.), Developments in Palaeontology and Stratigraphy. Elsevier, 20, pp. 37-50.

McGhee, G.R., Clapham, M.E., Sheehan, P.M., Bottjer, D.J. and Droser, M.L., 2013. A new ecological-severity ranking of major Phanerozoic biodiversity crises. Palaeogeography, Palaeoclimatology, Palaeoecology, 370(0), 260-270.

McKay, J. and Pedersen, T., 2008. The accumulation of silver in marine sediments: A link to biogenic Ba and marine productivity. Global Biogeochemical Cycles, 22(4).

McManus, J., Berelson, W.M., Klinkhammer, G.P., Hammond, D.E. and Holm, C., 2005. Authigenic uranium: Relationship to oxygen penetration depth and organic carbon rain. Geochimica et Cosmochimica Acta, 69(1), 95-108.

Melo, J., Loboziak, S. and Streel, M., 1999. Latest Devonian to Early Carboniferous biostratigraphy of Northern Brazil: an update. Bulletin du Centre de Recherches Elf Exploration Production, 22(1), 13-33.

Menor-Salván, C., Tornos, F., Fernández-Remolar, D. and Amils, R., 2010. Association between catastrophic paleovegetation changes during Devonian–Carboniferous boundary and the formation of giant massive sulfide deposits. Earth and Planetary Science Letters, 299(3-4), 398-408.

Metcalfe, I., 2009. Late Palaeozoic and Mesozoic tectonic and palaeogeographical evolution of SE Asia. Geological Society, London, Special Publications, 315(1), 7-23.

Middelburg, J. and Levin, L., 2009. Coastal hypoxia and sediment biogeochemistry. Biogeosciences Discussions, 6(2), 3655-3706.

Moreno, C., González, F., Sáez, R., Melgarejo, J.C. and Suárez-Ruiz, I., 2018. The Upper Devonian Kellwasser event recorded in a regressive sequence from inner shelf to lagoonal pond, Catalan Coastal Ranges, Spain. Sedimentology.

Moreno, C., Sierra, S. and Sáez, R., 1996. Evidence for catastrophism at the Famennian-Dinantian boundary in the Iberian Pyrite Belt. Geological Society, London, Special Publications, 107(1), 153-162.

Murphy, J.B., van Staal, C.R. and Keppie, J.D., 1999. Middle to late Paleozoic Acadian orogeny in the northern Appalachians: A Laramide-style plume-modified orogeny? Geology, 27(7), 653-656.

Murray, R. and Leinen, M., 1996. Scavenged excess aluminum and its relationship to bulk titanium in biogenic sediment from the central equatorial Pacific Ocean. Geochimica et Cosmochimica Acta, 60(20), 3869-3878.

Myrow, P.M. et al., 2014. High-precision U–Pb age and duration of the latest Devonian (Famennian) Hangenberg event, and its implications. Terra Nova, 26(3), 222-229.

Osanai, Y. et al., 2004. Permo-Triassic ultrahigh-temperature metamorphism in the Kontum massif, central Vietnam. Journal of Mineralogical and Petrological Sciences, 99(4), 225-241.

Outridge, P., Sanei, H., Stern, G., Hamilton, P. and Goodarzi, F., 2007. Evidence for control of mercury accumulation rates in Canadian High Arctic lake sediments by variations of aquatic primary productivity. Environmental science & technology, 41(15), 5259-5265.

Paproth, E., Feist, R. and Flajs, G., 1991. Decision on the Devonian-Carboniferous boundary stratotype. Episodes, 14(4), 331-336.

Percival, L. et al., 2018. Precisely dating the Frasnian–Famennian boundary: implications for the cause of the Late Devonian mass extinction. Scientific Reports, 8(1), 9578.

Percival, L. et al., 2015. Globally enhanced mercury deposition during the end-Pliensbachian extinction and Toarcian OAE: A link to the Karoo–Ferrar Large Igneous Province. Earth and Planetary Science Letters, 428, 267-280.

Percival, L.M.E. et al., 2017. Mercury evidence for pulsed volcanism during the end-Triassic mass extinction. Proceedings of the National Academy of Sciences of the United States of America, 114(30), 7929-7934.

Perkins, R.B., Piper, D.Z. and Mason, C.E., 2008. Trace-element budgets in the Ohio/Sunbury shales of Kentucky: Constraints on ocean circulation and primary productivity in the Devonian–Mississippian Appalachian Basin. Palaeogeography, Palaeoclimatology, Palaeoecology, 265(1–2), 14-29.

Piper, D.Z. and Calvert, S.E., 2009. A marine biogeochemical perspective on black shale deposition. Earth-Science Reviews, 95(1–2), 63-96.

Playford, P.E., McLaren, D.J., Orth, C.J., Gilmore, J.S. and Goodfellow, W.D., 1984. Iridium anomaly in the Upper Devonian of the Canning Basin, western Australia. Science, 226(4673), 437-439.

Pomar, L. and Hallock, P., 2008. Carbonate factories: a conundrum in sedimentary geology. Earth-Science Reviews, 87(3-4), 134-169.

Pracht, M. and Batchelor, R., 1998. A geochemical study of late Devonian and early Carboniferous tuffs from the South Munster Basin, Ireland. Irish Journal of Earth Sciences, 25-38.

Prestianni, C., Sautois, M. and Denayer, J., 2016. Disrupted continental environments around the Devonian-Carboniferous Boundary: introduction of the tener event. Geologica Belgica.

Pujol, F., Berner, Z. and Stüben, D., 2006. Palaeoenvironmental changes at the Frasnian/Famennian boundary in key European sections: Chemostratigraphic constraints. Palaeogeography, Palaeoclimatology, Palaeoecology, 240(1), 120-145.

Qie, W. et al., 2015. Local overprints on the global carbonate δ13C signal in Devonian–Carboniferous boundary successions of South China. Palaeogeography, Palaeoclimatology, Palaeoecology, 418(0), 290-303.

Racki, G., 2005. Toward understanding Late Devonian global events: few answers, many questions. In: D.J. Over, J.R. Morrow and P.B. Wignall (Eds.), Understanding Late Devonian and Permian-Triassic Biotic and Climatic Events: Towards an Integrated Approach, 20, pp. 5-36.

Racki, G., 2012. The Alvarez impact theory of mass extinction; limits to its applicability and the "Great Expectations Syndrome". Acta Palaeontologica Polonica, 57(4), 681-702.

Racki, G., Racka, M., Matyja, H. and Devleeschouwer, X., 2002. The Frasnian/Famennian boundary interval in the South Polish–Moravian shelf basins: integrated event-stratigraphical approach. Palaeogeography, Palaeoclimatology, Palaeoecology, 181(1), 251-297.

Racki, G., Rakociński, M. and Marynowski, L., 2018a. Anomalous Upper Devonian mercury enrichments: comparison of Inductively Coupled Plasma–Mass Spectrometry (ICP-MS) and AAS analytical data. Geological Quarterly, 62(3), 487-495, doi: 10.7306/gq. 1419.

Racki, G., Rakociński, M., Marynowski, L. and Wignall, P.B., 2018b. Mercury enrichments and the Frasnian-Famennian biotic crisis: A volcanic trigger proved? Geology, 46(6), 543-546.

Reimers, R.S. and Krenkel, P.A., 1974. Kinetics of mercury adsorption and desorption in sediments. Journal (Water Pollution Control Federation), 352-365.

Riding, R., 2009. An atmospheric stimulus for cyanobacterial-bioinduced calcification ca. 350 million years ago? Palaios, 24(10), 685-696.

Rimmer, S.M., 2004. Geochemical paleoredox indicators in Devonian–Mississippian black shales, Central Appalachian Basin (USA). Chemical Geology, 206(3–4), 373-391.

Rodionov, N. et al., 2018. U-Pb SHRIMP-II ages of titanite and timing constraints on apatite-nepheline mineralization in the Khibiny and Lovozero alkaline massifs (Kola Peninsula). Russian Geology and Geophysics, 59(8), 962-974.

Rowan, C.J., Roberts, A.P. and Broadbent, T., 2009. Reductive diagenesis, magnetite dissolution, greigite growth and paleomagnetic smoothing in marine sediments: A new view. Earth and Planetary Science Letters, 277(1), 223-235.

Sandberg, C.A., Morrow, J.R. and Ziegler, W., 2002. Late Devonian sea-level changes, catastrophic events, and mass extinctions. Geological Society of America Special Papers, 356, 473-487.

Sandberg, C.A. and Ziegler, W., 1996. Devonian conodont biochronology in geologic time calibration. Senckenbergiana lethaea, 76(1-2), 259-265.

Sandberg, C.A., Ziegler, W., Leuteritz, K. and Brill, S.M., 1978. Phylogeny, speciation, and zonation of Siphonodella (Conodonta, upper Devonian and lower Carboniferous). Newsletters on Stratigraphy, 102-120.

Schieber, J., Krinsley, D. and Riciputi, L., 2000. Diagenetic origin of quartz silt in mudstones and implications for silica cycling. Nature, 406(6799), 981-985.

Schlager, W., 2003. Benthic carbonate factories of the Phanerozoic. International Journal of Earth Sciences, 92(4), 445-464.

Schmitz, B., Charisi, S.D., Thompson, E.I. and Speijer, R.P., 1997. Barium, SiO2 (excess), and P2O5 as proxies of biological productivity in the Middle East during the Palaeocene and the latest Palaeocene benthic extinction event. Terra Nova, 9(2), 95-99.

Sepkoski, J.J., 1996. Patterns of Phanerozoic extinction: a perspective from global data bases. In: O.H. Walliser (Ed.), Global events and event stratigraphy in the Phanerozoic. Springer-Verlag, Berlin, Berlin, pp. 35-51.

Sial, A. et al., 2013. Mercury as a proxy for volcanic activity during extreme environmental turnover: The Cretaceous–Paleogene transition. Palaeogeography, Palaeoclimatology, Palaeoecology, 387, 153-164.

Smit, J., Koeberl, C., Claeys, P. and Montanari, A., 2016. Mercury anomaly, Deccan volcanism, and the end-Cretaceous mass extinction: Comment. Geology, 44(3), e381-e381.

Smith, M.G. and Bustin, R.M., 1998. Production and preservation of organic matter during deposition of the Bakken Formation (Late Devonian and Early Mississippian), Williston Basin. Palaeogeography, Palaeoclimatology, Palaeoecology, 142(3–4), 185-200.

Spalletta, C., Perri, M.C., Over, D.J. and Corradini, C., 2017. Famennian (Upper Devonian) conodont zonation: revised global standard. Bulletin of Geosciences, 92(1), 31-57.

Streel, M., Caputo, M.V., Loboziak, S., Melo, J. and Thorez, J., 2001. Palynology and sedimentology of laminites and tillites from the latest Famennian of the Parnaíba Basin, Brazil. Geologica Belgica, 3(1-2), 87-96.

Streel, M., Caputo, M.V., Loboziak, S. and Melo, J.H.G., 2000. Late Frasnian–Famennian climates based on palynomorph analyses and the question of the Late Devonian glaciations. Earth-Science Reviews, 52(1), 121-173.

Suzuki, N., Ishida, K., Shinomiya, Y. and Ishiga, H., 1998. High productivity in the earliest Triassic ocean: black shales, Southwest Japan. Palaeogeography, Palaeoclimatology, Palaeoecology, 141(1-2), 53-65.

Ta Hoa, P. and Doan, T.N., 2005. Preliminary studies on the Devonian–Carboniferous boundary at the Nam Cat Ba section, Hai Phong Province. Journal Science Vietnam National University, 21, 38-47. (in Vietnamese with English abstract)

Ta Hoa, P. and Doan, T.N., 2007. Discussion on the Devonian/ Carboniferous boundary at the south of Cat Ba Island. Journal Geological Series A, 298, 12-17. (in Vietnamese with English abstract)

Them, T.R. et al., 2019. Terrestrial sources as the primary delivery mechanism of mercury to the oceans across the Toarcian Oceanic Anoxic Event (Early Jurassic). Earth and Planetary Science Letters, 507, 62-72.

Thibodeau, A.M. and Bergquist, B.A., 2017. Do mercury isotopes record the signature of massive volcanism in marine sedimentary records? Geology, 45(1), 95-96.

Thibodeau, A.M. et al., 2016. Mercury anomalies and the timing of biotic recovery following the end-Triassic mass extinction. Nature communications, 7, 11147.

Tomshin, M., Kopylova, A., Konstantinov, K. and Gogoleva, S., 2018. Basites of the Vilyui paleorift: geochemistry and sequence of intrusive events. Russian Geology and Geophysics, 59(10), 1204-1216.

Tribovillard, N., Algeo, T.J., Lyons, T. and Riboulleau, A., 2006. Trace metals as paleoredox and paleoproductivity proxies: An update. Chemical Geology, 232(1–2), 12-32.

Tribovillard, N. et al., 2015. Iron availability as a dominant control on the primary composition and diagenetic overprint of organic-matter-rich rocks. Chemical Geology, 401, 67-82.

Van der Weijden, C.H., 2002. Pitfalls of normalization of marine geochemical data using a common divisor. Marine Geology, 184(3-4), 167-187.

Ver Straeten, C.A., Brett, C.E. and Sageman, B.B., 2011. Mudrock sequence stratigraphy: A multi-proxy (sedimentological, paleobiological and geochemical) approach, Devonian Appalachian Basin. Palaeogeography, Palaeoclimatology, Palaeoecology, 304(1), 54-73.

Walliser, O.H., 1984. Pleading for a natural D/C boundary. Courier Forschungsinstitut Senckenberg, 67, 241-246.

Walliser, O.H., 1996. Global events in the Devonian and Carboniferous, Global events and event stratigraphy in the Phanerozoic. Springer, pp. 225-250.

Wang, K., Attrep , M. and Orth, C.J., 1993. Global iridium anomaly, mass extinction, and redox change at the Devonian-Carboniferous boundary. Geology, 21(12), 1071-1074.

Wang, K. et al., 1991. Geochemical evidence for a catastrophic biotic event at the Frasnian/Famennian boundary in south China. Geology, 19(8), 776-779.

Wang, P., Huang, Y., Wang, C., Feng, Z. and Huang, Q., 2013. Pyrite morphology in the first member of the Late Cretaceous Qingshankou Formation, Songliao Basin, Northeast China. Palaeogeography, Palaeoclimatology, Palaeoecology, 385, 125-136.

Wignall, P. and Newton, R., 1998. Pyrite framboid diameter as a measure of oxygen deficiency in ancient mudrocks. American Journal of Science, 298(7), 537-552.

Wignall, P.B. and Myers, K.J., 1988. Interpreting benthic oxygen levels in mudrocks: a new approach. Geology, 16(5), 452-455.

Wilkin, R. and Barnes, H., 1997. Formation processes of framboidal pyrite. Geochimica et Cosmochimica Acta, 61(2), 323-339.

Wilkin, R., Barnes, H. and Brantley, S., 1996. The size distribution of framboidal pyrite in modern sediments: An indicator of redox conditions. Geochimica et Cosmochimica Acta, 60(20), 3897-3912.

Wilkin, R.T., Arthur, M.A. and Dean, W.E., 1997. History of water-column anoxia in the Black Sea indicated by pyrite framboid size distributions. Earth and Planetary Science Letters, 148(3), 517-525.

Xiao, W., Huang, B., Han, C., Sun, S. and Li, J., 2010. A review of the western part of the Altaids: a key to understanding the architecture of accretionary orogens. Gondwana Research, 18(2), 253-273.

Xu, B., Gu, Z., Han, J. and Wang, C., 2008. Environmental changes during Frasnian-Famennian transition in south China: A multiproxy approach. Journal of Geophysical Research: Biogeosciences, 113(G4).

Yao, L., Aretz, M., Chen, J., Webb, G.E. and Wang, X., 2016. Global microbial carbonate proliferation after the end-Devonian mass extinction: Mainly controlled by demise of skeletal bioconstructors. Scientific reports, 6, 39694.

Yudina, A.B., Racki, G., Savage, N.M., Racka, M. and Malkowski, K., 2002. The Frasnian-Famennian events in a deep-shelf succession, Subpolar Urals: biotic, depositional, and geochemical records. Acta Palaeontologica Polonica, 47(2), 355–372.

Zeng, J., Xu, R. and Gong, Y., 2011. Hydrothermal activities and seawater acidification in the Late Devonian FF transition: Evidence from geochemistry of rare earth elements. Science China Earth Sciences, 54(4), 540.

Zhang, R.Y. et al., 2014. U-Pb dating and tectonic implication of ophiolite and metabasite from the Song Ma suture zone, northern Vietnam. American Journal of Science, 314(2), 649-678.

Zheng, L. et al., 2018. Mercury stable isotope compositions in magmatic-affected coal deposits: New insights to mercury sources, migration and enrichment. Chemical Geology, 479, 86-101.

Zhu, W. et al., 2018. Mercury transformations in resuspended contaminated sediment controlled by redox conditions, chemical speciation and sources of organic matter. Geochimica et Cosmochimica Acta, 220, 158-179.

Ziegler, W. and Sandberg, C.A., 1990. The Late Devonian standard conodont zonation. Courier Forschungsinstitut Senckenberg, 121, 1-115.

Ziegler, W. and Sandberg, C.A., 1994. Conodont phylogenetic-zone concept. Newsletters on Stratigraphy, 105-123.

Supplemental Information

Contents

Additional Methods

Framboid counting methodology

Two test samples (bed 110 and 121) were analyzed in order to determine an accurate yet efficient way to assess the size and distribution of pyrite framboids. Using the Features function in the Oxford Aztec EDS software, a 1 cm^2 area of each sample was scanned with 0% frame spacing at 500X magnification (2028 photos, continuous imaging with no spaces between them), and framboids were detected using a grayscale analysis of all features >2 μm in diameter with an aspect ratio of 0.90-1.10 (to filter for round framboid shapes vs. elongated structures representing non-framboidal pyrite minerals). Samples were analyzed again over the exact same area using a 100% frame spacing (520 photos, representing 0.26 cm^2 spread evenly over 1 cm^2 and spaced by the equivalent of a full photo, giving a staggered windowpane effect), under the same magnification and framboid detection conditions. The framboid count from the spaced images was multiplied by 4 to estimate the representative framboid number over a 1 cm^2 grid. The 100% spacing results in a 2 hour analysis time and 2-3 gigabites of data per sample vs. more than 8 hours and 7+ gigabites of data for each sample analyzed at 0% spacing.

The resulting framboid measurements were exported into Microsoft Excel for data analysis. The distribution of framboid sizes (length and equivalent circle diameter, or ECD) for 0 and 100% spacing were also analyzed to ensure that the distribution was not affected by framboids cut by the edges of each image. For both comparison samples, the resulting number of framboids counted using 0% spacing vs. 100% spacing were within 10% of each other.

Data presentation

Cross-plots with Al_2O_3

Only four samples (beds 116, 117, 120, and 121) have Al_2O_3 values >1 wt. %. When elemental data from these samples is plotted and correlated with Al_2O_3, these values are more heavily weighted when calculating R^2 values due to their larger leverage (greater distance from the mean Al_2O_3 value). For this reason, only values with Al_2O_3<1 were used when calculating R^2 values. As shown in Figure S1, all R^2 values are less than 0.3, indicating that proxies for all Pho Han samples analyzed (excluding 116, 117, 120, and 121) are not lithologically controlled. It is difficult to determine if geochemical proxies for beds 116, 117, 120, and 121 are lithologically controlled due to the small number of data points, and the potential for anomalous Al concentrations based on scavenging by organic matter (see *4.1.1*). As these beds were deposited during a period of known ecological crisis, the unusual conditions within the water column at that time can affect how the geochemical proxies are interpreted.

Despite the problems associated with normalizing to Al in carbonates with extremely low detrital components, we have presented the standard redox proxies normalized to Al and PAAS in Figure S2 and S3 for consistency with other datasets, following the methodology of Tribovillard et al. (2015). The particulate iron shuttle can impact Mo, P, As, and Sb enrichments when U enrichments are not present (Tribovillard et al., 2015). In Pho Han sediments, enrichments in U/Al and Mo/Al are present near the D-C boundary/Hangenberg Crisis, but As/Al and Sb/Al appear to be uncorrelated. Co/Al, V/Al, and Cr/Al are also uncorrelated to the D-C boundary or Hangenberg Crisis. Concurrent enrichments in U and Mo are linked to redox conditions, particulate shuttles, and the evolution of water chemistry (Algeo and Tribovillard, 2009). Mo/Al is enriched in beds 116-119 and U/Al is enriched in beds 117-119, indicating concurrent enrichments during the deposition of beds 117-119. Using Mo/Al and U/Al as redox proxies supports our interpretation that the most severe anoxia (Hangenberg Crisis) is within beds 116-118. Similar patterns are seen when normalizing against PAAS.

Trace-element crossplots

As seen in Riquier et al. (2007), we present crossplots of V/Cr vs. Ni/Co, V/(V+Ni) vs. Ni/Co, U/Th vs. Ni/Co, and U/Th vs. V/Cr in Figure S4. The beds that were deposited during the Hangenberg Crisis (116-118) generally lie within the dysoxic-anoxic fields. Although bed 117 falls into the oxic range of Ni/Co values, the U/Th data suggests that all beds (except 105) were

deposited under highly anoxic conditions. The use of Co and Cr as proxies in carbonate environments with low detrital input is problematic, however, and these are likely not appropriate proxies to use for analysis of this section (see *4.1.1*).

Hydrothermal supply

The South China Terrane experienced hydrothermal activity throughout the Late Devonian (Chen and Liao, 2006; Huang et al., 2013a; Huang et al., 2013b; Xu et al., 2008; Zeng et al., 2011). In order to assess whether deposition of Cat Co 3 section sediments was also affected by hydrothermal activity, REEN (normalized rare earth elements/lanthanides) distribution plots were made for beds for which we have complete rare earth element data (Figure S5). The REE data was normalized to PAAS values. Only bed 124 has an abnormal REEN spidergram pattern relative to all the others, but they all display negative Ce anomalies, which usually correspond to ocean basins that tend to be relatively depleted in Ce (Chen et al., 2006; Elderfield and Greaves, 1982; Tostevin et al., 2016). The REEN pattern is also not consistent with hydrothermal fluids, which usually contain anomalously high Eu values (as shown in Figure 1 of Tostevin et al., 2016).

Eu anomalies, Al/(Al+Fe+Mn), ΣREE, and $^{87}Sr/^{86}Sr$ data (Figure S7) can also be used as proxies for hydrothermal activity (Chen et al., 2006; Huang et al., 2013a; Tostevin et al., 2016; Zeng et al., 2011). All Cat Co 3 sediments record Eu anomalies <1, indicating that they are not affected by hydrothermal supply (Zeng et al., 2011). ΣREE values are elevated above 100 ppm within beds 116, 117, and 124 (Figure S6). Al/(Al+Fe+Mn) values <0.35 indicate hydrothermal supply while values >0.6 indicate terrigenous supply (Huang et al., 2013a; Huang et al., 2013b; Zeng et al., 2011). Based on this criteria, only five Cat Co 3 beds are affected by hydrothermal activity- beds 109, 110, 111, 115a, and 118 (Figure S6). $^{87}Sr/^{86}Sr$ data are contradictory to the Al/(Al+Fe+Mn) values, showing that all of the sample values fall well above 0.7065, an approximate cutoff for hydrothermal influence (Dickson, 1990). All the values are close to 0.7082, similar to the global curve as seen in McArthur et al. (2012) for the D-C boundary.

Other proxies

In contrast to the U/Th ratios that indicate persistent anoxia throughout the Cat Co 3 section, Ni/Co ratios indicate the opposite (Fig. S7). In mudstones, Ni/Co ratios <5.0 record oxic depositional conditions, ratios 5.0-7.0 record dysoxic conditions, and ratios >7.0 record suboxic and anoxic conditions (Jones and Manning, 1994). The Ni/Co values in Cat Co 3 section

sediments range from 1.67 to 9.43, with only beds 115a and 120 recording suboxia/anoxia (Fig. 7). While Ni/Co ratios have been used successfully as paleoredox proxies in mudstones (Hatch and Leventhal, 1992; Jones and Manning, 1994; Riquier et al., 2007), this proxy is not reliable for sections such as the Cat Co 3 that are predominately carbonate (Fig. S4) as Co is only useful as a redox proxy in paleoenvironments with a high detrital component (Tribovillard et al., 2006).

The use of the cerium (Ce) anomaly as a redox proxy remains controversial (Cullers, 2002; Tostevin et al., 2016); we present Ce anomaly data here for the sake of consistency across D-C boundary datasets (Fig. S7). Ce anomalies were calculated using the formula: $Ce_{anom} = \log [3Ce_n/(2La_n + Nd_n)]$, in which n signifies the REE normalization to PAAS values (Elderfield and Greaves, 1982; Morad and Felitsyn, 2001; Wright et al., 1987). Ce anomalies with La/Sm<0.35 indicate diagenetic apatite rather than ocean redox conditions (Morad and Felitsyn, 2001). La/Sm values within the Cat Co 3 section sediments range between 4.07 and 12.01, indicating that Ce anomalies may be used to determine ocean redox conditions during deposition. Using the criteria of German and Elderfield (1990) and Morad and Felitsyn (2001) in biogenic apatite, Ce_{anom} values >-0.1 record anoxic signatures. Out of all geochemically sampled beds (104-126) in the Cat Co 3 section, only two beds (123 and 125) have Ce anomaly values that are considered anoxic (Fig. S7). In contrast, Ce_{anom} <-0.1 are considered to record anoxic signatures if they are calculated using whole rock geochemistry in muds and silts (as opposed to conodont apatite or inarticulate brachiopods) (Wilde et al., 1996). If the interpretation of Wilde et al. (1996) can be applied to whole rock analysis of carbonates, then Cat Co 3 section experienced anoxic conditions throughout most of its history, which is consistent with U/Th signatures (Fig. 6) as well as pyrite framboid distributions (see *4.3*). As some carbonate phases may not record useful Ce anomalies due to fractionation during precipitation and changes in sedimentation rate (Tostevin et al., 2016), and Ce anomalies in carbonates are contingent on Fe and/or Mn speciation (Cullers, 2002; Pattan et al., 2005; Tostevin et al., 2016), the use of the Ce anomaly as a redox proxy in carbonates is fraught with caveats and pitfalls. Therefore, the Ce anomaly is not discussed further for the Cat Co 3 section.

Supplemental Figures

Figure S1. Cross-plots with Al2O3 vs. common redox and productivity proxies used in this study's geochemical analyses. A line is drawn at Al2O3=1 because data from four samples (beds 116, 117, 120, and 121) would skew linear correlation calculations to give an erroneously high R2 value. R2 values are recorded for beds with Al2O3<1, showing that no elements correlate with Al2O3 for a bulk of the Cat Co 3 section. Figure S1 continued on next page.

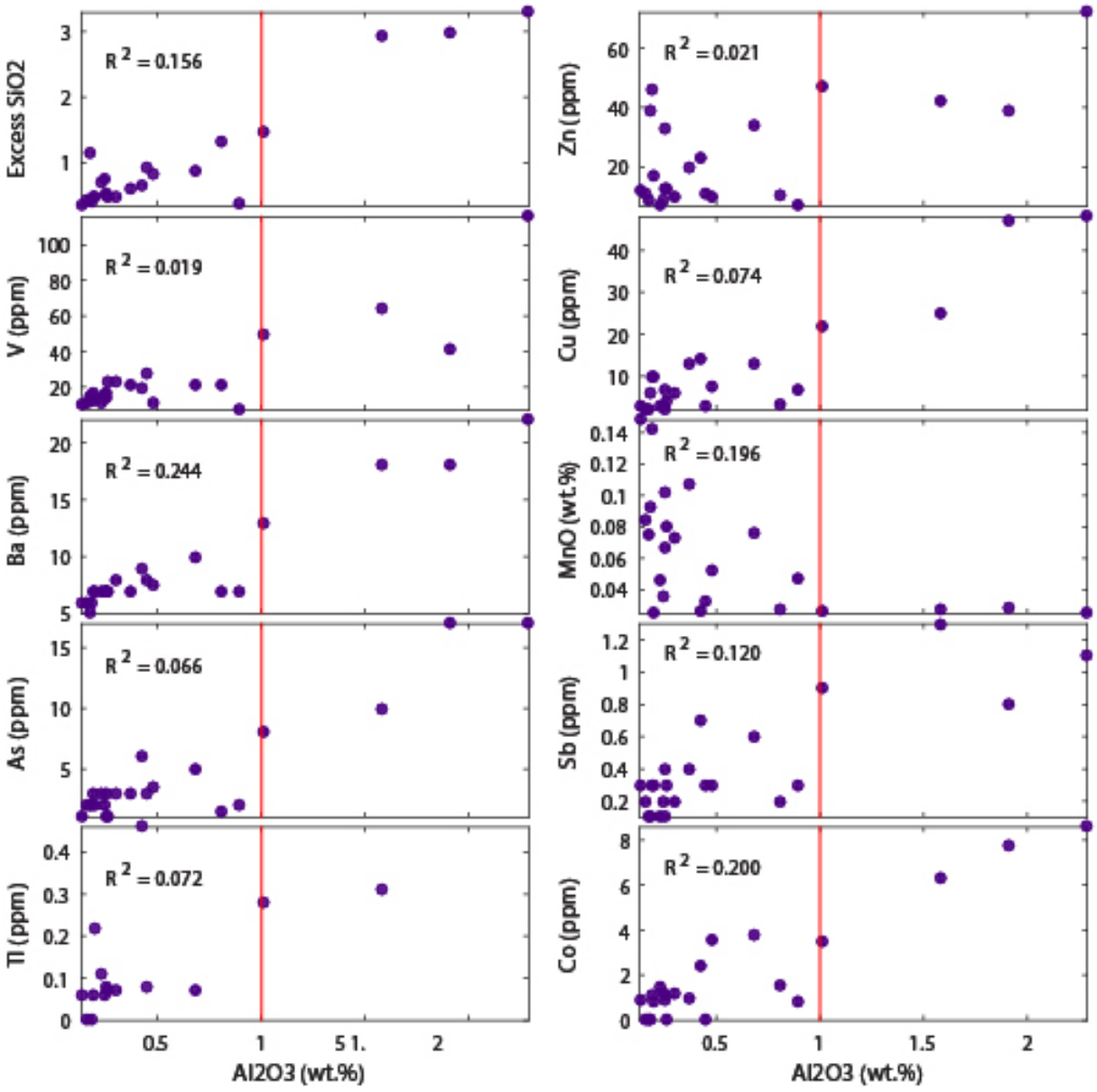

Figure S1. (continued)

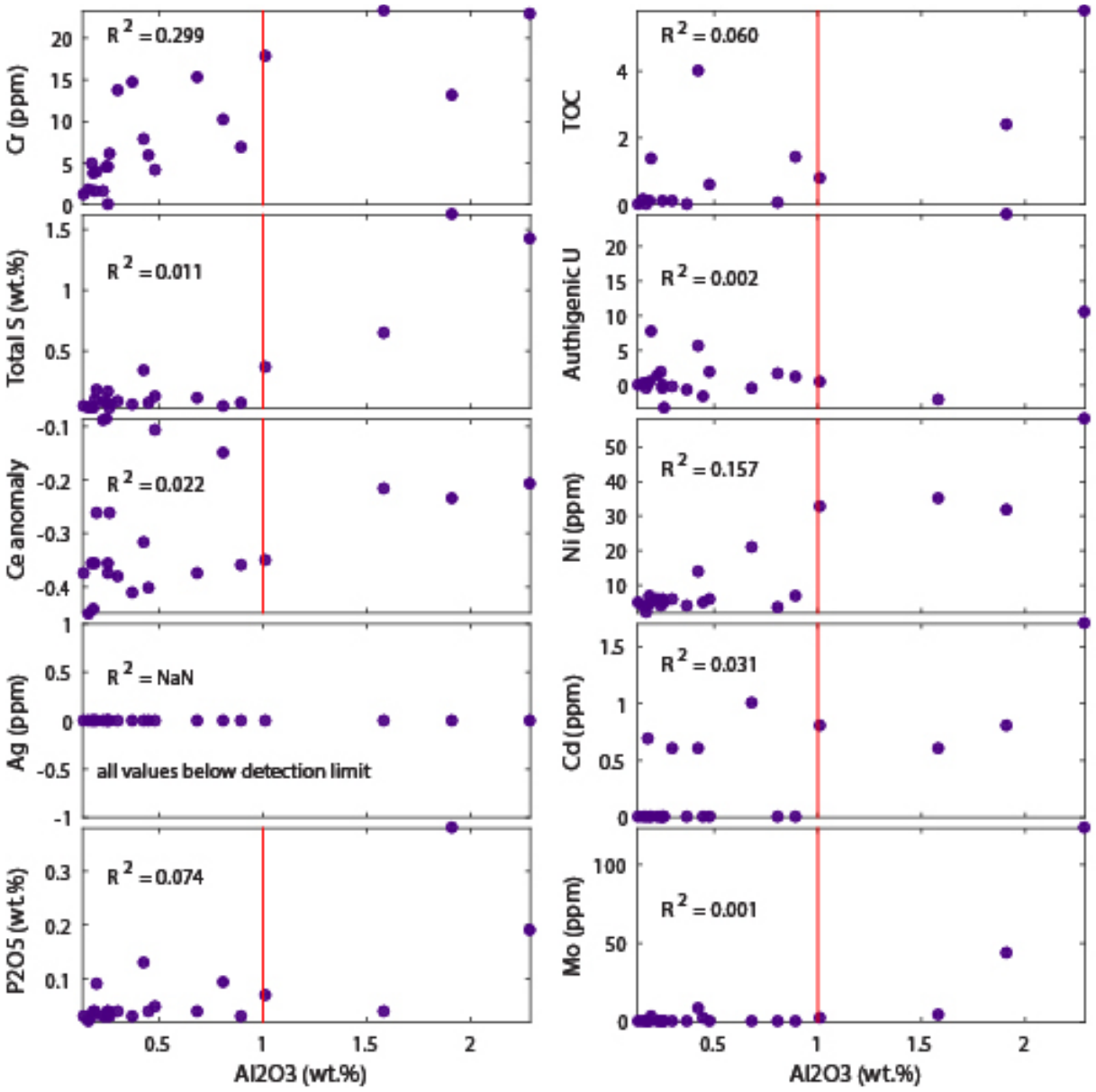

Figure S2. Chemostratigraphy plots of common redox proxy elements normalized to Al.

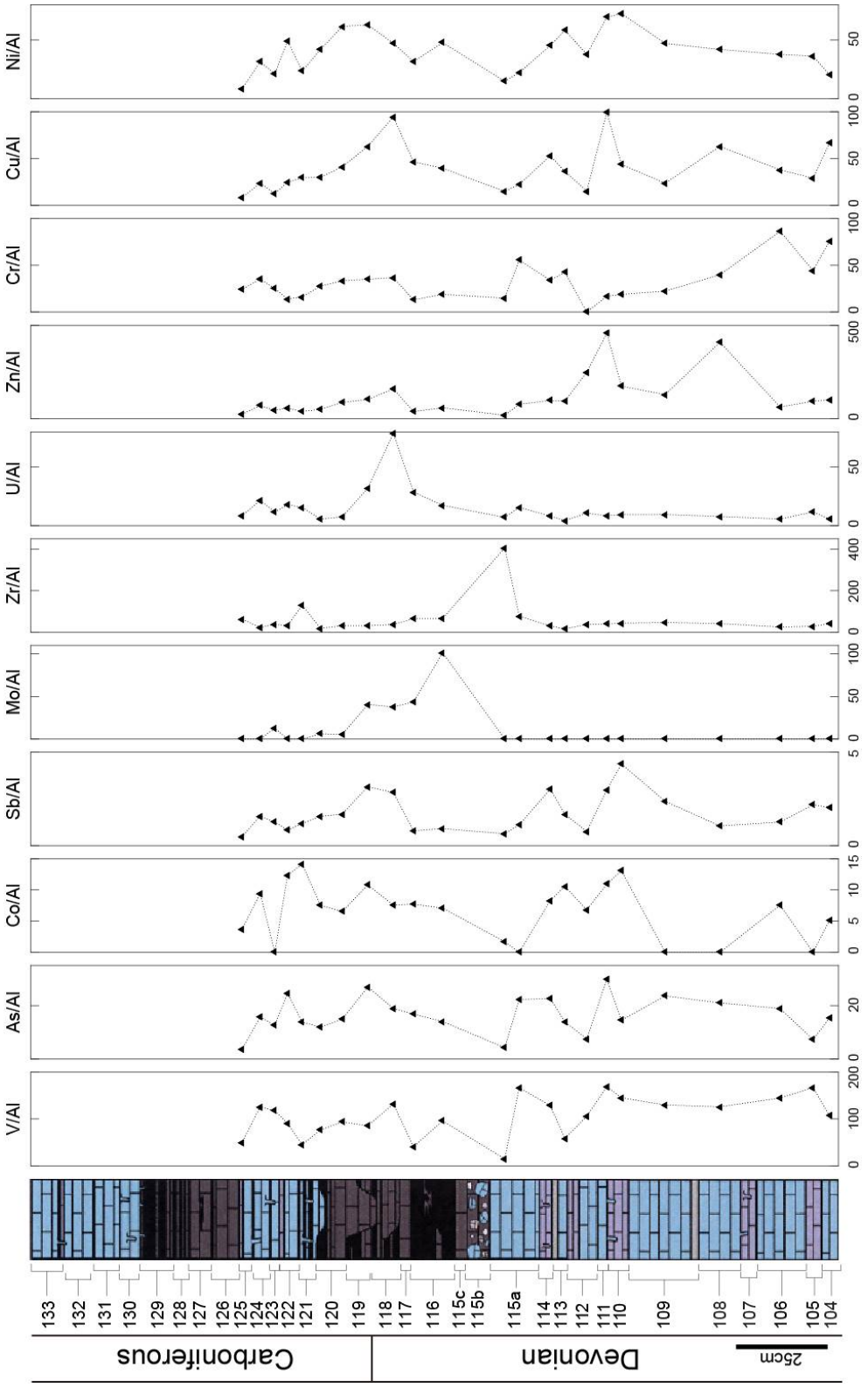

Figure S3. Chemostratigraphic plots normalized to enrichment factors (PAAS).

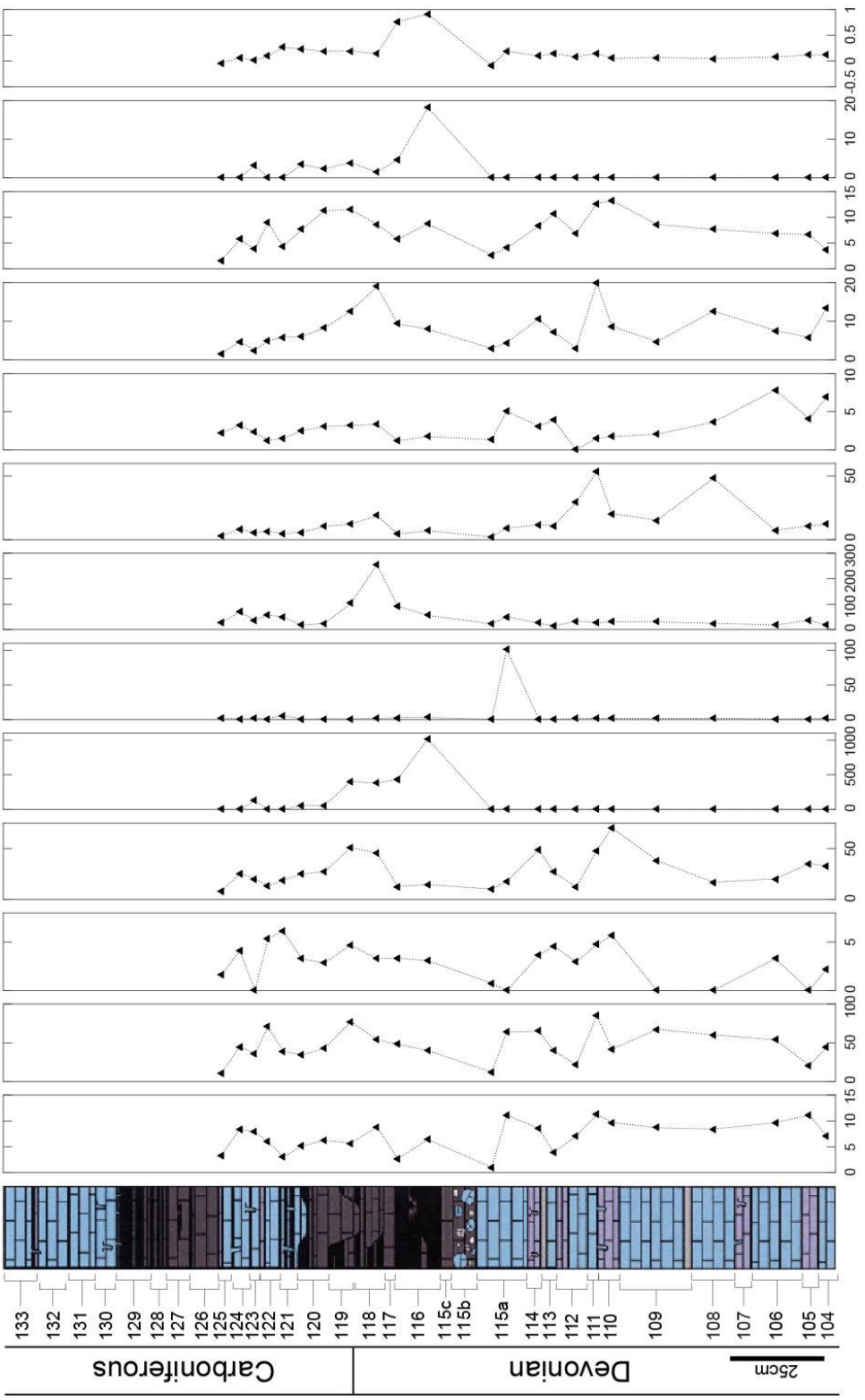

Figure S4. Cross-plots of redox-sensitive element ratios as seen in Riquier et al. (2007). Ranges for oxic/dysoxic/anoxic depositional conditions are from Jones and Manning (1994) and Hatch and Leventhal (1992). Nearly all values show anoxic/dysoxic signatures, particularly for element ratios where there is not a strong detrital component for the denominator element (see Tribovillard et al., 2006 for which elements have a strong detrital component).

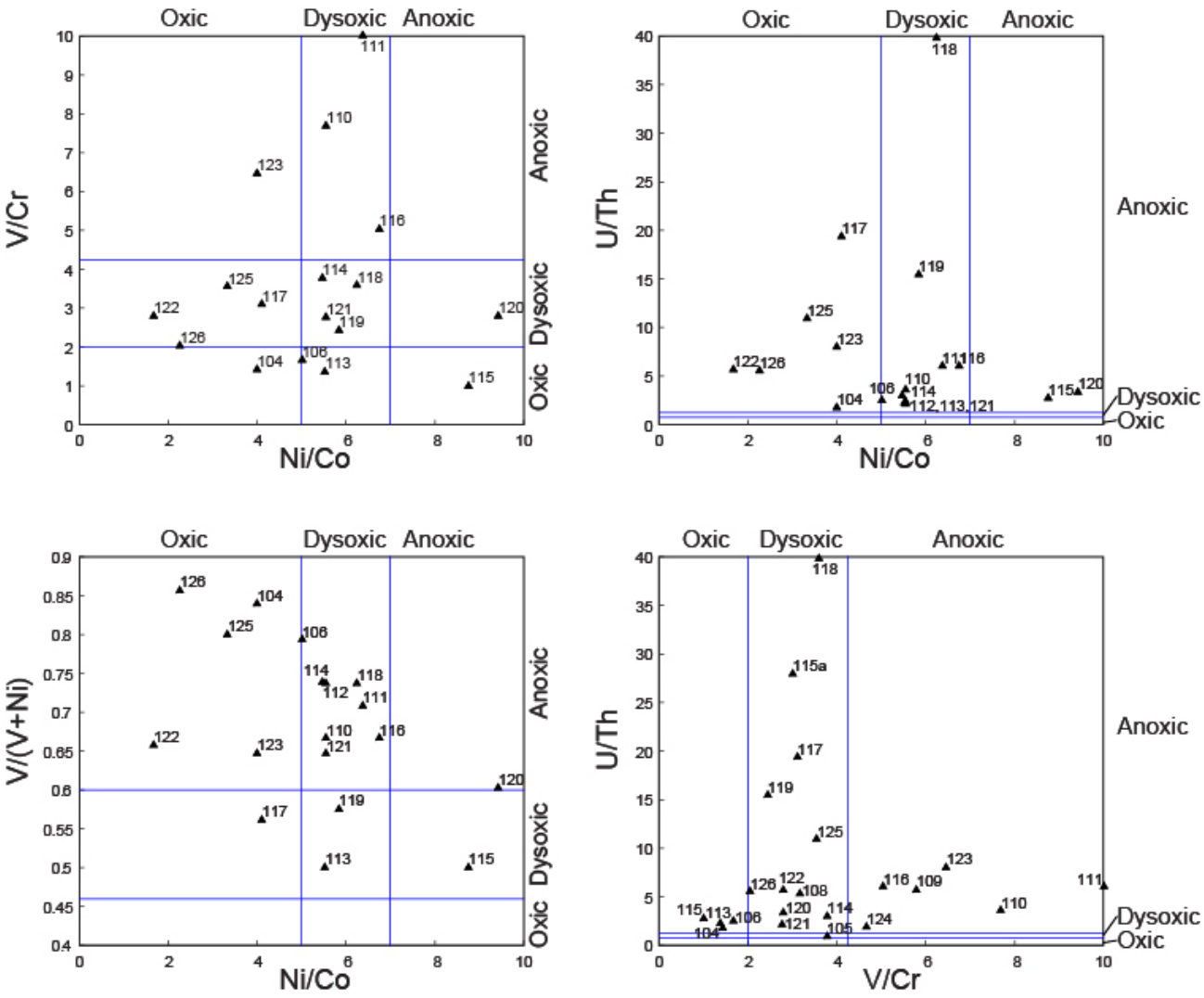

Figure S5. REE normalized spidergrams of beds with complete REE data. REE values are normalized to PAAS. Nearly all measured beds show similar signatures with the exception of bed 124, which has a higher heavy REE component and a pronounced Eu anomaly. However, this bed does not contain evidence for increased detrital input via whole rock geochemistry, SEM-EDS analysis, or XRD analysis.

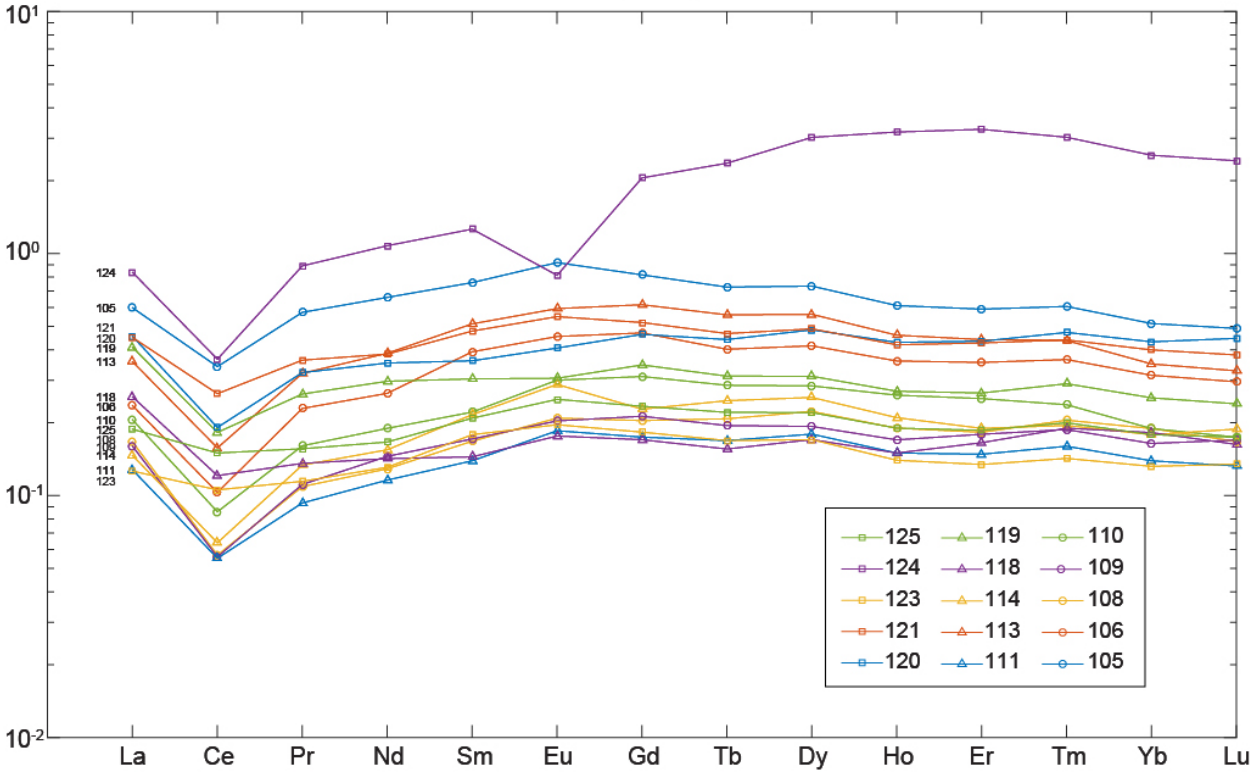

Figure S6. Eu anomaly, REE sums, Al/(Al+Fe+Mn), and $^{87}Sr/^{86}Sr$ data. Eu anomaly and $^{87}Sr/^{86}Sr$ data show that our samples are not affected by hydrothermal supply (see Dickson, 1990 for values), and the Al/(Al+Fe+Mn) data do not show a particularly strong signature for either hydrothermal supply or terrigenous supply.

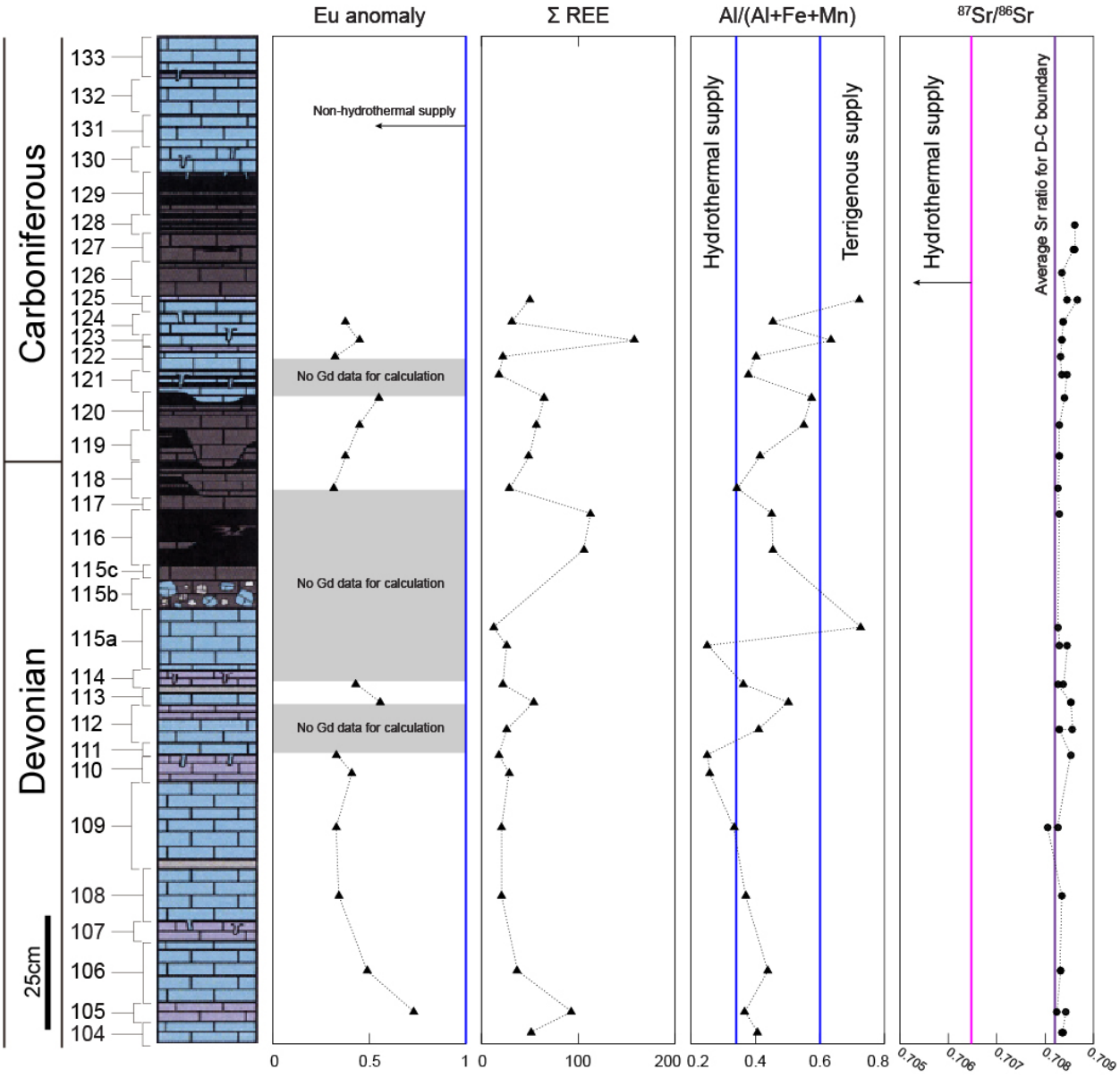

Figure S7. Cerium (Ce) anomalies and Ni/Co are commonly used redox proxies that show inconclusive results for the Cat Co 3 section, due either to low detrital component (Ni/Co), or problems with the proxy itself (Ce anomaly). These figures are provided primarily for consistency across data sets for other D-C boundary units.

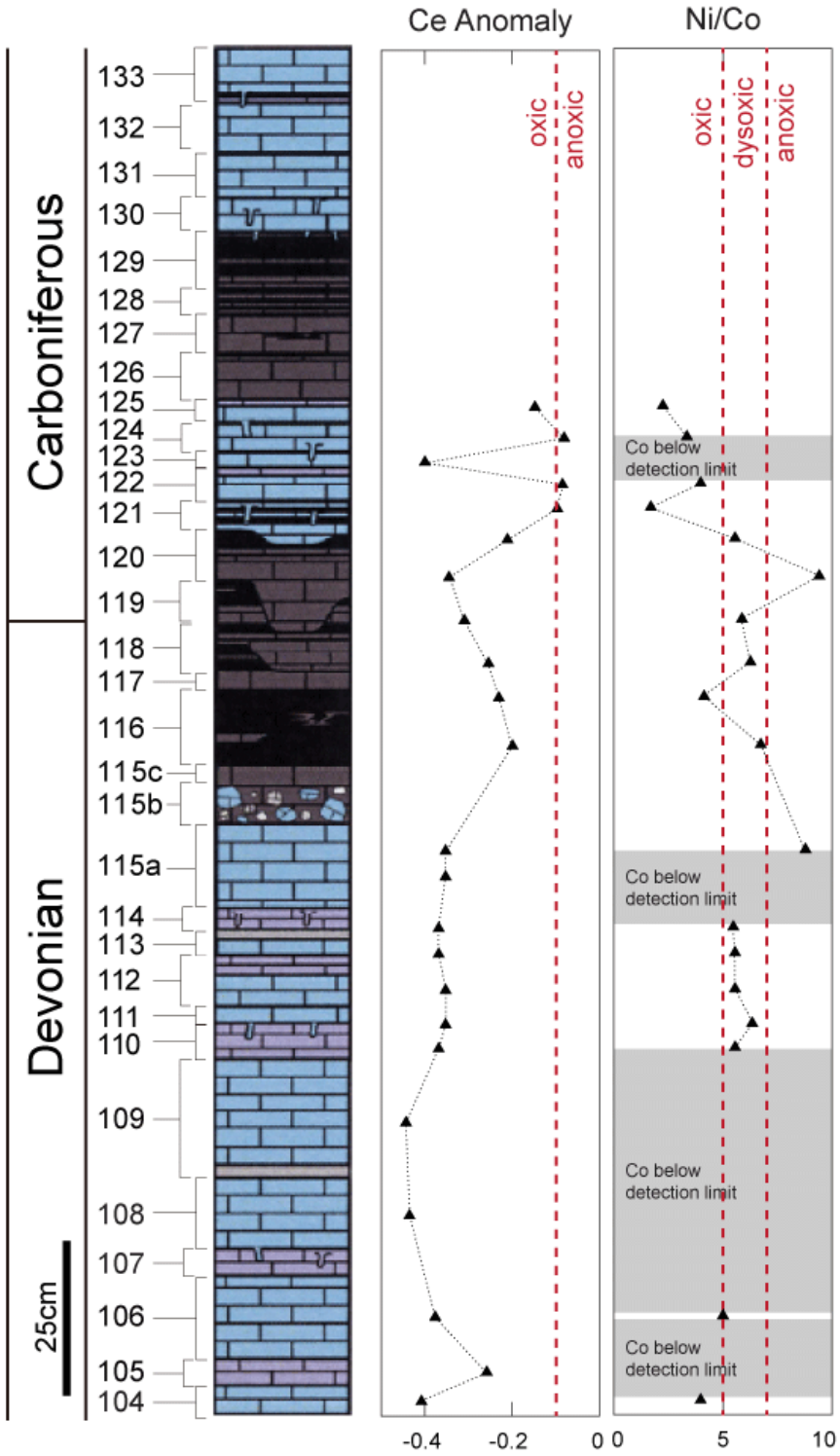

Supplemental Tables

Table S1. Coefficients of variation (standard deviation divided by the mean) for each element analyzed in this study (available in electronic supplemental data). The coefficient of variation for Al is shown at the top (blue box); all elements where the coefficient of variation is below the value for Al are noted in red, and these elements are not suitable for normalization by Al in stratigraphic columns for proxy analysis (per guidelines of Van der Weijden, 2002). Chemostratigraphic data that are normalized to Al are provided in Fig. S2 for ease of comparison across sections that are suitable for Al normalization.

Element	coefficient of variation	Element	coefficient of variation
Al	0.967		
Au	2.416	Se	(below detection limit)
Ag	(below detection limit)	Sn	4.130
As	1.017	Sr	0.275
Ba	0.480	Ta	0.833
Be	(below detection limit)	Th	0.991
Bi	4.899	U	1.439
Br	1.229	V	0.922
Cd	1.626	W	2.534
Co	1.124	Y	0.417
Cr	0.796	Zn	0.752
Cs	1.075	Zr	1.778
Cu	1.130	La	0.700
Ga	1.241	Ce	0.759
Ge	3.406	Pr	1.307
Hf	1.866	Nd	0.789
Hg	1.918	Sm	0.730
In	(below detection limit)	Eu	0.637
Ir	2.847	Gd	1.517
Mo	3.285	Tb	1.412
Nb	1.224	Dy	1.915
Ni	1.175	Ho	2.140
Pb	3.414	Er	2.185
Rb	1.462	Tl	1.501
S	1.656	Tm	1.548
Sb	0.803	Yb	1.240
Sc	0.723	Lu	1.497

Table S2. Major and trace element data (whole rock).

Analyte Symbol	SiO2	Al2O3	Fe2O3(T)	MnO	MgO	CaO	Na2O	K2O
Unit Symbol	%	%	%	%	%	%	%	%
Detection Limit	0.01	0.01	0.01	0.001	0.01	0.01	0.01	0.01
Analysis Method	FUS-ICP	FUS-ICP	FUS-ICP	FUS-ICP	FUS-ICP	FUS-ICP	FUS-ICP	FUS-ICP
Sample								
VN-104	1.07	0.37	0.29	0.107	0.63	53.78	0.07	0.09
VN-105	0.85	0.26	0.25	0.08	0.72	55.41	0.08	0.04
VN-106	0.86	0.3	0.21	0.073	0.74	54.41	0.07	0.06
VN-108	0.71	0.18	0.13	0.093	0.67	54.2	0.06	0.03
VN-109	0.75	0.16	0.15	0.084	0.61	55.27	0.05	0.03
VN-110	0.61	0.13	0.12	0.148	0.6	55.11	0.04	0.03
VN-111	0.86	0.19	0.27	0.142	0.67	55.08	0.07	0.03
VN-112	0.89	0.25	0.2	0.067	0.59	54.2	0.03	0.05
VN-113	1.55	0.68	0.43	0.076	1.65	52.99	0.05	0.15
VN-114	0.96	0.25	0.22	0.102	1.2	53.35	0.04	0.06
VN-115	2.05	0.89	0.33	0.047	0.76	52.09	0.36	0.17
VN-115A	0.67	0.17	0.17	0.075	0.62	54.84	0.04	0.03
VN-116	5.86	2.29	2.06	0.025	0.9	45.13	0.13	0.58
VN-117	5.3	1.91	1.73	0.029	0.9	47.82	0.41	0.48
VN-118	0.86	0.2	0.26	0.026	0.81	54.23	0.05	0.04
VN-119	1.14	0.42	0.42	0.027	0.79	53.96	0.04	0.1
VN-120	2.63	1.01	0.6	0.027	0.62	52.08	0.06	0.25
VN-121	5.24	1.58	0.86	0.028	0.69	49.97	0.04	0.42
VN-122	1.475	0.48	0.54	0.052	0.64	53.445	0.095	0.12
VN-123	1.26	0.23	0.21	0.046	0.65	54.34	0.04	0.06
VN-124	1.65	0.45	0.16	0.033	0.55	53.9	0.07	0.1
VN-125	1.34	0.24	0.18	0.036	0.59	54.92	0.03	0.06
VN-126	2.345	0.805	0.205	0.028	0.58	52.965	0.215	0.185

Table S2. Major and trace element data (whole rock).

Analyte Symbol	TiO2	P2O5	LOI	Total	Mass	Au	Ag	As
Unit Symbol	%	%	%	%	g	ppb	ppm	ppm
Detection Limit	0.001	0.01		0.01		1	0.5	1
Analysis Method	FUS-ICP	FUS-ICP	FUS-ICP	FUS-ICP	INAA	INAA	MULT INAA / TD-ICP	INAA
Sample								
VN-104	0.016	0.03	42.84	99.31	1.185	< 1	< 0.5	3
VN-105	0.004	0.03	41.32	99.04	1.346	4	< 0.5	1
VN-106	0.005	0.04	42.66	99.44	1.214	< 1	< 0.5	3
VN-108	0.002	0.04	43.03	99.13	1.451	2	< 0.5	2
VN-109	0.003	0.02	43.12	100.2	1.359	< 1	< 0.5	2
VN-110	0.004	0.03	43.16	99.99	1.383	< 1	< 0.5	1
VN-111	0.003	0.04	42.76	100.1	1.479	< 1	< 0.5	3
VN-112	0.006	0.04	43.28	99.6	1.035	< 1	< 0.5	1
VN-113	0.018	0.04	42.91	100.5	1.446	< 1	< 0.5	5
VN-114	0.006	0.04	42.79	99.02	1.503	< 1	< 0.5	3
VN-115	0.041	0.03	42.29	99.07	0.779	< 1	< 0.5	2
VN-115A	0.005	0.03	43.45	100.1	0.947	< 1	< 0.5	2
VN-116	0.127	0.19	41.36	98.66	0.5841	29	< 0.5	17
VN-117	0.057	0.38	39.5	98.52	0.7092	3	< 0.5	17
VN-118	0.004	0.09	42.64	99.21	1.4	3	< 0.5	2
VN-119	0.015	0.13	42.46	99.49	1.459	< 1	< 0.5	6
VN-120	0.045	0.07	42.32	99.71	1.249	9	< 0.5	8
VN-121	0.067	0.04	40.2	99.14	1.387	< 1	< 0.5	10
VN-122	0.021	0.05	42.54	78.19	0.7825	15.5	< 0.5	3.5
VN-123	0.006	0.03	42.9	99.77	1.375	< 1	< 0.5	3
VN-124	0.006	0.04	42.53	99.5	1.357	3	< 0.5	3
VN-125	0.006	0.03	42.77	100.2	1.445	< 1	< 0.5	2
VN-126	0.011	0.095	42.34	99.775	0.87695	< 1	< 0.5	1.5

Table S2. Major and trace element data (whole rock).

Analyte Symbol	**Ba**	**Br**	**Cd**	**Co**	**Cr**	**Cs**	**Cu**	**Hg**
Unit Symbol	ppm	ppm	ppm	ppm	ppm	ppm	ppm	ppm
Detection Limit	1	0.5	0.5	0.1	0.5	0.1	1	1
Analysis Method	FUS-ICP	INAA	TD-ICP	INAA	INAA	FUS-MS	TD-ICP	INAA
Sample								
VN-104	7	< 0.5	< 0.5	1	14.8	< 0.2	13	< 1
VN-105	7	< 0.5	< 0.5	< 0.1	6.1	0.3	4	< 1
VN-106	8	< 0.5	0.6	1.2	13.7	0.3	6	< 1
VN-108	6	0.9	0.7	< 0.1	3.8	0.2	6	< 1
VN-109	6	< 0.5	< 0.5	< 0.1	1.9	0.3	2	< 1
VN-110	6	0.5	< 0.5	0.9	1.3	0.3	3	< 1
VN-111	7	0.9	< 0.5	1.1	1.7	0.3	10	< 1
VN-112	7	1.2	< 0.5	0.9	< 0.5	< 0.2	2	< 1
VN-113	10	1	1	3.8	15.3	0.5	13	< 1
VN-114	7	< 0.5	< 0.5	1.1	4.5	0.3	7	< 1
VN-115	7	0.8	< 0.5	0.8	7	< 0.2	7	< 1
VN-115A	5	1.2	< 0.5	< 0.1	5	< 0.2	2	< 1
VN-116	22	7.3	1.7	8.6	23	< 0.2	48	< 1
VN-117	18	6.2	0.8	7.8	13.2	< 0.2	47	< 1
VN-118	7	2.1	< 0.5	0.8	3.9	0.3	10	< 1
VN-119	9	1.1	0.6	2.4	7.8	0.4	14	< 1
VN-120	13	< 0.5	0.8	3.5	17.9	0.7	22	< 1
VN-121	18	1.3	0.6	6.3	23.2	1.1	25	< 1
VN-122	7.5	2.15	< 0.5	3.6	4.1	< 0.2	7.5	< 1
VN-123	7	1.6	< 0.5	1.5	1.7	0.3	3	< 1
VN-124	8	1.3	< 0.5	< 0.1	6	0.5	3	< 1
VN-125	7	0.9	< 0.5	1.2	4.5	0.3	3	< 1
VN-126	7	1.65	< 0.5	1.55	10.25	< 0.2	3.5	< 1

Table S2. Major and trace element data (whole rock).

Analyte Symbol	**In**	**Ir**	**Mo**	**Ni**	**Pb**	**Rb**	**S**	**Sb**
Unit Symbol	ppm	ppb	ppm	ppm	ppm	ppm	%	ppm
Detection Limit	0.1	1	2	1	5	1	0.001	0.1
Analysis Method	FUS-MS	INAA	FUS-MS	TD-ICP	TD-ICP	FUS-MS	TD-ICP	INAA
Sample								
VN-104	NA	< 1	< 2	4	< 5	< 10	0.068	0.4
VN-105	< 0.1	< 1	< 2	5	< 5	2	0.039	0.3
VN-106	< 0.1	< 1	< 2	6	< 5	2	0.085	0.2
VN-108	< 0.1	< 1	< 2	4	< 5	1	0.032	0.1
VN-109	< 0.1	< 1	< 2	4	< 5	1	0.038	0.2
VN-110	< 0.1	< 1	< 2	5	< 5	1	0.053	0.3
VN-111	< 0.1	< 1	< 2	7	< 5	1	0.098	0.3
VN-112	NA	< 1	< 2	5	< 5	< 10	0.071	0.1
VN-113	< 0.1	< 1	< 2	21	< 5	5	0.119	0.6
VN-114	< 0.1	< 1	< 2	6	< 5	2	0.164	0.4
VN-115	NA	8	< 2	7	< 5	< 10	0.077	0.3
VN-115A	NA	< 1	< 2	2	< 5	< 10	0.029	0.1
VN-116	NA	29	123	58	10	10	1.43	1.1
VN-117	NA	3	44	32	< 5	< 10	1.62	0.8
VN-118	< 0.1	< 1	4	5	< 5	2	0.18	0.3
VN-119	< 0.1	< 1	9	14	< 5	3	0.344	0.7
VN-120	< 0.1	< 1	3	33	< 5	8	0.374	0.9
VN-121	< 0.1	< 1	5	35	8	15	0.648	1.3
VN-122	NA	< 1	< 2	6	< 5	< 10	0.129	0.3
VN-123	< 0.1	< 1	< 2	6	< 5	2	0.092	0.1
VN-124	< 0.1	< 1	3	5	< 5	4	0.08	0.3
VN-125	< 0.1	< 1	< 2	4	< 5	2	0.073	0.2
VN-126	NA	12.5	< 2	3.5	< 5	< 10	0.0505	0.2

Table S2. Major and trace element data (whole rock).

Analyte Symbol	Sc	Se	Sn	Ta	U	W	Y	Zn
Unit Symbol	ppm	ppm	ppm	ppm	ppm	ppm	ppm	ppm
Detection Limit	0.01	0.5	1	0.01	0.01	1	1	1
Analysis Method	INAA	INAA	FUS-MS	FUS-MS	FUS-MS	INAA	FUS-ICP	MULT INAA / TD-ICP
Sample								
VN-104	1.42	< 0.5	NA	< 0.3	1.1	< 1	23	20
VN-105	3.2	< 0.5	< 1	0.27	1.6	< 1	21	13
VN-106	4	< 0.5	< 1	0.3	0.89	< 1	15	10
VN-108	0.64	< 0.5	1	0.27	0.74	< 1	9	39
VN-109	0.43	< 0.5	< 1	0.3	0.8	< 1	9	11
VN-110	0.58	< 0.5	< 1	0.29	0.64	< 1	11	12
VN-111	0.46	< 0.5	< 1	0.25	0.85	< 1	7	46
VN-112	1.22	< 0.5	NA	< 0.3	1.4	< 1	19	33
VN-113	2.37	< 0.5	< 1	0.27	1.51	< 1	18	34
VN-114	0.87	< 0.5	< 1	0.35	1.07	< 1	8	13
VN-115	0.45	< 0.5	NA	< 0.3	3.3	7	9	9
VN-115A	0.53	< 0.5	NA	< 0.3	1.4	< 1	13	7
VN-116	2.3	< 0.5	NA	< 0.3	21	4	23	72
VN-117	1.75	< 0.5	NA	< 0.3	29	1	27	39
VN-118	0.51	< 0.5	< 1	0.3	8.37	< 1	8	17
VN-119	0.92	< 0.5	< 1	0.3	7.09	< 1	12	23
VN-120	2.46	< 0.5	< 1	0.34	4	< 1	18	47
VN-121	2.51	< 0.5	< 1	0.38	4.57	< 1	16	42
VN-122	0.67	< 0.5	NA	NA	3.95	2	10.5	10
VN-123	0.47	< 0.5	< 1	0.3	2.17	< 1	6	7
VN-124	1.54	< 0.5	5	0.22	2.76	< 1	14	11
VN-125	0.71	< 0.5	< 1	0.29	2.73	< 1	8	9
VN-126	1.26	< 0.5	NA	< 0.3	3.6	1	16.5	10.5

Table S2. Major and trace element data (whole rock).

Analyte Symbol	**Zr**	**Ce**	**Pr**	**Gd**	**Dy**	**Tl**	**Be**	**V**
Unit Symbol	ppm	ppm	ppm	ppm	ppm	ppm	ppm	ppm
Detection Limit	1	0.05	0.01	0.01	0.01	0.05	1	5
Analysis Method	FUS-ICP	FUS-MS	FUS-MS	FUS-MS	FUS-MS	FUS-MS	FUS-ICP	FUS-ICP
Sample								
VN-104	8	14	NA	NA	NA	NA	< 1	21
VN-105	4	27.3	5.09	3.84	3.23	0.07	< 1	23
VN-106	4	8.25	2.04	2.21	1.83	0.07	< 1	23
VN-108	4	4.54	0.97	0.96	0.98	< 0.05	< 1	12
VN-109	4	4.47	0.99	1	0.85	< 0.05	< 1	11
VN-110	3	6.86	1.43	1.46	1.25	0.06	< 1	10
VN-111	4	4.41	0.83	0.82	0.79	0.06	< 1	17
VN-112	5	8	NA	NA	NA	NA	< 1	14
VN-113	6	12.6	2.85	2.89	2.47	0.07	< 1	21
VN-114	4	5.11	1.19	1.07	1.12	0.08	< 1	17
VN-115	191	8	NA	NA	NA	NA	< 1	7
VN-115A	7	4	NA	NA	NA	NA	< 1	15
VN-116	81	42	NA	NA	NA	NA	< 1	116
VN-117	66	43	NA	NA	NA	NA	< 1	41
VN-118	4	9.68	1.21	0.8	0.75	0.22	< 1	14
VN-119	7	14.6	2.34	1.63	1.37	0.46	< 1	19
VN-120	17	15.3	2.87	2.18	2.13	0.28	< 1	50
VN-121	16	21.1	3.23	2.44	2.15	0.31	< 1	64
VN-122	33	8	NA	NA	NA	NA	< 1	11.5
VN-123	4	8.45	1.02	0.86	0.75	0.11	< 1	11
VN-124	9	29.3	7.92	9.66	13.3	0.08	< 1	28
VN-125	3	12	1.39	1.1	0.97	0.06	< 1	16
VN-126	27	20	NA	NA	NA	NA	< 1	21

Table S2. Major and trace element data (whole rock).

Analyte Symbol	**Ga**	**Ge**	**Sr**	**Nb**	**La**	**Nd**	**Sm**	**Eu**
Unit Symbol	ppm	ppm	ppm	ppm	ppm	ppm	ppm	ppm
Detection Limit	1	0.5	2	0.2	0.05	0.05	0.01	0.005
Analysis Method	FUS-MS	FUS-MS	FUS-ICP	FUS-MS	FUS-MS	FUS-MS	FUS-MS	FUS-MS
Sample								
VN-104	NA	NA	272	NA	15.4	17	2.44	0.6
VN-105	1	< 0.5	284	0.8	22.7	21.1	4.25	1.01
VN-106	1	< 0.5	309	0.6	8.95	8.47	2.2	0.5
VN-108	1	< 0.5	266	0.4	6.34	4.13	0.94	0.23
VN-109	1	< 0.5	314	0.4	6.08	4.65	0.96	0.224
VN-110	1	< 0.5	296	0.4	7.82	6.07	1.24	0.33
VN-111	1	< 0.5	285	0.3	4.86	3.71	0.78	0.204
VN-112	NA	NA	295	NA	9.24	6	1.51	0.4
VN-113	2	0.5	305	0.5	13.6	12.4	2.87	0.652
VN-114	1	< 0.5	351	0.6	5.57	4.95	1.21	0.317
VN-115	NA	NA	334	NA	8.07	8	0.75	0.3
VN-115A	NA	NA	286	NA	5.23	2	0.68	< 0.2
VN-116	NA	NA	545	NA	33.2	24	3.65	0.8
VN-117	NA	NA	578	NA	36	27	3.75	0.9
VN-118	< 1	< 0.5	508	0.2	9.73	4.55	0.81	0.194
VN-119	1	< 0.5	515	0.4	15.6	9.5	1.7	0.336
VN-120	2	< 0.5	437	1	17.3	11.3	2.02	0.448
VN-121	3	< 0.5	357	1.7	17.1	12.3	2.68	0.604
VN-122	NA	NA	269.5	NA	5.665	2.5	0.885	0.1
VN-123	< 1	< 0.5	294	0.3	4.8	4.19	1	0.216
VN-124	1	0.6	358	0.6	31.8	34.5	7.07	0.895
VN-125	< 1	< 0.5	245	< 0.2	7.15	5.33	1.17	0.275
VN-126	NA	NA	310.5	NA	11.7	14	2.22	0.45

Table S2. Major and trace element data (whole rock).

Analyte Symbol	Tb	Ho	Er	Tm	Yb	Lu	Hf	Bi
Unit Symbol	ppm	ppm	ppm	ppm	ppm	ppm	ppm	ppm
Detection Limit	0.01	0.01	0.01	0.005	0.01	0.002	0.1	0.1
Analysis Method	FUS-MS	FUS-MS	FUS-MS	FUS-MS	FUS-MS	FUS-MS	FUS-MS	FUS-MS
Sample								
VN-104	0.3	NA	NA	NA	1.01	0.2	< 0.2	< 2
VN-105	0.56	0.61	1.71	0.242	1.44	0.211	0.2	< 0.1
VN-106	0.31	0.36	1.03	0.146	0.88	0.127	0.2	< 0.1
VN-108	0.16	0.19	0.53	0.082	0.53	0.072	0.2	< 0.1
VN-109	0.15	0.17	0.52	0.075	0.46	0.073	0.1	< 0.1
VN-110	0.22	0.26	0.73	0.095	0.53	0.075	0.2	< 0.1
VN-111	0.13	0.15	0.43	0.064	0.39	0.057	0.2	< 0.1
VN-112	0.2	NA	NA	NA	0.7	0.12	< 0.2	< 2
VN-113	0.43	0.46	1.28	0.175	0.98	0.141	0.2	< 0.1
VN-114	0.19	0.21	0.55	0.078	0.5	0.081	0.1	< 0.1
VN-115	< 0.1	NA	NA	NA	0.65	0.05	5.5	< 2
VN-115A	< 0.1	NA	NA	NA	0.38	0.09	< 0.2	< 2
VN-116	0.3	NA	NA	NA	1.55	< 0.01	1.8	< 2
VN-117	0.5	NA	NA	NA	1.55	0.03	1.4	< 2
VN-118	0.12	0.15	0.48	0.076	0.51	0.07	0.2	< 0.1
VN-119	0.24	0.27	0.77	0.116	0.71	0.103	0.3	< 0.1
VN-120	0.34	0.43	1.26	0.189	1.21	0.192	0.5	< 0.1
VN-121	0.36	0.42	1.24	0.176	1.12	0.164	0.6	< 0.1
VN-122	< 0.1	NA	NA	NA	0.65	0.08	0.75	< 2
VN-123	0.13	0.14	0.39	0.057	0.37	0.058	0.2	< 0.1
VN-124	1.82	3.18	9.46	1.21	7.14	1.04	0.4	0.3
VN-125	0.17	0.19	0.54	0.08	0.5	0.075	< 0.1	< 0.1
VN-126	0.4	NA	NA	NA	0.83	0.07	0.6	< 2

Table S3. Carbon isotope and TOC data.

Sample	$\delta^{13}C_{org}$	$\delta^{13}C_{carb}$ (sample set 1)	$\delta^{13}C_{carb}$ (sample set 2)	TOC (wt%)
105		2.02		0.08946
107	-25.25	1.99		0.10156
108	-26.07	1.64		0.06338
110 (top)	-24.83	1.5		0.09223
110 (bottom)	-25.35	1.8		0.10274
111	-25.75	2.21		0.07723
112	-25.68	1.61		0.06071
113	-25.11	1.49		0.09306
114	-25.76	1.2		0.1073
115B (115a)	-26.11	1.1		0.09069
115b	-26.16	1.84		0.13969
115c	-25.86	2.29	1.80, 0.91, 1.77	0.37798
116A	-24.83	1.46	1.26, 1.34, 1.54	5.63637
116C	-24.71	1.07		5.76084
117-1	-26.03	1.03	1.08, 1.09	0.59006
117-2	-26.38	1.42		4.21093
118-1	-26.21	1.19	2.67, 1.62, 1.47, 1.45	3.97544
118-2	-26.27	1.1		1.95104
118-3	-26.48	1.86		0.67217
119-1	-26.36	1.57	0.97, 2.39, 3.12, 0.91	4.48834
119-2	-26.47	1.46		3.37707
119-4	-26.59	2.11		0.50966
120	-26.51	0.86	3.39, 1.45	0.87189
120-1	-25.82	1.86		0.16913
121	-26.28	1.66	1.10, 2.81	0.16638
121-1	-25.9			0.80514
122	-26.52	1.87	1.55	0.13158
123	-26.23		1.93	0.17975
124	-26.71	1.61	2.16, 2.55	0.11875
125	-26.71	1.38	1.84	0.13494
125 (top)	-27.05			0.21602
126	-26.58	2.13	2.21, 2.14	0.18182
126 (top)	-26.48	2.36		0.37349
127	-26.77	2.26		0.1806
128-2	-26.79	2.95		0.92872
128-4	-26.68			0.53621
129-2	-26.68	2.33		0.23016
129-3	-26.81	1.39		1.05748
130		1.39		
131		2.21		
132		1.66		

Table S4. $^{87}Sr/^{86}Sr$ data. Some samples were analyzed in both 2014 and 2017 as duplicates.

Sample	$^{87}Sr/^{86}Sr$	2σ
104	0.708336	0.0006
104	0.70836	0.0007
105	0.70843	0.0006
105	0.708246	0.0007
106	0.708318	0.0007
106	0.708307	0.0006
108	0.708345	0.0006
109	0.708052	0.0006
109	0.708256	0.0007
111	0.708528	0.0005
112	0.708291	0.0008
112	0.708302	0.0008
112	0.708572	0.0007
113	0.708534	0.0007
113	0.708525	0.0007
114	0.708256	0.0007
114	0.708386	0.0008
115a	0.708464	0.0007
115a	0.708303	0.0007
115	0.708268	0.0008
117	0.708291	0.0008
118	0.70827	0.0007
119	0.708298	0.0009
119	0.708282	0.0006
120	0.708296	0.0007
121	0.708409	0.0007
122	0.708446	0.0007
122	0.708339	0.0008
123	0.708315	0.0007
124	0.708351	0.0006
124	0.708348	0.0007
125	0.708375	0.0008
125	0.70838	0.0007
126	0.708672	0.0006
126	0.708447	0.0008
127	0.708353	0.0007
128	0.708586	0.0007
128	0.708621	0.0007
129	0.708621	0.0008

References

Algeo, T.J. and Tribovillard, N., 2009. Environmental analysis of paleoceanographic systems based on molybdenum–uranium covariation. Chemical Geology, 268(3–4), 211-225.

Chen, D., Qing, H., Yan, X. and Li, H., 2006. Hydrothermal venting and basin evolution (Devonian, South China): Constraints from rare earth element geochemistry of chert. Sedimentary Geology, 183(3-4), 203-216.

Chen, X. and Liao, Z., 2006. The palaeoecological characters of the brachiopod genus Planovatirostrum Sartenaer, 1970. Acta Palaeontologica Sinica, 45(1), 82.

Cullers, R.L., 2002. Implications of elemental concentrations for provenance, redox conditions, and metamorphic studies of shales and limestones near Pueblo, CO, USA. Chemical Geology, 191(4), 305-327.

Dickson, T., 1990. Carbonate mineralogy and chemistry. In: M.R. Tucker and V.P. Wright (Eds.), Carbonate sedimentology. Blackwell Science, Oxford, England, pp. 284-313.

Elderfield, H. and Greaves, M.J., 1982. The rare earth elements in seawater. Nature, 296, 214-219.

German, C.R. and Elderfield, H., 1990. Application of the Ce anomaly as a paleoredox indicator; the ground rules. Paleoceanography, 5(5), 823-833.

Hatch, J. and Leventhal, J., 1992. Relationship between inferred redox potential of the depositional environment and geochemistry of the Upper Pennsylvanian (Missourian) Stark Shale Member of the Dennis Limestone, Wabaunsee County, Kansas, USA. Chemical Geology, 99(1-3), 65-82.

Huang, H. et al., 2013a. Depositional chemistry of chert during late Paleozoic from western Guangxi and its implication for the tectonic evolution of the Youjiang Basin. Science China Earth Sciences, 56(3), 479-493.

Huang, H. et al., 2013b. Geochemistry of the Late Paleozoic cherts in the Youjiang Basin: Implications for the basin evolution. Journal of Palaeogeography, 2(4), 402-421.

Jones, B. and Manning, D.A., 1994. Comparison of geochemical indices used for the interpretation of palaeoredox conditions in ancient mudstones. Chemical Geology, 111(1), 111-129.

McArthur, J., Howarth, R. and Shields, G., 2012. Strontium Isotope Stratigraphy. The Geologic Time Scale, 1, 127-144.

Morad, S. and Felitsyn, S., 2001. Identification of primary Ce-anomaly signatures in fossil biogenic apatite: implication for the Cambrian oceanic anoxia and phosphogenesis. Sedimentary Geology, 143(3), 259-264.

Pattan, J.N., Pearce, N.J.G. and Mislankar, P.G., 2005. Constraints in using Cerium-anomaly of bulk sediments as an indicator of paleo bottom water redox environment: A case study from the Central Indian Ocean Basin. Chemical Geology, 221(3–4), 260-278.

Riquier, L. et al., 2007. Environmental changes at the Frasnian–Famennian boundary in Central Morocco (Northern Gondwana): integrated rock-magnetic and geochemical studies. Geological Society, London, Special Publications, 278(1), 197-217.

Tostevin, R. et al., 2016. Effective use of cerium anomalies as a redox proxy in carbonate-dominated marine settings. Chemical Geology, 438, 146-162.

Tribovillard, N., Algeo, T.J., Lyons, T. and Riboulleau, A., 2006. Trace metals as paleoredox and paleoproductivity proxies: An update. Chemical Geology, 232(1–2), 12-32.

Tribovillard, N. et al., 2015. Iron availability as a dominant control on the primary composition and diagenetic overprint of organic-matter-rich rocks. Chemical Geology, 401, 67-82.
Van der Weijden, C.H., 2002. Pitfalls of normalization of marine geochemical data using a common divisor. Marine Geology, 184(3-4), 167-187.
Wilde, P., Quinby-Hunt, M.S. and Erdtmann, B.-D., 1996. The whole-rock cerium anomaly: a potential indicator of eustatic sea-level changes in shales of the anoxic facies. Sedimentary Geology, 101(1), 43-53.
Wright, J., Schrader, H. and Holser, W.T., 1987. Paleoredox variations in ancient oceans recorded by rare earth elements in fossil apatite. Geochimica et Cosmochimica Acta, 51(3), 631-644.
Xu, B., Gu, Z., Han, J. and Wang, C., 2008. Environmental changes during Frasnian-Famennian transition in south China: A multiproxy approach. Journal of Geophysical Research: Biogeosciences, 113(G4).
Zeng, J., Xu, R. and Gong, Y., 2011. Hydrothermal activities and seawater acidification in the Late Devonian FF transition: Evidence from geochemistry of rare earth elements. Science China Earth Sciences, 54(4), 540.